

M2-SCREAM: A Stratospheric Composition Reanalysis of Aura MLS data with MERRA-2 transport

Krzysztof Wargan¹, Brad Weir², Gloria L Manney³, Stephen E. Cohn⁴, K. Emma Knowland⁵, Pamela A Wales⁶, and Nathaniel J Livesey⁷

¹Science Systems and Applications, Inc.

²USRA / NASA Goddard

³Northwest Research Associates

⁴Data Assimilation Office

⁵Morgan State University

⁶University of Maryland, College Park

⁷Jet Propulsion Laboratory

November 24, 2022

Abstract

MERRA-2 Stratospheric Composition Reanalysis of Aura Microwave Limb Sounder (M2-SCREAM) is a new reanalysis of stratospheric ozone, water vapor, hydrogen chloride (HCl), nitric acid (HNO₃) and nitrous oxide (N₂O) between 2004 and the present (with a latency of several months). The assimilated fields are provided at a 50-km horizontal resolution and at a three-hourly frequency. M2-SCREAM assimilates version 4.2 Microwave Limb Sounder (MLS) profiles of the five constituents alongside total ozone column from the Ozone Monitoring Instrument. Dynamics and tropospheric water vapor are constrained by the MERRA-2 reanalysis. The assimilated species are in excellent agreement with the MLS observations, except for HNO₃ in polar night, where data are not assimilated. Comparisons against independent observations show that the reanalysis realistically captures the spatial and temporal variability of all the assimilated constituents. In particular, the standard deviations of the differences between M2-SCREAM and constituent mixing ratio data from The Atmospheric Chemistry Experiment Fourier Transform Spectrometer are much smaller than the standard deviations of the measured constituents. Evaluation of the reanalysis against aircraft data and balloon-borne frost point hygrometers indicates a faithful representation of small-scale structures in the assimilated water vapor, HNO₃ and ozone fields near the tropopause. Comparisons with independent observations and a process-based analysis of the consistency of the assimilated constituent fields with the MERRA-2 dynamics and with large-scale stratospheric processes demonstrate the utility of M2-SCREAM for scientific studies of chemical and transport variability on time scales ranging from hours to decades. Analysis uncertainties and guidelines for data usage are provided.

1 **M2-SCREAM: A Stratospheric Composition Reanalysis of Aura MLS data**
2 **with MERRA-2 transport**

3 **Krzysztof Wargan^{1,2}, Brad Weir^{2,3,†}, Gloria L. Manney^{4,5}, Stephen E. Cohn², K. Emma**
4 **Knowland^{2,3,†}, Pamela A. Wales^{2,3,†}, and Nathaniel J. Livesey⁶**

5 ¹ Science Systems and Applications Inc., Lanham, Maryland, USA

6 ² Global Modeling and Assimilation Office, NASA Goddard Space Flight Center, Greenbelt, Maryland,
7 USA

8 ³ Universities Space Research Association, Columbia, Maryland, USA

9 ⁴ NorthWest Research Associates, Socorro, New Mexico, USA

10 ⁵ Department of Physics, New Mexico Institute of Mining and Technology, Socorro, New Mexico, USA

11 ⁶ Jet Propulsion Laboratory, California Institute of Technology, Pasadena, California, USA

12 [†] Now Morgan State University, Baltimore, Maryland, USA

13
14 **Corresponding author: Krzysztof Wargan (krzysztof.wargan-1@nasa.gov)**

15 **Key Points:**

- 16 • New composition reanalysis of the stratosphere is introduced.
17 • Microwave Limb Sounderr (MLS) ozone, H₂O, HNO₃, HCl, and N₂O are assimilated for 2004–2021 and
18 will be extended to the present.
19 • Asimilated species agree well with MLS and with independent data.
20
21

22 Abstract

23 MERRA-2 Stratospheric Composition Reanalysis of Aura Microwave Limb Sounder (M2-
24 SCREAM) is a new reanalysis of stratospheric ozone, water vapor, hydrogen chloride (HCl), nitric
25 acid (HNO₃) and nitrous oxide (N₂O) between 2004 and the present (with a latency of several
26 months). The assimilated fields are provided at a 50-km horizontal resolution and at a three-hourly
27 frequency. M2-SCREAM assimilates version 4.2 Microwave Limb Sounder (MLS) profiles of the
28 five constituents alongside total ozone column from the Ozone Monitoring Instrument. Dynamics
29 and tropospheric water vapor are constrained by the MERRA-2 reanalysis. The assimilated species
30 are in excellent agreement with the MLS observations, except for HNO₃ in polar night, where data
31 are not assimilated. Comparisons against independent observations show that the reanalysis
32 realistically captures the spatial and temporal variability of all the assimilated constituents. In
33 particular, the standard deviations of the differences between M2-SCREAM and constituent
34 mixing ratio data from The Atmospheric Chemistry Experiment Fourier Transform Spectrometer
35 are much smaller than the standard deviations of the measured constituents. Evaluation of the
36 reanalysis against aircraft data and balloon-borne frost point hygrometers indicates a faithful
37 representation of small-scale structures in the assimilated water vapor, HNO₃ and ozone fields near
38 the tropopause. Comparisons with independent observations and a process-based analysis of the
39 consistency of the assimilated constituent fields with the MERRA-2 dynamics and with large-scale
40 stratospheric processes demonstrate the utility of M2-SCREAM for scientific studies of chemical
41 and transport variability on time scales ranging from hours to decades. Analysis uncertainties and
42 guidelines for data usage are provided.

43 Plain Language Summary

44 Earth's stratosphere contains a number of trace gases of various origins, chemical properties and
45 lifetimes. In addition to their importance for stratospheric chemistry, including those affecting the
46 ozone layer, and for the planet's radiative budget, the complex geographical and vertical
47 distributions of atmospheric constituents provide invaluable information about stratospheric
48 dynamics and transport in a changing climate. This paper introduces and evaluates a new high-
49 resolution composition data set produced at NASA's Global Modeling and Assimilation Office.
50 Named MERRA-2 Stratospheric Composition Reanalysis of Aura Microwave Limb Sounder (M2-
51 SCREAM), this stratosphere-focused product consists of assimilated global three-dimensional
52 ozone, water vapor, hydrogen chloride, nitric acid, and nitrous oxide fields, all of which are of
53 primary importance to stratospheric chemistry and transport studies. M2-SCREAM uses high
54 quality data from the Microwave Limb Sounder instrument (2004-present) combined with
55 meteorological information from NASA's MERRA-2 reanalysis. Comparisons with independent
56 observations and a process-based analysis of the consistency of the assimilated constituent fields
57 with the MERRA-2 dynamics and with large-scale stratospheric processes demonstrate the utility
58 of M2-SCREAM for scientific studies of chemical and transport variability on time scales ranging
59 from hours to decades.

60 1 Introduction

61 The past decade has witnessed growing scientific interest in the quickly developing field of
62 chemical retrospective analyses (*reanalyses*): multiyear records of assimilated observations of
63 atmospheric constituent gases (Errera et al., 2019; Flemming et al., 2017; Hollingsworth et al.,
64 2008; Innes et al., 2013; 2019; Miyazaki et al., 2015, 2020; van der A et al., 2015). While major
65 multidecadal meteorological reanalyses routinely include ozone and water vapor, their data

66 assimilation systems do not incorporate full chemistry models, and their treatment of stratospheric
67 water vapor is often simplified to the point of rendering that product unsuitable for science (e.g.,
68 Davis et al., 2017; SPARC 2021), with exception of the recent European Centre for Medium-
69 Range Weather Forecasts reanalysis, ERA5 (Hersbach et al., 2020), which has been shown to have
70 a scientifically useful stratospheric water vapor product (Wang et al., 2020; SPARC 2021). In
71 contrast, chemical (or *composition*) reanalyses typically use “full” chemistry models (i.e., ones
72 that explicitly model chemical reactions, rather than parametrizing them) with transport driven by
73 assimilated winds and temperature fields from existing meteorological reanalyses. Composition
74 reanalyses typically include a host of atmospheric constituent fields beyond ozone and water
75 vapor. Most chemical reanalyses focus on tropospheric composition and air quality applications,
76 although some of them, e.g. the Copernicus Atmospheric Monitoring Service (Innes et al., 2019),
77 also provide realistic representations of stratospheric ozone. To our knowledge, the only
78 stratosphere-focused global reanalyses to date are the Belgian Assimilation System for Chemical
79 Observations (BASCOE) Reanalysis of Aura MLS (Microwave Limb Sounder) versions 1 and 2
80 (BRAM and BRAM2; Errera et al., 2019).

81
82 This paper introduces a new chemical reanalysis of stratospheric constituents developed at
83 NASA’s Global Modeling and Assimilation Office (GMAO). Named “M2-SCREAM”, for
84 Modern-Era Retrospective Analysis for Research and Applications, version 2 (MERRA-2; Gelaro
85 et al., 2017) Stratospheric Composition Reanalysis of Aura MLS, this product consists of
86 assimilated global three-dimensional fields of stratospheric ozone, water vapor, hydrogen chloride
87 (HCl), nitric acid (HNO₃), and nitrous oxide (N₂O) mixing ratios, while the tropospheric water
88 vapor and meteorological fields are constrained by MERRA-2. While the model used to produce
89 M2-SCREAM simulates a number of other chemical species, only the five assimilated constituents
90 are evaluated and released to the scientific community at present. The reanalysis horizontal
91 resolution matches the MERRA-2 reanalysis of 0.625° longitude by 0.5° latitude on 72 levels and
92 covers the period of MLS observations from September 2004 to 2022 (March 2022 at the time of
93 writing). The assimilated instantaneous fields are produced at a three-hourly frequency. M2-
94 SCREAM assimilates version 4.2 MLS profiles of the five constituents alongside total column
95 ozone from the Ozone Monitoring Instrument (OMI: Levelt et al, 2006; 2018), using the recently
96 developed Constituent Data Assimilation System (CoDAS: Wargan et al., 2020a,b; Weir et al.,
97 2021). M2-SCREAM provides an accurate and dynamically consistent high-resolution data record
98 of the five constituents, all of which are of primary importance to stratospheric chemistry and
99 transport studies. As an illustration, **Fig. 1** compares tropical stratospheric water vapor from the
100 MERRA-2 and M2-SCREAM reanalyses. Dynamically driven variability in the tropical tape
101 recorder signal (e.g., Davis et al., 2017), especially above 70 hPa, is readily apparent in M2-
102 SCREAM, while only hinted at in MERRA-2. Comparisons with independent observations
103 (**Section 6**) reveal that the M2-SCREAM stratospheric water vapor exhibits realistic variability.

104

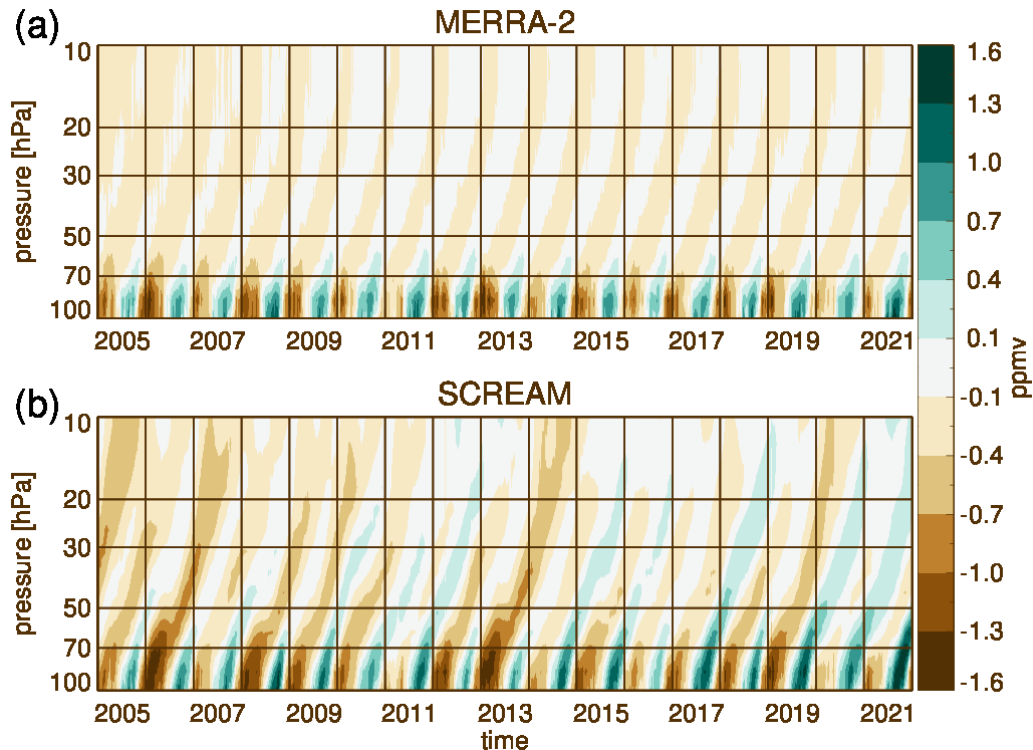


Figure 1: Water vapor anomalies from MERRA-2 (a) and M2-SCREAM (b) averaged between 15°S and 15°N and plotted as a function of time and pressure. A five-day running mean was applied to the data at every pressure level. The anomalies are computed at every level separately by removing the time average.

Building on the theory of data assimilation, this study demonstrates that a (composition) reanalysis product is fundamentally data-driven whereby the information content in the assimilated constituent fields is drawn from observations and these fields constitute a near-optimal estimate of the true atmospheric composition given the assimilated data and their uncertainties (**Section 2**). The utility of composition reanalyses for scientific studies, therefore, lies in the global, high-frequency representation of these constituent fields consistent with the underlying dynamics and chemistry of the real atmosphere.

As our focus is on the scientific utility of this reanalysis product, we have taken several steps intended to guide the users. Specifically, we derive and provide monthly sets of uncertainties for each of the assimilated species and flag the areas where the confidence in the assimilation output is low. Furthermore, we evaluate and discuss the suitability of the reanalysis fields for scientific applications by focusing not only on comparisons with independent observations but also on process-based analysis.

The remainder of the sections are organized as follows. Description of the GEOS Constituent Data Assimilation System (CoDAS) is provided in **Section 3**. Data sources assimilated in M2-SCREAM and those used for evaluation of the reanalysis are described in **Section 4**. **Section 5** discusses the internal consistency of the reanalysis. **Section 6** describes and discusses validation of the reanalysis against independent observations as well as process-based evaluation. **Section 7** discusses confidence in the M2-SCREAM output and contains some recommendations for users.

132 A summary of this study is given in **Section 8**. Three appendices discuss (A) the uncertainty
 133 estimation, (B) a technical correction applied to the reanalysis output, and (C) the contents of the
 134 M2-SCREAM output provided to the users.

135 **2 Theoretical motivation for constituent data assimilation**

136 This section provides a high-level overview of the theory of constituent data assimilation with
 137 emphasis on those of its aspects that motivate the methodological choices of M2-SCREAM and
 138 their scientific application. In what follows the term *data assimilation* is taken to mean constituent
 139 data assimilation. We do not consider meteorological assimilation in this study other than in the
 140 context of driving the model by assimilated winds and temperatures. Furthermore, by *model* we
 141 mean a specified dynamics general circulation model (GCM) forced by assimilated meteorology
 142 and integrated with a chemistry module. Throughout the paper we will use the terms *analysis* and
 143 *analyzed* for constituent fields obtained through the procedure described in this section; we will
 144 use the words *assimilation* and *assimilated* for the final product computed by CoDAS using the
 145 Incremental Analysis Update (IAU: Bloom et al., 1996) described in Section 3. Only the
 146 assimilated fields are archived and distributed to users.

147
 148 Data assimilation seeks to estimate the probability distribution of global gridded constituent fields
 149 x_n at time t_n given a set of observations $y_{1:n} = \{y_1, y_2, \dots, y_n\}$ of functions H_1, H_2, \dots, H_n of the
 150 states x_1, x_2, \dots, x_n . A data assimilation system (DAS) does this by tracking and updating the
 151 probability density function (pdf) $p(x_n | y_{1:n})$ of the state x_n conditioned on all current and past
 152 observations $y_{1:n}$ as new data arrive. Using Bayes' theorem,

$$153 \quad p(x_n | y_{1:n}) \propto p(y_n | x_n) p(x_n | y_{1:n-1}), \quad (1)$$

154
 155 where $p(y_n | x_n)$ is the probability density of observing y_n given x_n , the prior is the pdf
 156 $p(x_n | y_{1:n-1})$ of x_n given *all previous observations*, and the posterior is the pdf $p(x_n | y_{1:n})$ after
 157 conditioning on the new observations y_n . Sequential filtering methods further decompose the prior
 158 into its forecast and initialization components using the assumed Markov property of the state to
 159 give the recursion relation
 160

$$161 \quad p(x_n | y_{1:n}) \propto p(y_n | x_n) \int p(x_n | x_{n-1}) p(x_{n-1} | y_{1:n-1}) dx_{n-1}$$

162
 163 for the posterior $p(x_n | y_{1:n})$ in terms of its value at the previous time t_{n-1} , $p(x_{n-1} | y_{1:n-1})$. See
 164 Jazwinski (1970), Theorem 6.4 for more details.
 165

166 Assuming all the distributions are Gaussian, we can define the cost function
 167

$$168 \quad J_n(x) = (y_n - H_n x)^T R^{-1} (y_n - H_n x) + (x - x_n^b)^T B^{-1} (x - x_n^b), \quad (2)$$

169
 170 such that $p(x_n | y_{1:n}) \propto \exp[-\frac{1}{2} J_n(x_n)]$, where R is the error covariance of $p(y_n | x_n)$, B the
 171 error covariance of $p(x_n | x_{n-1})$, and $x_n^b = M(x_{n-1}^a)$ is the *background* (or *forecast*) state from
 172 the mean (or mode) x_{n-1}^a of the previous pdf $p(x_{n-1} | y_{1:n-1})$ propagated forward by the model
 173 M . For notational convenience, from here on we will drop the time index subscript n when not
 174

175 needed and treat the observation operator as its Jacobian matrix at x_n^a . The *analysis*, x^a , is defined
 176 as the state that minimizes the cost function $J(x)$. It is thus the mean/mode of the posterior pdf
 177 (Nichols et al., 2010; Lahoz and Schneider 2014) and usually serves as the initial condition for the
 178 background x^b at the next timestep. However, in M2-SCREAM the initial condition is, instead,
 179 the assimilated state obtained from background and analysis through the IAU procedure described
 180 in the next section. In either case it follows that x^a is the maximum likelihood estimate of the true
 181 state of the constituent fields given available data valid at steps $t_n, t_{n-1}, t_{n-2}, \dots$. By definition,
 182 it satisfies the equation

$$183 \quad x^a = x^b + BH^T(HBH^T + R)^{-1}(y - Hx^b), \quad (3)$$

184
 185
 186 On digital computers, Equation 3 can be solved for by storing x^b and x^a as vectors of constituent
 187 mixing ratios defined on the three-dimensional model grid and y as a vector whose length is the
 188 number of observations. Since at half-degree resolution over the entire globe the matrix B would
 189 require over 2 petabytes of memory to store outright, we solve for x^a using a conjugate gradient
 190 method that needs only to multiply by R and B . The sequential filtering approach has the added
 191 advantage that it does not need to store previous values of the state and observations. For further
 192 discussion, including typical assumptions and simplifications made in a DAS see, e.g. Jazwinski
 193 (1970), Cohn (1997), Nichols et al. (2010), Weir et al. (2013), Lahoz and Schneider (2014), and
 194 Reich (2019). The remainder of this section explores several important points that follow from the
 195 formulation outlined above.

196
 197 It follows from Equation (1) that data assimilation is fundamentally an observation-driven
 198 methodology. The role of the model is limited to the time propagation of the cumulative
 199 information from past observations in accordance with the governing equations of motion. If
 200 spatio-temporal data coverage is sufficient (i.e., if the state is *completely observable* with respect
 201 to the given observations; see Jazwinski 1970 pp. 231–234) then the initial condition for the model
 202 integration over each assimilation cycle (six-hourly in our case) is purely the result of previously
 203 assimilated observations up to unavoidable uncertainties, and consequently, approximates the *true*
 204 constituent fields in contrast to a *possible realization* of that state as is the case in pure model
 205 simulations. In fact, assimilation is useful precisely because, and to the degree that, its output's
 206 information content is derived from observations. We emphasize this point because it is sometimes
 207 stated that assimilated fields are a “blend” of data and model output, which leads to concerns about
 208 what assimilated products represent. **Figure 2** illustrates the concept of data assimilation as driven
 209 by observations. Shown are the global ozone and HNO₃ analyzed fields interpolated from the M2-
 210 SCREAM native level output onto the 500-K potential temperature surface. The circles show the
 211 assimilated MLS observations within the six-hourly time window around the analysis time. It is
 212 readily seen that the ozone observations agree very well with the assimilated field (**Fig. 2a**), as
 213 expected from relatively small observation uncertainties. Precision and accuracy of the constituent
 214 field away from the current observations is measured by observation minus “forecast” (O-F)
 215 residuals and is shown to be high given the assumed uncertainties (**Section 5**). The considerable
 216 advantage of having a high-resolution global gridded field constructed from past observations
 217 propagated with the model is evident from the high level of detail seen in the figure, including
 218 complex dynamically driven features.

219

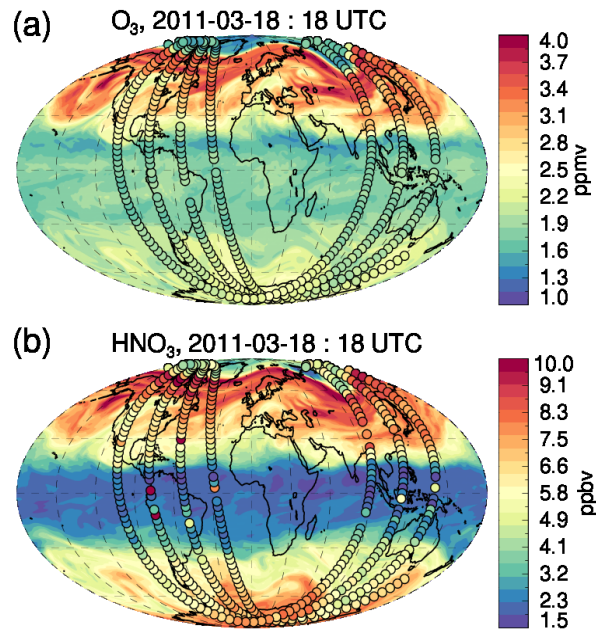


Figure 2: Assimilated ozone (a) and HNO₃ (b) on 18 March 2011, 18 UTC, interpolated to the 500-K potential temperature surface. MLS observations are overplotted using the same color scheme as circles.

Data assimilation is a probabilistic methodology. Observation and background (prior) uncertainties play a critical role. In **Fig. 2(b)**, the agreement between the observations and the assimilated HNO₃ field is less close than for ozone: several observed values depart from the assimilated field and appear inconsistent with the average concentrations in the adjacent regions, particularly in the tropics. This is expected from the relatively high observation uncertainties for MLS HNO₃ (Livesey et al., 2020), that is, a large spread in $p(y_n | x_n)$. Noise in the data is effectively filtered out as a result. The posterior pdf, $p(x_n | y_{1:n})$, can be estimated from the internal statistics of the DAS under suitable assumptions (Desroziers et al., 2005). Using this method, we calculate monthly standard deviations of the posterior pdfs as well as overall estimates of uncertainties for M2-SCREAM (**Appendix A**). These diagnostics are provided to the users in the form of monthly estimates.

In regions of the atmosphere where observations are not assimilated (for example in the middle and lower troposphere unobserved by MLS or during infrequent prolonged data outages) the output fields produced by the DAS can no longer be thought of as data-driven and are more akin to the results of a chemistry model simulation forced by assimilated meteorology. Even in those situations it is expected that observational information content is propagated to some extent into unobserved regions by model transport. Our previous work (Wargan et al., 2020a; 2020b) indicates that assimilation results are valid at all latitudes including the poles despite the MLS coverage boundaries at 82°. Additionally, we demonstrate in **Section 6.1** good qualitative agreement with independent data several kilometers below the tropopause. However, except in the cases delineated above we do not evaluate M2-SCREAM over unobserved regions and do not recommend its use for scientific studies far outside of areas covered by MLS observations. We provide monthly

248 gridded files that contain uncertainty estimates and that flag the regions of the atmosphere not
249 covered by observations. We also provide some additional recommendations in **Section 7**.

250 **3 GEOS Constituent Data Assimilation System (CoDAS)**

251 The GEOS Constituent Data Assimilation System (CoDAS) is an extension of the GEOS
252 Atmospheric Data Assimilation System (ADAS; Todling and El Akkroui, 2018) and is capable
253 of assimilating observations of any trace gas simulated by any of several GEOS-compatible
254 chemistry modules. Originally derived from the ozone assimilation code of MERRA-2 (Wargan
255 et al., 2017), CoDAS generalizes those capabilities to arbitrary collections of trace gases with
256 generic averaging kernel and in situ observation operators capable of ingesting nearly every known
257 space-based trace gas retrieval. Current applications include stratospheric (Wargan et al. 2021a,b)
258 and carbon (Weir et al., 2021) constituent assimilation systems with ongoing research
259 incorporating reactive tropospheric gases that determine air quality from a full tropospheric and
260 stratospheric chemistry module. Through its ADAS lineage, CoDAS inherits a suite of assimilation
261 methodologies including three- and four-dimensional variational, ensemble, and hybrid methods
262 for estimating the posterior pdf (Equation 1). For simplicity, we use three-dimensional variational
263 (3DVar) formulation and Gridpoint Statistical Interpolation (GSI; Wu et al., 2002) to discretize
264 the atmospheric state x onto a regular, horizontal grid and η -level vertical coordinates, resulting in
265 the cost function in Equation (1).

266
267 The theoretical success of data assimilation owes to two fundamental factors: 1) the power of
268 recycling previous data into each new background as described in **Section 2**, a result that follows
269 from Bayes' theorem of the 1700s, and 2) that data differences from a prior background tend to
270 have much simpler statistics than the data values themselves, a result known since at least the
271 1950s (Bergthórsson and Döös, 1955). The latter follows from the fact that differencing data and
272 a model can produce a random variable whose statistics are far more smooth in space and regular
273 in time than the data themselves, which can have complex and chaotic behavior. Nevertheless, the
274 practical success of data assimilation relies heavily upon the modeling of the error statistics,
275 namely the covariance B of the background errors and R of the observation errors, which are
276 assumed here to be either additive or multiplicative for simplicity. Since these matrices are far too
277 large to store in memory, we represent them as transformation operators. Simplifying assumptions
278 about error statistics then translate to simpler, and faster, representations as transformations. We
279 use a background error covariance B whose variances and horizontal correlation lengths are
280 constant horizontally. With the exception of ozone, these values are constant vertically as well.
281 Vertical background error correlation is estimated from the vertical correlation length of the
282 modeled values and thus varies in space and time. CoDAS supports log-normal, i.e., multiplicative,
283 error distributions which are used for stratospheric water vapor, HCl, and HNO₃ (see **Table 1**).
284 Using multiplicative errors introduces some “flow-dependence” in the error statistics since they
285 are proportional to the background values. We use an observation error covariance R that is the
286 reported retrieval error (precision and accuracy combined) multiplied by a scaling factor that varies
287 by level. These numbers are all tuned using repeated applications of the Desroziers et al. (2005)
288 diagnostics.

289
290 Data are assimilated over 6-hour windows centered on “off-synoptic” times (e.g. 21Z) and are
291 cycled back into the model by adding the average analysis minus background increment to
292 simulated tracer values over the window length. This is similar to the IAU used for the

293 meteorological variables of MERRA-2. While there are advantages to 4DVar and ensemble
294 capabilities in the ADAS (e.g., Skachko et al. 2016), here we use 3DVar and note that refinement
295 of its window length, e.g., to an hour, can impart any desired “flow-dependence” to the increments;
296 furthermore, with the computational costs of simulating full chemistry, it is not currently within
297 the scope of this product to use 4DVar. Research is underway to evolve background error standard
298 deviations rather than the simplified approach of taking them to be proportional to the state as done
299 here (Ménard et al. 2021; Gilpin et al. 2022).

300

301 The model used in the present configuration of CoDAS is a version of GEOS GCM (Icarus-
302 3_2_p9) integrated with the stratospheric chemistry module, StratChem (Nielsen et al., 2017 and
303 references therein). This model configuration is the same as that used by Wargan et al. (2020b).
304 The meteorology in the GCM is constrained by the MERRA-2 reanalysis output of temperature,
305 surface pressure, tropospheric (but not stratospheric) water vapor, and winds (GMAO 2015) via
306 the *replay* methodology unique to GEOS and described in detail by Orbe et al. (2017). The
307 dynamical and temperature fields in M2-SCREAM are, therefore, very similar to those in
308 MERRA-2 (not shown). Differences that arise from the upgrades to the GCM used to produce M2-
309 SCREAM since MERRA-2 and from the radiative impacts of assimilated ozone and water vapor
310 are small in the stratosphere (not shown). Below the tropopause, water vapor is replayed to the
311 MERRA-2 analysis, and thus constrained by MERRA-2 within the troposphere but not above it.

312

313 The StratChem module is a family chemistry scheme that simulates 125 gas-phase and 35
314 photolysis reactions important in the middle atmosphere. These include gas-phase and
315 heterogeneous chemistry of the chlorine, bromine and nitrogen families. The reaction rates follow
316 Burkholder et al. (2015). There are 51 transported and 18 inferred species. Polar stratospheric
317 clouds (PSCs) are parameterized following Considine et al. (2000). We refer the reader to Wargan
318 et al. (2020b) for further details of the model setup.

319

320 For technical reasons related to the current implementation of the PSC scheme in StratChem
321 discussed in further detail in Section 5, HNO₃ is not assimilated in regions where model-generated
322 PSCs are present. We recommend that lower-stratospheric HNO₃ from M2-SCREAM during polar
323 night be avoided in scientific studies. Further recommendations regarding HNO₃ are given in
324 **Section 8**. This work also used an MLS observation operator with a bug that mistook model layer
325 centers for layer edges which slightly offset the placement of the observations. Given the vertical
326 resolution of the model compared to MLS profiles, the impact was small and has been successfully
327 corrected in post-processing (**Appendix B**).

328 **4 Data**

329 **4.1 Assimilated observations**

330 MLS on NASA’s Aura satellite (Waters et al., 2006) is a microwave limb sensor that measures
331 thermal emission of the atmosphere in a range of spectral bands allowing retrieval of the profile
332 information of many atmospheric constituents from the upper troposphere through the mesosphere.
333 The instrument makes day and night measurements between 82°S and 82°N along 15 orbits per
334 day. At the time of writing, the MLS mission covers 17 years of nearly uninterrupted
335 measurements (**Section 7**) since late 2004. The MLS observations have provided and continue to
336 provide invaluable information on stratospheric composition, its changes and variability.

337
 338 M2-SCREAM assimilates version 4.2 ozone, water vapor, HCl, HNO₃ and N₂O data from MLS
 339 (Livesey et al., 2020). **Table 1**, similar to that provided in Wargan et al. (2020b), specifies the
 340 vertical extent and resolution of the assimilated profiles. As many details of the MLS data
 341 treatment are the same as in Wargan et al. (2020b), here we summarize it briefly and focus on the
 342 most important facts and the long-term behavior of these data. The observation uncertainties for
 343 ozone are as those used in MERRA-2 (Wargan et al., 2017) and those for the other species were
 344 tuned using the method described in Desroziers et al. (2005). Recommended quality screening
 345 (Livesey et al., 2020) is applied to all MLS observations prior to assimilation.

346
 347 **Table 1.** *Treatment of MLS observations and the model background and observation errors.*
 348 *Values in column “B” for all species except N₂O are factors used to scale the background state,*
 349 *x^b , to obtain the background uncertainty standard deviation. For N₂O we use a constant*
 350 *background uncertainty of 8ppbv. The column “R” lists the ranges of scaling factors applied to*
 351 *the reported MLS uncertainties.*

Constituent	Vertical range	Vertical resolution in lower to middle stratosphere	B	R	Remarks
Ozone	216 – 0.1 hPa	2.5 – 3 km	5%	100%	
HCl	100 – 0.32 hPa	3 km	10%	30–100%	
N ₂ O	68 – 0.46 hPa	4 – 6 km	8 ppb	23–75%	Significant drift exists (Livesey et al., 2021)
Water vapor	261 – 0.01 hPa (model top)	1.5 – 3 km	6%	37–760%	Drift and wet bias in the stratosphere (Livesey et al., 2021)
HNO ₃	216– 1.5 hPa	4 – 4.5 km	10%	30–70%	HNO ₃ is not assimilated in regions where model-generated PSCs are present due to technical reasons related to the current implementation of the PSC scheme in GEOS.

352
 353 The MLS version 4.2 N₂O and water vapor, both retrieved from the 190 GHz band, suffer from
 354 known altitude dependent drifts in the period after 2010 (Livesey et al., 2021). Evaluated against
 355 other satellite data, the drift in water vapor is positive and ranges from 2–3% per decade in much
 356 of the stratosphere to 5% and more at 50 hPa. Additionally, the version 4.2 water vapor is found
 357 to be biased high with respect to the latest version (version 5) by about 10% (Livesey et al., 2022).

358 The post-2010 drift in N₂O is negative. It is confined to the lower stratosphere (LS) but it is larger
359 than the drift in water vapor, up to 15%. The other three assimilated species, ozone, HCl, and
360 HNO₃, have been found to be stable for the duration of the MLS mission (Livesey et al., 2020).

361
362 M2-SCREAM was already well in production when version 5 of MLS data became available
363 (Livesey et al., 2022). The water vapor drift has been significantly reduced in version 5, but some
364 bias in N₂O remains (Livesey et al., 2021). Comparisons with independent data suggest that the
365 moderately high bias in stratospheric water vapor seen in version 4.2 has been eliminated in version
366 5. We compare M2-SCREAM with MLS version 5 observations in **Section 5**.

367
368 As described in Wargan et al. (2020a,b), M2-SCREAM also assimilates total ozone observations
369 from the OMI sensor (Levelt et al., 2006; 2018). These observations provide an additional
370 constraint on the analyzed ozone, as demonstrated in the previous GEOS DAS systems described
371 by Wargan et al. (2015; 2017; 2020a,b) and Ziemke et al. (2015).

372 **4.2 Independent observations**

373 This subsection describes the independent (that is, not assimilated) data used to evaluate M2-
374 SCREAM. The Atmospheric Chemistry Experiment Fourier Transform Spectrometer (ACE-FTS)
375 on Canada's SCISAT-1 satellite (Bernath et al., 2005; Bernath 2017) is a solar occultation sensor
376 that provides sunrise and sunset measurements in multiple infrared channels, allowing accurate
377 retrievals of many trace gases including ozone, water vapor, HCl, HNO₃, and N₂O. The instrument
378 provides 30 high vertical resolution profiles per day. The coverage varies significantly with season,
379 with most measurements taken at mid- and high latitudes. However, annually aggregated ACE-
380 FTS data provide near-global coverage that is sufficient for reanalysis evaluation. We use version
381 4.1 ACE-FTS retrievals (Boone et al., 2020) with additional screening applied using sets of quality
382 flags provided by the instrument team (Sheese et al., 2015; Sheese et al., 2020). Version 3.5 ACE-
383 FTS had an average estimated dry bias of ~5% in the middle-to-upper stratosphere and the lower
384 mesosphere (Sheese et al. 2017); their Fig 3 suggests a bias close to 10% near the stratopause. Our
385 results in **Section 6.3** suggest that some of this bias persists in version 4.1.

386
387 Another solar occultation sensor, the Stratospheric Aerosol and Gas Experiment III instrument,
388 was installed on the International Space Station (SAGE III/ISS) in February 2017. The SAGE
389 III/ISS is in a low earth orbit with an inclination angle of 51.6° and a measurement range from
390 about 70°S to 70°N (Wang et al., 2020). Ozone, water vapor, aerosols and other trace gases are
391 retrieved from solar occultation measurements on a 1-km grid for both sunrise and sunset. In this
392 study, version 5.2 of the SAGE III/ISS water vapor product is used, interpolated to a 0.5-km
393 vertical grid (Davis et al., 2021). SAGE III/ISS water vapor profiles are filtered according to Davis
394 et al. (2021) to remove cloud interference in the troposphere and retrieval anomalies in the upper
395 stratosphere and mesosphere. Unlike previous versions of SAGE data, version 5.2 water vapor
396 profiles are not smoothed vertically, resulting in substantial noise within an individual profile.

397
398 We use observations of water vapor, ozone, and HNO₃ retrieved from the measurements made by
399 the Gimballed Limb Observer for Radiance Imaging of the Atmosphere (GLORIA) instrument
400 flown on the German High Altitude and Long Range Research Aircraft (HALO) during the joint
401 Polar Stratosphere in a Changing Climate, Gravity Wave Life Cycle Experiment, and Seasonality
402 of Air mass transport and origin in the Lowermost Stratosphere using the HALO Aircraft

403 campaigns (hereafter, PGS, Johansson et al., 2018). The GLORIA sensor (Friedl-Vallon et al.,
 404 2014) is an imaging Fourier transform spectrometer measuring thermal emissions of the
 405 atmosphere in the infrared. The data used in this study are made possible by high spectral
 406 resolution measurements taken every 13 seconds at the nominal vertical resolution of 250 m. The
 407 actual vertical resolution ranges from about 0.5 km to 1 km, finer than that of the assimilated fields
 408 (~1.1 km in the upper troposphere and lower stratosphere, *UTLS*). The PGS campaign consisted
 409 of 15 HALO flights in the North Atlantic region between 21 December 2015 and 18 March 2016.
 410 The timing of the campaign fortuitously coincided with one of the coldest Arctic polar vortex
 411 seasons that featured significant denitrification, dehydration, and ozone depletion (Manney and
 412 Lawrence 2016; Khorsawi et al., 2017), making it a good test case for the reanalysis.

413
 414 Frost Point Hygrometers (FPH) are balloon-borne instruments that measure atmospheric water
 415 vapor content by maintaining a stable thin layer of ice on a temperature-controlled mirror
 416 monitored by an infrared LED beam. The moisture content is derived from the temperature of the
 417 mirror at thermodynamic equilibrium (Hurst et al., 2014). This technology allows accurate
 418 measurements of specific humidity in the stratosphere well above the altitudes where humidity
 419 measurements from radiosondes are suitable for scientific use. We show comparisons between the
 420 M2-SCREAM water vapor and National Oceanic and Atmospheric Administration’s FPHs
 421 stations that provide multidecadal record: Lauder, New Zealand (169.68°E, 45.04°S), Hilo, Hawaii
 422 (155.05°W, 19.72°N), and Boulder, CO, USA (105.2°W, 39.95°N). 181, 120, and 277 profiles of
 423 specific humidity are available from Lauder, Hilo, and Boulder, respectively, between 2005 and
 424 2020. The vertical resolution of the FPH measurements is 5-10 m. Here, we use data sets averaged
 425 in 250-m layers and further map them onto a 1-km vertical grid by averaging within each layer.

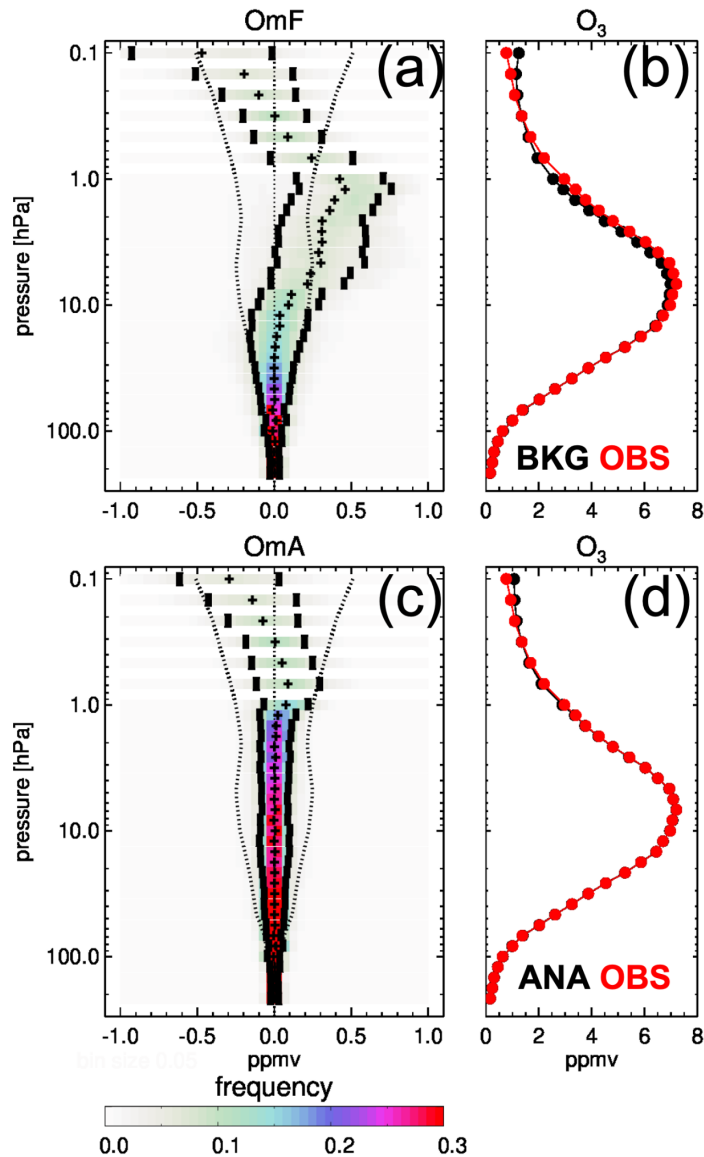
426
 427 All comparisons of M2-SCREAM against MLS and the independent data sets are presented in
 428 terms of mixing ratios rather than as relative to the observed values. While relative differences
 429 expressed in percent can be useful in other contexts, we find that they are often misleading when
 430 used in discussions of constituents. As trace gas variability spans more than one order of
 431 magnitude, areas of very low concentrations are dominated by random noise, producing
 432 exceedingly large relative differences when the actual differences simply reflect the instrument
 433 precision.

434 **5 Internal statistics and agreement with MLS observations**

435 For every observation CoDAS calculates the corresponding O-F, i.e., $y - H(x^b)$, that is the
 436 discrepancy between the observed constituent mixing ratio and the background value from a six-
 437 hourly integration of the model initialized with the result of the previous assimilation cycle.
 438 Although inconsistent with the superscript “b” for background, we use here the traditional “F” for
 439 “forecast” in the term “O-F”. At the end of a given cycle the system computes the observation
 440 minus analysis (O-A) departure, $y - H(x^a)$. On average, the latter are expected to be closer to
 441 zero than the corresponding O-Fs. The mean and standard deviation of the O-Fs represent the
 442 combined uncertainty of the background field and the uncertainty of the observations (Desroziers
 443 et al., 2005, their equation 1). The success of assimilation critically depends on the ability of the
 444 model to propagate information from observations forward in time over the length of the
 445 assimilation window, that is, the model error accumulated over the integration period should be
 446 small. Therefore, O-Fs represent a valuable diagnostic of the performance of the DAS.

447

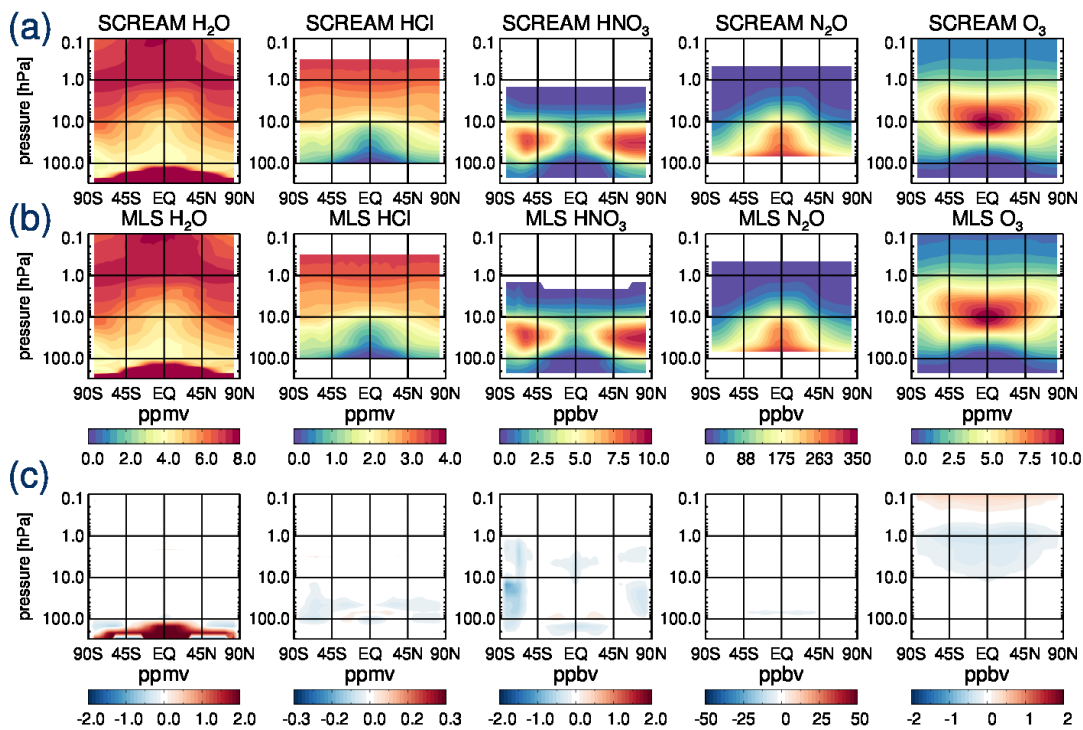
448



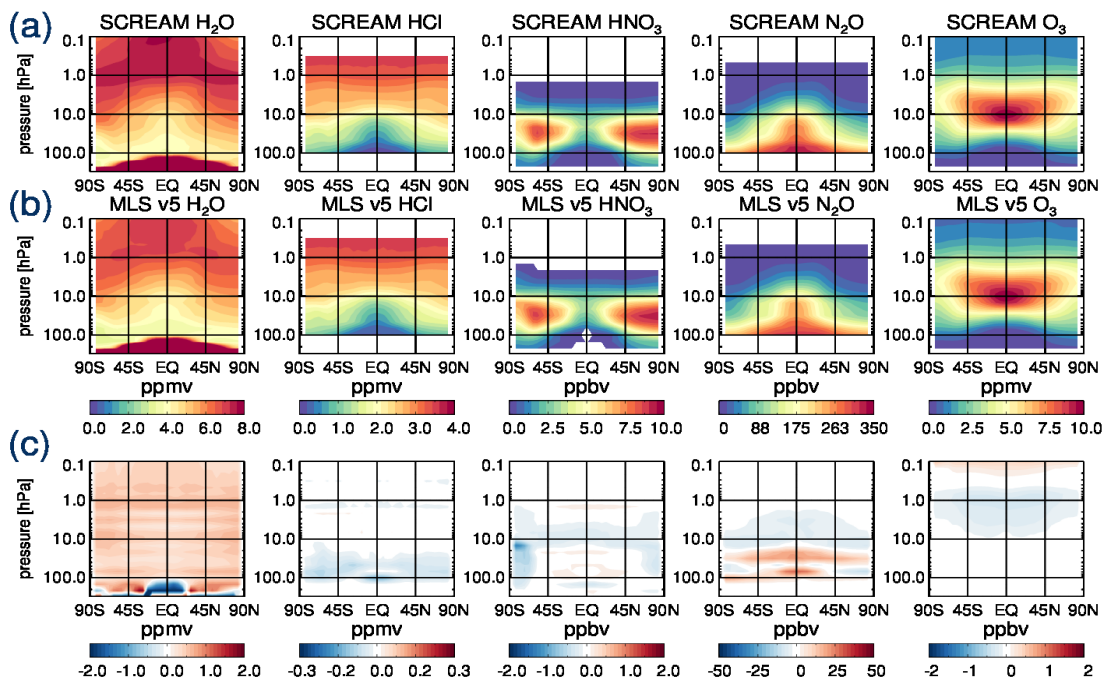
449 **Figure 3:** Global M2-SCREAM O-F (a,b) and O-A (c,d) statistics for MLS version 4.2 ozone.
 450 Panels (a) and (c) show the O-F and O-A statistics: the mean (plus signs), standard deviations
 451 around the mean (short vertical bars), probability density functions (colors) at the MLS levels from
 452 216 to 0.1 hPa. The dotted lines are plus/minus MLS uncertainty estimates. Panels (b) and (d)
 453 show mean background, "BKG" (b) and analysis, "ANA" (d) profiles (black) and mean MLS
 454 observed profiles (red) at the same pressure levels.
 455

456 **Figure 3** illustrates the O-F and O-A statistics for M2-SCREAM ozone calculated globally in
 457 January 2005. The statistics do not vary significantly from month to month. O-F and O-A pdfs are
 458 shown along with their mean, median, and standard deviation around the mean at each MLS
 459 pressure level. Additionally, the figure plots MLS uncertainty estimates derived from the relevant
 460 table in Livesey et al. (2020) as the square root of the sum of squares of the reported precision and
 461 accuracy, the latter multiplied by 0.5. For pressures greater than 10 hPa, the O-Fs show very little
 462 bias and approximately Gaussian distributions, with standard deviations comparable to the
 463

464 observational uncertainty estimates. There is, however, a pressure dependent bias in the upper
465 stratosphere and the mesosphere. Also evident is an increase in the O-F spread with altitude. In
466 contrast, the O-As exhibit a much smaller bias (near-zero throughout the stratosphere, up to 1 hPa)
467 and standard deviations are within the observational uncertainties. A comparison of the two panels
468 of **Fig. 3** reveals that while assimilation updates bring the assimilated ozone mixing ratio close to
469 the observed values, that information is not fully retained during the six-hourly model integration
470 in the upper atmosphere. This behavior arises because characteristic timescales for stratospheric
471 ozone chemistry rapidly decrease with altitude and become on the order of one hour or less at the
472 higher levels (Brasseur and Solomon, 2005). Short constituent lifetimes pose a challenge to data
473 assimilation, which relies on a cumulative effect of observations as noted in **Section 2**. For this
474 reason, the BRAM2 reanalysis does not assimilate ozone at pressures smaller than 4 hPa (Skachko
475 et al., 2016; Errera et al., 2019). We have made a choice to assimilate MLS ozone at pressures of
476 0.1 hPa or greater in M2-SCREAM. However, users should treat upper-stratospheric ozone from
477 the reanalysis with caution. Unlike ozone, the lifetimes of water vapor, HCl, HNO₃, and N₂O are
478 sufficiently long for the observational information to propagate and accumulate. The O-Fs for all
479 four constituents exhibit negligible bias and their standard deviations are within the MLS
480 uncertainty estimates (**Figure S1**). Note that the MLS uncertainties shown in these figures are
481 global estimates, not the observation-by-observation estimates provided with the data, and
482 therefore are not necessarily strictly larger than the observational uncertainties even though the O-
483 Fs include a contribution from the background as well as from observation uncertainties.
484 Furthermore, the uncertainty estimates derived using Desroziers' formula and used in CoDAS are
485 typically 50 to 70% of those in the MLS data files. As expected, the O-As (not shown) are reduced
486 compared to the O-Fs, indicative of the internal consistency of the data assimilation system.
487 Compared to the mean observed values, the MLS uncertainties (and the O-F standard deviations)
488 for HCl, HNO₃, and N₂O are substantially larger than those for ozone and H₂O, suggesting more
489 "noisy" observations. That is consistent with our discussion of **Fig. 2(b)**. Overall, the O-F results,
490 except for ozone in the upper stratosphere and above, demonstrate excellent performance of the
491 reanalysis in terms of the agreement with the assimilated data and the ability of CoDAS to retain
492 and propagate information from observations forward in time.
493



494
 495 **Figure 4:** Zonal mean mixing ratios of the assimilated constituents calculated from M2-SCREAM
 496 sampled at the MLS observation locations (a) and MLS version 4.2 data (b). The M2-SCREAM
 497 minus MLS differences are shown in (c). All quality-screened MLS data between 2005 and 2021
 498 are used.
 499



500
 501 **Figure 5:** As in Figure 4 but with MLS version 5.0 data.
 502

503 Next, we compare the zonal means of the M2-SCREAM constituents with observations from MLS
 504 version 4.2 (assimilated, Fig. 4) and version 5 (Fig. 5). Both comparisons use quality-filtered MLS

505 observations between 2005 and 2021 and M2-SCREAM profiles subsampled at the observation
506 locations within three hours of observation times. As expected, the differences between M2-
507 SCREAM and MLS version 4.2 are small overall except for water vapor in the troposphere and
508 HNO₃ in the polar regions. Water vapor below the tropopause is constrained by MERRA-2 through
509 replay (**Section 3**), thus less constrained by MLS. In addition, discrepancies among different data
510 sources are typically large in the upper troposphere because of very sharp vertical gradients of
511 specific humidity there. As explained in Section 3, CoDAS does not assimilate HNO₃ in the
512 presence of (model) PSCs, and there is a tendency in the model to overestimate nitric acid
513 condensation, leading to the high latitude biases seen in **Fig. 4**. Despite deficiencies in the
514 StratChem representation of HNO₃ under PSC conditions, other constituents are modeled with
515 sufficient skill to serve as background conditions during PSC and ozone hole conditions. Small
516 differences in HNO₃ between 10 hPa and 1 hPa are consistent with larger MLS uncertainties. There
517 is a small pressure-dependent ozone bias at pressures below 10 hPa. That may seem surprising
518 given that there is no significant bias in the O-As (**Fig. 3**). However, this bias results from the bias
519 in O-Fs discussed above. The application of the IAU (**Section 3**) results in only one half of the
520 analysis increment being applied at the center time of an assimilation window. Consequently, the
521 systematic differences seen in **Fig. 4(c)** can be thought of as being half way between the mean O-
522 F and O-A.

523
524 Most differences between **Figs 4** and **5** reflect known differences between the two versions of the
525 MLS retrievals and are small for ozone, HCl, and HNO₃. The stratosphere is overall drier in version
526 5.0 than in version 4.2, with the latter understood to be too wet (Livesey et al., 2021). The largest
527 differences between the two figures are seen in N₂O. Recall that N₂O observations are assimilated
528 down to 68 hPa and we do not advise scientific use of the reanalysis N₂O at pressures larger than
529 about 70 hPa. There are also significant differences in MLS N₂O between the two versions that
530 result in part from a reduction of an unphysical drift (toward lower values) present in the older
531 version assimilated here.

532
533 We have also examined the differences between M2-SCREAM and BRAM2 (**Fig. S2**). Overall,
534 the zonal means agree very well between the two reanalyses, both of which assimilate the same
535 data. The differences in HCl and HNO₃ are similar in spatial pattern and in magnitude to those
536 shown in **Fig. 4**. The only noteworthy difference of up to 0.5 ppmv between the two reanalyses is
537 seen in ozone at pressures lower than 4 hPa, where BRAM2 is not constrained by data and M2-
538 SCREAM is only weakly constrained by MLS due to the fast ozone chemistry at those pressures.

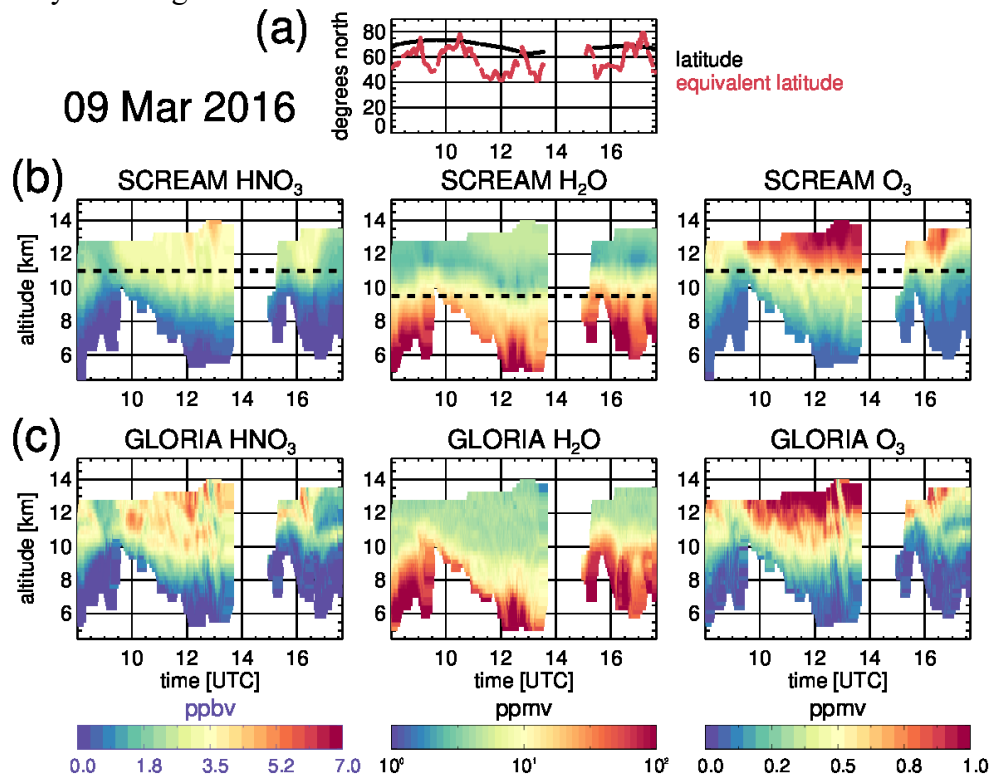
539
540 Overall, the results presented above demonstrate internal consistency of the reanalysis and its close
541 agreement with the assimilated MLS data within observational uncertainties. Comparisons against
542 the improved version 5 MLS retrievals help diagnose spatially varying biases, especially in
543 assimilated water vapor and N₂O.

544 **6 Comparisons with independent observations**

545 **6.1 Representation of small-scale structures**

546 We begin the evaluation of M2-SCREAM with a qualitative comparison of the reanalysis HNO₃,
547 water vapor, and ozone with the observations made by the GLORIA instrument during a single
548 flight on 9 March 2013 (**Fig. 6**, more examples are given in **Figs S3–S16**). The reanalysis

549 constituents are interpolated to the GLORIA vertical levels for each measurement and each level
 550 separately because the geolocations of the measurement tangent points vary significantly with
 551 altitude. The UTLS is a particularly challenging region for the reanalysis because this is where
 552 MLS uncertainties are typically larger than at higher altitudes and no observations are assimilated
 553 below about 10 km. While we assign significantly lower confidence to the constituent profiles
 554 below the bottom of the MLS profiles (marked as dashed lines in **Fig. 6**), we still expect the
 555 constituent fields' features to be consistent with the real dynamics of the atmosphere at those
 556 altitudes because the model is driven by assimilated MERRA-2 meteorology. Since the spatial and
 557 temporal resolution of the aircraft data is significantly higher than that of M2-SCREAM, we do
 558 not expect the reanalysis to capture many of the small-scale features seen in GLORIA observations
 559 such as gravity wave signatures in the constituent fields.



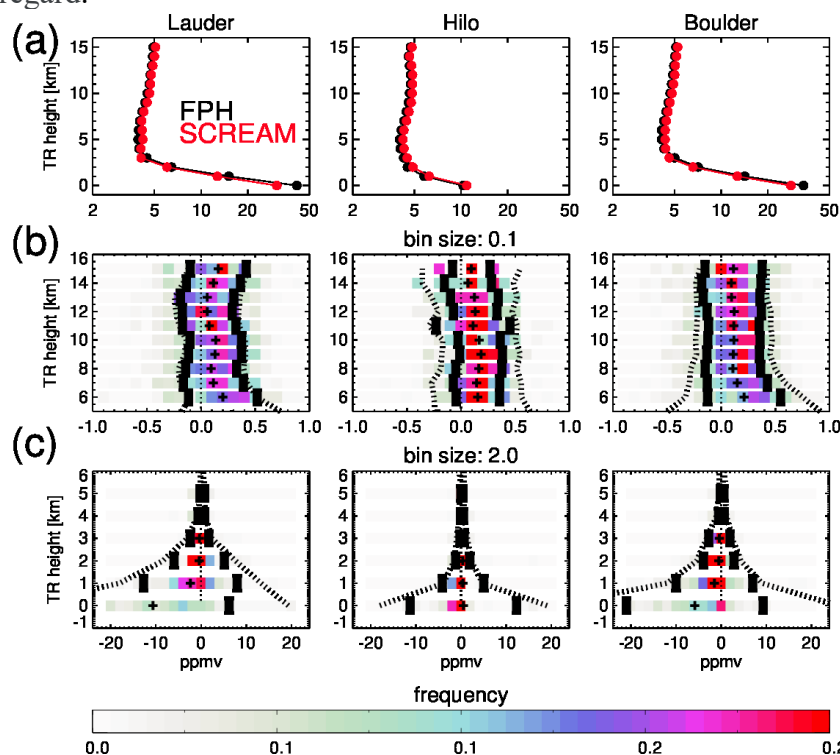
560
 561 **Figure 6:** (a) Latitudes and equivalent latitudes of the GLORIA measurements at 10 km. (b) M2-
 562 SCREAM HNO₃, water vapor, and ozone collocated with GLORIA measurements during a single
 563 flight on 9 March 2016. The dashed lines mark the lowest altitudes of MLS observations
 564 assimilated in M2-SCREAM. (c) GLORIA observations.

565
 566 The overall morphologies of the M2-SCREAM HNO₃, water vapor, and ozone profiles agree very
 567 well with the observations and are dynamically consistent with the flight trajectory in equivalent
 568 latitude space (Butchart and Remsberg, 1986) that ranges between 40°N and 80°N (**Fig. 6a**). A
 569 particularly interesting detail is the drop in the HNO₃ and ozone mixing ratios between 11 and 13.5
 570 km at the end of the flight, coincident with a sharp increase of the equivalent (but not geographical)
 571 latitude, consistent with the aircraft crossing the boundary between different air masses. This
 572 feature is seen in M2-SCREAM and (in much greater detail) in the aircraft data. M2-SCREAM
 573 underestimates HNO₃, which is qualitatively consistent with the behavior at high northern latitudes
 574 in **Fig. 5**. The ozone fields are qualitatively very similar between the reanalysis and the

575 observations, although the smallest scale features are absent in M2-SCREAM as expected. Similar
 576 conclusions are drawn from examining other flights (**Figs S3–S16**).

577

578 There is a distinct layer of minimum water vapor mixing ratio above the tropopause in M2-
 579 SCREAM that is not present in the GLORIA observations. This is a persistent feature in all the
 580 aircraft comparisons (**Figs 6 and S3–S16**). The occurrence of similar lowermost stratosphere
 581 minima is also frequent in the reanalysis at other latitudes and periods (not shown). Close
 582 examination of available FPH water vapor profiles from the Lauder and Boulder locations reveals
 583 a frequent occurrence of such deep minima located between about 2 and 4 km above the tropopause
 584 (**Movies M1 and M3** in Supplementary Information). These minima are also present in the station
 585 data but are less deep and less frequent than those in M2-SCREAM. One possible explanation is a
 586 low bias in MLS water vapor in a shallow layer above the tropopause. Such a bias was identified
 587 in version 3 MLS retrievals with respect to a multi-instrument mean by Hegglin et al. (2013) and
 588 with respect to HIRDLS data by Schwartz et al. (2015), and v4 retrievals can be expected to be
 589 similar in this regard.



590
 591 **Figure 7:** Statistical comparisons for 2005–2021 of the M2-SCREAM water vapor with NOAA's
 592 frost point hygrometer (FPH) measurements at Lauder (169.68°E, 45.04°S), Hilo (155.05°W,
 593 19.72°N), and Boulder (105.2°W, 39.95°N) in units of ppmv. (a) Mean profiles from FPH (black)
 594 and M2-SCREAM (red). (b) and (c) M2-SCREAM minus FPH statistics: mean (plus signs),
 595 standard deviations around the mean (short vertical bars), probability density functions (colors)
 596 as functions of tropopause-relative (TR) height. The dotted lines are the mean difference
 597 plus/minus standard deviation of the FPH observations. Note that the abscissa shows the natural
 598 logarithm of H₂O mixing ratio in ppmv. Vertical ranges of 5–15 km and 0–5 km are shown in (b)
 599 and (c), respectively. Note the different bin sizes used in (b) and (c).

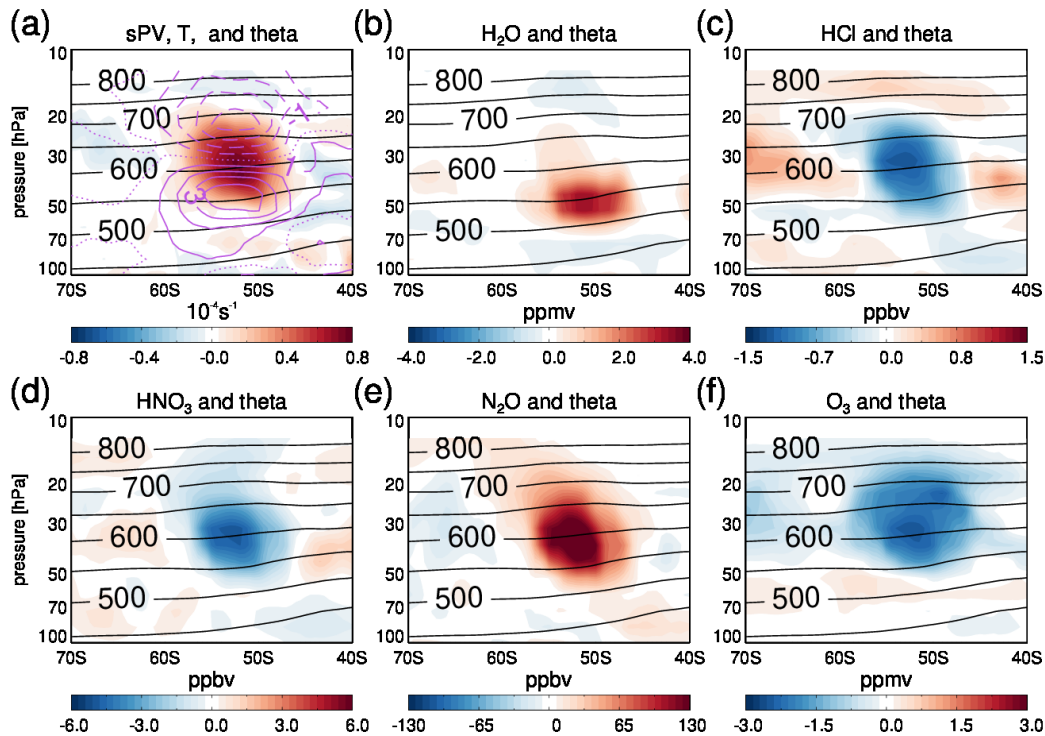
600

601 Comparisons of the reanalysis water vapor against the FPH data at these three locations are shown
 602 in **Fig. 7**. These figures are similar in design to **Fig. 3**. Here, however, the vertical coordinate is
 603 the distance from the tropopause (“tropopause-relative height”) defined as the 2 potential vorticity
 604 (PV) unit surface ($1 \text{ PVU}: 1.0 \times 10^{-6} \text{ m}^2 \text{ s}^{-1} \text{ K kg}^{-1}$) or the 380-K potential temperature surface,
 605 whichever is located at a lower altitude. The difference averages are calculated as M2-SCREAM
 606 minus FPH sonde observations. Additionally, the dotted lines in **Fig. 7(b,c)** do not represent
 607 uncertainties but rather the standard deviations of the observed FPH mixing ratios added and
 608 subtracted from the mean M2-SCREAM minus FPH difference. The agreement between the two
 609 data sets is very close between about 4 and 15 km above the tropopause. Below 4 km there is more
 610 spread in the differences but the standard deviations of the difference are generally smaller than
 611 the observed variability as the latter becomes very large near the tropopause. These standard
 612 deviations range between 17 ppmv at the tropopause (Lauder) and about 0.2 ppmv above 4 km at
 613 all three stations. Most of them are smaller than the standard deviations of the observed water
 614 vapor mixing ratio also above 4 km but often not by much as water vapor variability is very small
 615 in much of the lower and middle stratosphere except close to the tropopause. Correlations between
 616 M2-SCREAM and FPH (not shown) range between 0.55 and 0.9. The reanalysis exhibits a positive
 617 bias of up to 0.2 ppmv at altitudes higher than the 4 km above the tropopause, consistent with a
 618 MLS version 4.2 wet bias compared to the FPH record at these altitudes (e.g., Figure 1 of Livesey
 619 et al., 2021). The shapes of the average water vapor profiles are very similar in FPH data and in
 620 M2-SCREAM. The minimum is located between 3 and 4 km above the tropopause, indicative of
 621 the existence of a tropopause transition layer where moist tropospheric air mixes into the LS. This
 622 is consistent with the findings of Hegglin et al. (2009) who identified such a transition layer in the
 623 extratropics. Overall, the performance of M2-SCREAM water vapor measured against the FPH is
 624 extremely good. We combined the individual sonde profiles and collocated M2-SCREAM profiles
 625 into three short animations to facilitate convenient viewing. These animations are included in the
 626 Supplementary Information (**Movies S1–S3**). We encourage the reader to watch them as they help
 627 to qualitatively assess this agreement on a profile-by-profile basis. Those animations also show
 628 assimilation uncertainty envelopes around the assimilated profiles.

629 **6.2 Australian New Year’s busfires**

630 Severe bushfires in south-eastern Australia in December 2019 and January 2020 resulted in
 631 exceptionally strong pyro-cumulonimbus (“PyroCb”) outbreaks that injected plumes of smoke and
 632 tropospheric air into the LS (Allen et al., 2020; Kablick et al., 2020; Khaykin et al., 2020; Schwartz
 633 et al., 2020). Because of the presence of sunlight-absorbing smoke the largest plumes acted as
 634 synoptic-scale heat sources whose thermal expansion spawned localized regions of anticyclonic
 635 circulation (Allen et al., 2020). The air trapped in these anticyclones remained relatively isolated
 636 and retained signatures of tropospheric composition for up to several months. Using MLS data,
 637 Schwartz et al. (2020) tracked several large plumes as they traveled through the southern
 638 hemisphere (SH) stratosphere and identified that at least one of them circled the Earth three times
 639 before dispersing. The convective plumes associated with the Australian New Year’s (ANY) fires
 640 are not simulated in the GEOS model. The presence of the plume-induced anticyclones and their
 641 chemical composition in the reanalysis can, therefore, arise only from assimilation of radiance data
 642 in MERRA-2 and MLS constituent observations in CoDAS.

643



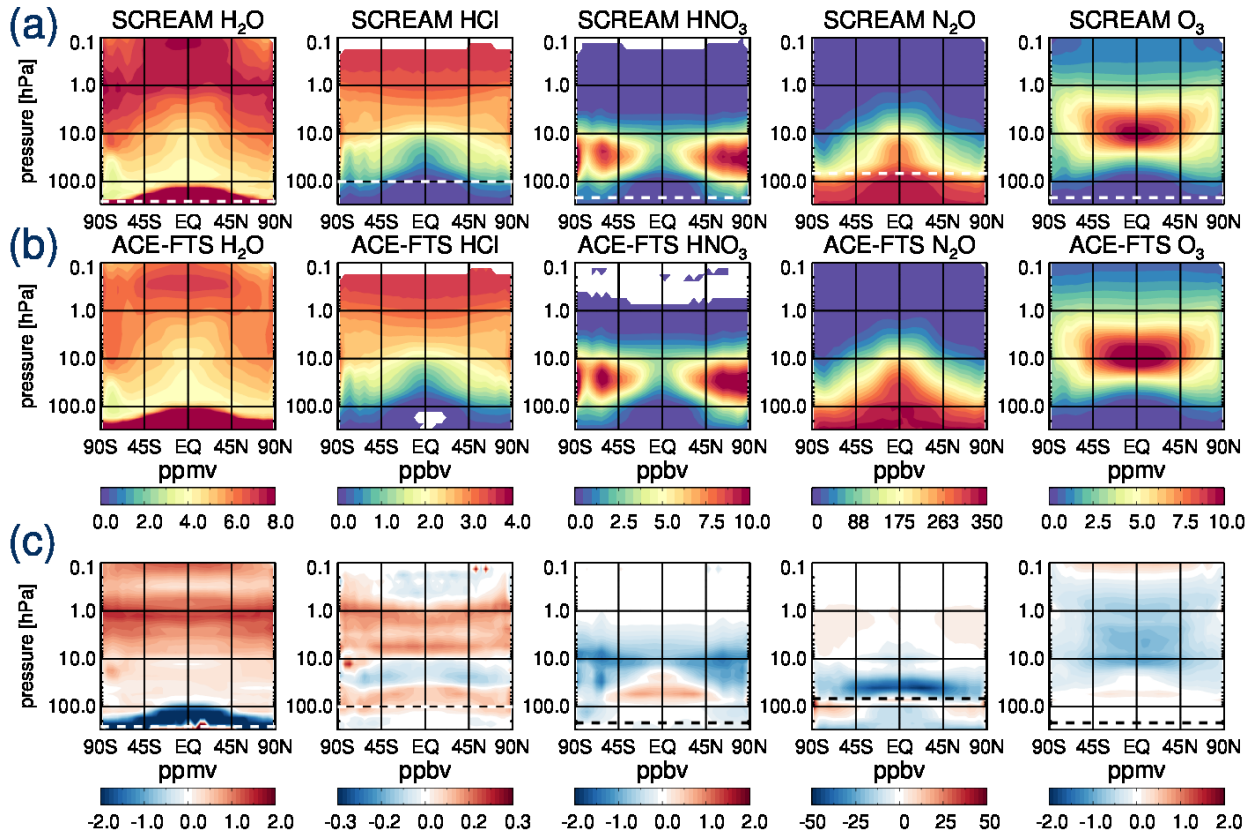
644 **Figure 8:** Departures from the zonal mean for sPV (shading) and temperature (magenta contours,
 645 1 K spacing) (a), water vapor (b), HCl (c), HNO₃ (d), N₂O (e), and ozone (f) at 80°W on 31
 646 January 2020. Also shown are potential temperature contours (50 K intervals).
 647

648
 649 **Figure 8** shows the departures from the zonal mean of scaled PV (sPV), temperature, and the five
 650 M2-SCREAM constituents near the center of the largest ANY plume at 80°W between 40°S and
 651 70°S on 31 January 2020. These plots are similar to Figures 1 and 2 in Allen et al. (2020). For
 652 display purposes we use sPV, defined as PV divided by a standard static stability value at each
 653 potential temperature (Dunkerton & Delisi, 1986; implementation as in Manney et al., 1994). This
 654 method was chosen rather than simply PV because the rapid increase of the absolute values of the
 655 latter with height tends to produce an apparent upward shift in the location of the dynamical
 656 anomaly with respect to the temperature anomaly dipole. The anticyclone is seen in **Fig. 8** as a
 657 positive sPV anomaly. The associated positive and negative temperature departures at the bottom
 658 and top of the plume, respectively, are consistent with the dynamical response to the presence of
 659 a localized heat source and were observed in previous studies (Allen et al., 2020; Khaykin et al.,
 660 2020). The positive anomalies in water vapor (up to about 3 ppmv) and N₂O (in excess of 130
 661 ppbv) and negative anomalies for HCl (over 1 ppbv), HNO₃ (up to 0.4 ppbv), and ozone (2 ppmv)
 662 indicate partly tropospheric air and, for HCl, chemically altered composition of the plume that
 663 extended between about 50 and 20 hPa at that time, in agreement with previous studies.
 664 Preliminary comparisons with individual MLS profiles (not shown) suggest that M2-SCREAM
 665 reproduces the position of the HCl, HNO₃, N₂O, and ozone departures from the zonal mean,
 666 although it tends to slightly underestimate the magnitudes of the first three. However, M2-
 667 SCREAM fails to capture the magnitude and vertical extent of the water vapor departures from the
 668 zonal mean. MLS observed water vapor mixing ratios as high as 18 to 20 ppmv at the center of the plume,
 669 several times larger than those seen in M2-SCREAM. The M2-SCREAM water vapor anomaly is limited
 670 to the bottom portion of the plume. A much larger maximum above is not present in the reanalysis.

671 An analysis of the assimilation statistics revealed that, in the absence of the plume in the GEOS
672 background state, the observations of the extremely large water vapor mixing ratios were rejected
673 by the CoDAS internal quality control. This initial analysis of the ANY plume in M2-SCREAM
674 demonstrates that the reanalysis is capable of reproducing most of its features realistically. It also
675 demonstrates the trade-off between simple assumptions meant to reduce noise in the assimilated
676 product (additional quality control) and the ability to capture short-lived anomalies. The failure to
677 reproduce the maximum water vapor anomalies warrants future improvements to the GEOS
678 assimilation system. A preliminary analysis of the LS water vapor enhancement following the
679 eruption of the Hunga Tonga volcano in mid-January 2022 (not shown) suggests that relaxing the
680 internal quality screening may be necessary to reproduce the observed constituent fields during
681 extreme anomalous events.

682 **6.3 Global comparisons**

683 In this subsection, we perform global comparisons of M2-SCREAM with independent
684 observations from ACE-FTS and SAGE III/ISS. **Figure 9** shows the zonal mean differences
685 between the five M2-SCREAM constituents and all available ACE-FTS data between 2005 and
686 2020. The reanalysis fields are sampled at ACE-FTS observation locations and within 1.5 hour of
687 observation times and both data sets are interpolated to the same pressure grid. The color scales
688 used in this figure are the same as those in the MLS comparisons to help the reader assess the
689 magnitude of the reanalysis differences with independent data compared to the differences with
690 assimilated observations. As expected, the former are significantly larger than the latter as the
691 reanalysis is tightly constrained to MLS. It follows that **Figs 4 and 9** reflect the relative biases
692 between the two data sources as well as points of agreement between them and potentially any
693 seasonal sampling bias from the ACE-FTS orbit.

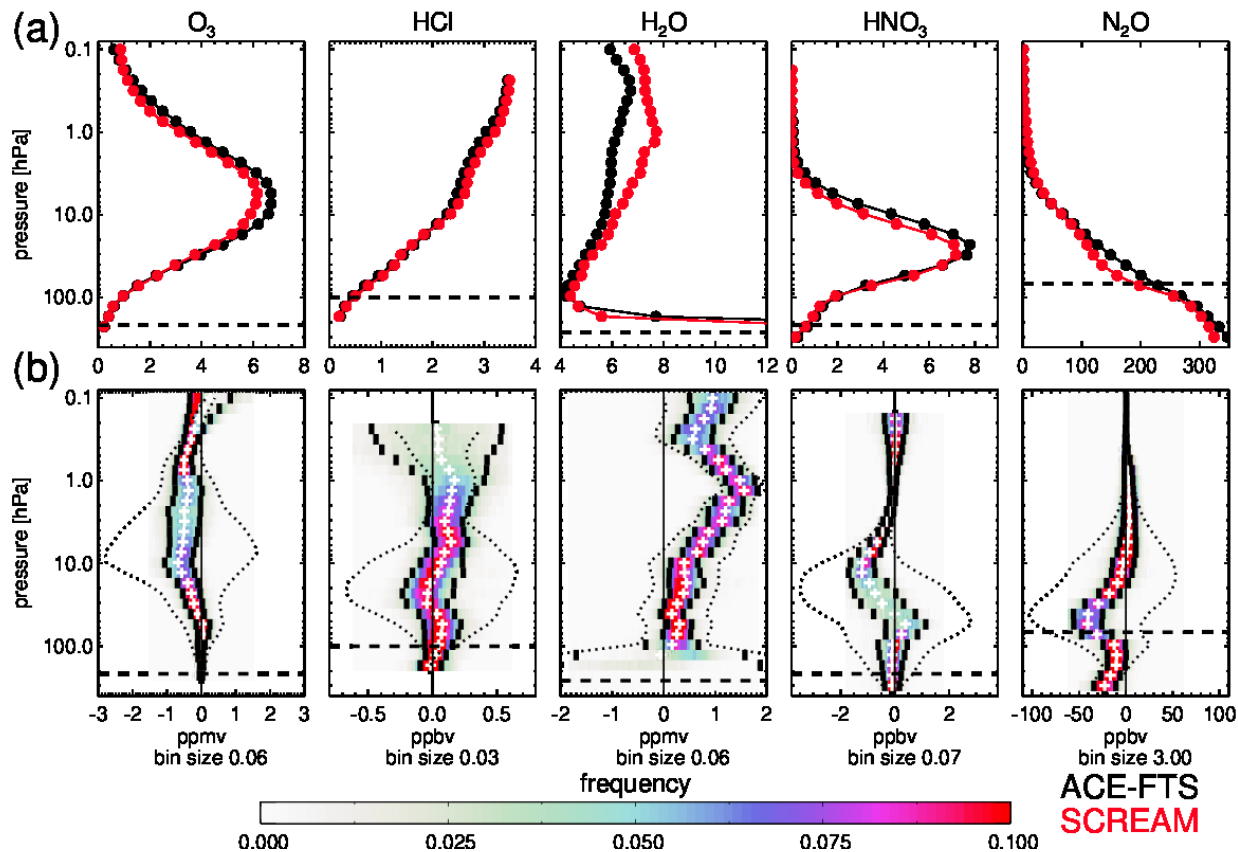


694
 695 **Figure 9:** Zonal mean mixing ratios of the assimilated constituents calculated from ACE-FTS
 696 data (a) and M2-SCREAM sampled at the ACE-FTS observation locations (b). The M2-SCREAM
 697 minus ACE-FTS differences are shown in (c). The dashed lines (white, (a); black, (c) except HCl
 698 where white is used) mark the lowest altitudes of MLS observations assimilated in M2-SCREAM.
 699 All quality-screened ACE-FTS data between 2005 and 2021 are used.

700

701 Even a cursory examination of **Fig. 9** (a) and (b) reveals overall very good agreement between the
 702 reanalysis and ACE-FTS in terms of the climatological structures in the five constituent fields,
 703 with the differences being small relative to the average mixing ratios. M2-SCREAM water vapor
 704 is higher than that from ACE-FTS, with the magnitude of the difference increasing with altitude
 705 and reaching almost 2 ppmv at the stratopause. This is qualitatively consistent with an overall wet
 706 bias in MLS version 4.2, but the magnitude of the differences is much larger than that between
 707 M2-SCREAM and MLS version 5 (Figure 5), FPHs (Figure 7), and SAGE III/ISS (**Fig. 11**). The
 708 HCl differences are within about 0.1 ppbv and exhibit an alternating layered pattern with little
 709 latitudinal variation. For HNO₃ we see a positive difference (M2-SCREAM greater than ACE-
 710 FTS) of up to 0.5 ppbv between 45°S and 45°N and below 10 hPa and larger negative differences
 711 in excess of 1 ppbv around 10 hPa. This pattern resembles that of the M2-SCREAM minus MLS
 712 differences, but its magnitude is larger. The largest N₂O differences (of about 40 ppbv) are seen
 713 between 40 and 50 hPa in the tropics and subtropics. As seen in **Figs 4** and **9**, tropical N₂O is
 714 approximately constant between 50 and 20 hPa, in agreement with MLS (see also **Fig. S2**). A close
 715 examination of MLS N₂O profiles in the tropics (not shown) confirms a near-zero vertical gradient
 716 in that region. As there is no known dynamical mechanism that would produce this feature, we
 717 suggest that it results from MLS retrieval errors. Finally, the M2-SCREAM ozone is up to 1 ppmv
 718 lower than that reported by ACE-FTS in most of the stratosphere and in the lower mesosphere.

719
720
721
722
723
724
725



726
727
728
729
730
731
732
733
734
735
736

Figure 10: Statistical comparisons of the M2-SCREAM ozone, HCl, water vapor, HNO₃, and N₂O with ACE-FTS observations for 2020. (a) mean profiles (M2-SCREAM in red and ACE-FTS in black). (b) difference statistics; specifically, difference mean (plus signs), standard deviations around the mean (short vertical bars), probability density functions (colors) at prescribed pressure levels. The dotted lines are the mean difference plus/minus standard deviation of the ACE-FTS observations. All available 2020 ACE-FTS data are used for ozone, HCl, and water vapor. Only data between 60°S and 60°N are used for HNO₃. The dashed lines mark the lowest altitudes of MLS observations assimilated in M2-SCREAM.

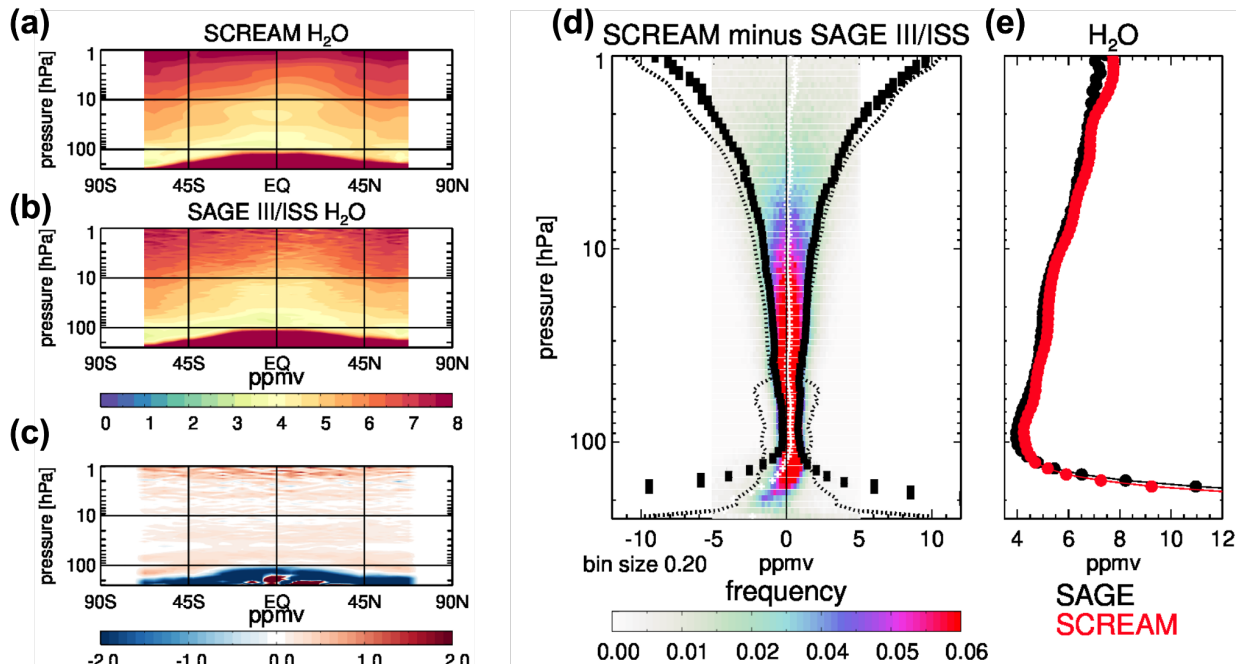
737 Globally aggregated statistics of M2-SCREAM minus ACE-FTS differences along with average
738 constituent profiles are shown in **Fig. 10** (results limited to the 30°N to 60°N for December 2005–
739 to January 2020 are shown in **Figs S17** and **S18** for direct comparison with the results of Errera et
740 al., 2019 for BRAM2). Since the global mean differences were discussed above (**Fig. 9**). Here we
741 focus on the difference pdfs and their standard deviations. As in **Fig. 7** the dotted lines show the
742 mean difference plus/minus the standard deviations of the observed mixing ratios. These standard

743 deviations provide a measure of constituent variability that includes seasonal and geographical
744 variations. For ozone (**Fig. 10**) the differences are approximately normally distributed in the
745 stratosphere. The difference standard deviations (short vertical bars) are within 0.5 ppmv, much
746 smaller than the ozone variability. Above the stratopause the difference pdfs are bimodal. This is
747 likely related to the bimodality of the ozone concentrations around twilight (the local time of ACE-
748 FTS observations). The M2-SCREAM minus ACE-FTS differences for HCl have standard
749 deviations of up to 0.25 ppbv in the stratosphere. The global mean HCl mixing ratios vary between
750 about 0.1 and 3 ppbv. The variability of the observed mixing ratios is typically much larger in the
751 middle stratosphere, reaching about 0.6 ppbv between 20 and 10 hPa. Above the stratopause, the
752 differences become larger than the variability of the observations. This is also where MLS
753 uncertainties increase with altitude (**Fig. S1b**). The most pronounced feature of the water vapor
754 comparisons in **Fig. 10** is the altitude dependent bias resulting from a relative difference between
755 MLS and ACE-FTS bias that was discussed above. The difference standard deviations are within
756 the climatological envelope of variability. It should be noted that both the M2-SCREAM minus
757 ACE-FTS differences and variability of the observations are relatively small compared to the
758 average stratospheric water vapor. For HNO₃ and N₂O the difference standard deviations are
759 considerably smaller than the observation standard deviations in the deep layers where each of
760 these species exhibits relatively large mixing ratios (for pressures greater than about 5 hPa for
761 HNO₃, and 20 hPa for N₂O).

762

763 Zonal mean and annual differences between M2-SCREAM and SAGE III/ISS profiles of water
764 vapor are shown in **Fig. 11**. Because of the significant noise in the SAGE III/ISS retrieval (see
765 section 4.2), we chose to show the instrument uncertainties (dotted lines in **Fig. 11d**) rather than
766 the standard deviation of the observed values, shown in **Fig. 10**. Throughout the stratosphere, M2-
767 SCREAM mixing ratios of water vapor are biased high with respect to SAGE III/ISS retrievals,
768 with the differences ranging from about 0.1 to 0.7 ppm. The largest differences, up to about 10%,
769 are seen in the upper stratosphere. SAGE III/ISS water vapor profiles were reported to have a
770 roughly 10% dry bias with respect to MLS version 4.2 (Davis et al., 2021) and close agreement
771 with MLS version 5.0 outside of tropospheric regions (Park et al., 2021). Among the data sets
772 analyzed here, MLS, ACE-FTS, and SAGE III/ISS the low water vapor concentrations reported
773 by ACE-FTS in the upper stratosphere and lower mesosphere emerge as an outlier.

774

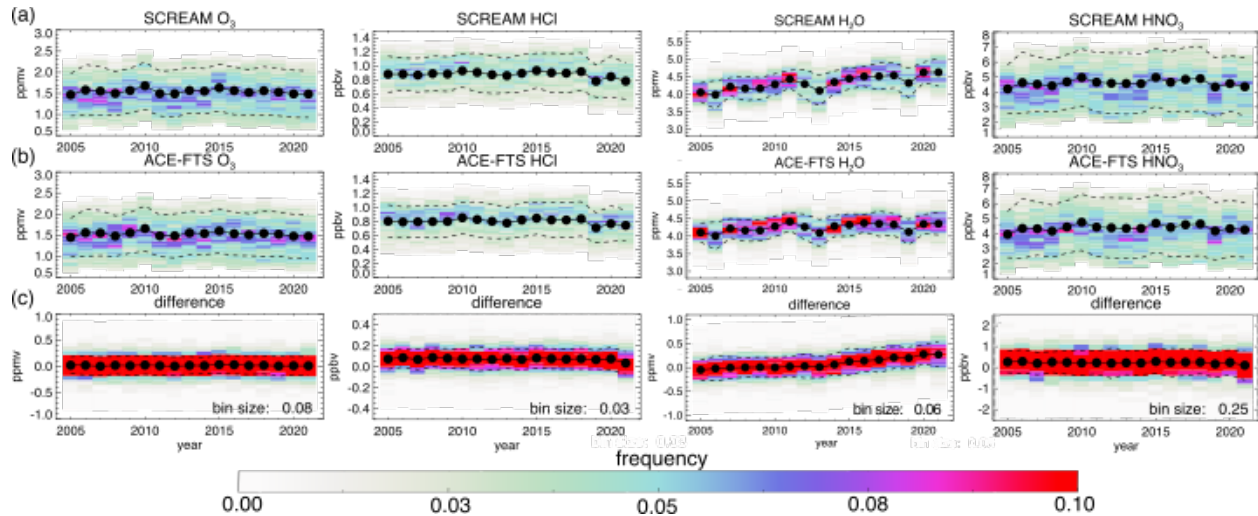


775
 776 **Figure 11:** Comparison of M2-SCREAM water vapor with SAGE III/ISS observations in 2018.
 777 Zonal mean annual water vapor from M2-SCREAM and SAGE III/ISS are shown in panels (a) and
 778 (b), respectively. Panel (c) shows the reanalysis minus SAGE III/ISS. Various global statistics are
 779 plotted in (d) and (e). Panel (d) plots the mean difference (plus signs), mean plus/minus difference
 780 standard deviation (short vertical bars), and pdfs of the difference (colors) in the left-hand side
 781 panel. The dashed lines are plus/minus estimated SAGE III/ISS uncertainties. Panel (e) displays
 782 the average profiles.

783 6.4 Long-term behavior and interannual variability

784 Since ACE-FTS is available for the entire MLS record, we use ACE-FTS observations to assess
 785 the performance of M2-SCREAM over the reanalysis period. Comparisons are done for ozone,
 786 HCl, water vapor and HNO₃ using annually aggregated data for 2005 to 2020 (70 hPa, 30°N–60°N,
 787 **Fig. 12**). We have decided not to evaluate the long-term performance of assimilated N₂O because
 788 of the known significant drift in the MLS retrievals of that constituent in the LS, even though this
 789 is where N₂O is of particular interest owing to its long lifetime. We do not recommend N₂O from
 790 M2-SCREAM for studies of long-term changes. We do however emphasize its utility for transport
 791 studies on shorter time scales (see **Section 6.5**). The figure shows pdfs (color), averages (black
 792 dots), standard deviations (dashed lines) of annually aggregated M2-SCREAM (top row) where,
 793 as always, M2-SCREAM is sampled at observation locations), ACE-FTS (middle row) and their
 794 differences M2-SCREAM minus ACE-FTS (bottom row).

795



796
 797 **Figure 12:** Time series of annual 70-hPa 30°N–60°N pdfs from M2-SCREAM subsampled at ACE-
 798 FTS observation locations (a) and from ACE-FTS data (b). Panel (c) shows the pdfs of M2-
 799 SCREAM minus ACE-FTS. Results are shown for (from left to right) ozone, HCl, H₂O, and HNO₃.
 800 The black filled circles are the annual averages, and the dashed lines mark the 1-sigma envelopes
 801 around the mean.

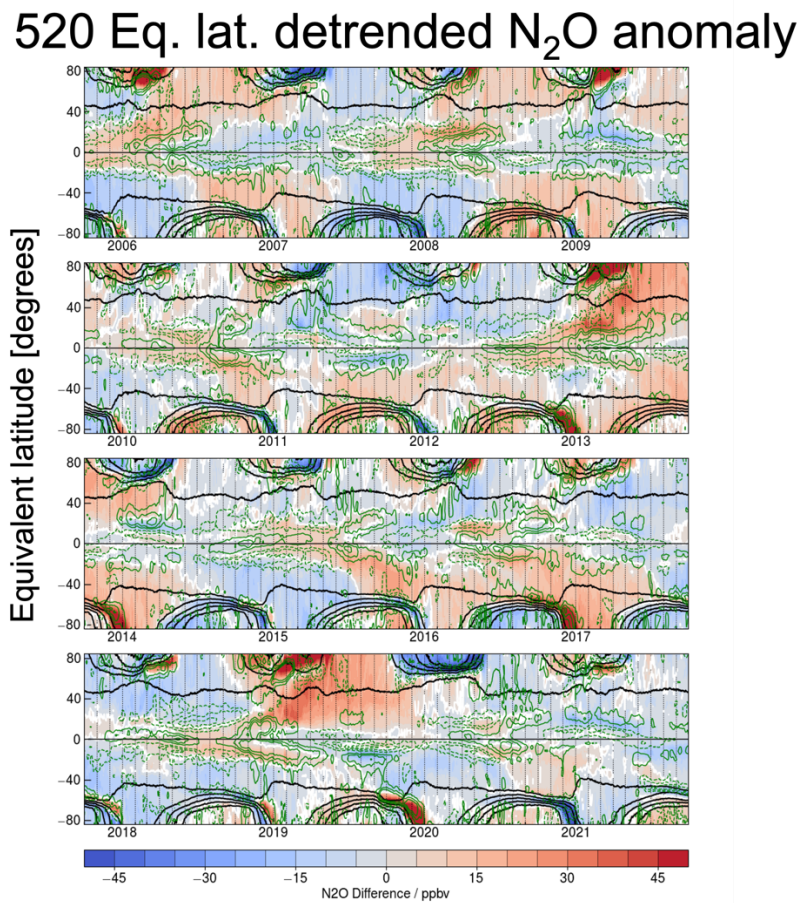
802
 803 The distributions of ozone and HCl vary considerably from year to year. There is a very good
 804 agreement between the structures of the histograms from ACE-FTS and M2-SCREAM (**Fig. 12**
 805 (a, b)), although the reanalysis HCl exhibits a slightly larger spread than that in ACE-FTS
 806 observations. The difference pdfs (**Fig. 12c**) use the same bin sizes as those used in the other panels
 807 to emphasize the relative magnitudes of the differences and the mixing ratios themselves. For both
 808 constituents, the reanalysis minus satellite differences are much smaller than the mixing ratio
 809 variability. The reanalysis HCl exhibits a positive bias of about 10 to 12% consistent with the
 810 results shown in **Fig. 9**. Linear fits to the differences (not shown) show no evidence of any relative
 811 drift between M2-SCREAM and ACE-FTS ozone and HCl.

812
 813 **Figure 12** also shows the results for water vapor and HNO₃. Here again, the details of the pdf
 814 shapes are well reproduced by M2-SCREAM. As seen in the ozone and HCl differences, the
 815 difference pdfs (panel (c)) are significantly more concentrated (indicative of little spread) and more
 816 symmetric around the mean than the mixing ratio distributions. The reanalysis HNO₃ shows a
 817 small positive bias of about 0.3 ppbv (compared to the mean mixing ratio of about 4 ppbv) as
 818 already seen in **Fig. 9**. There is no evidence of a drift between the M2-SCREAM and ACE-FTS
 819 HNO₃. Water vapor in the reanalysis exhibits a drift of approximately 0.2 ppmv per decade,
 820 consistent with the known drift in MLS version 4.2 water vapor.

821
 822 Overall, all four reanalysis constituents agree well with ACE-FTS in the extra-tropical LS in terms
 823 of interannual variability of the tracer mixing ratio distributions over the reanalysis period. Apart
 824 from water vapor (and N₂O, not shown) there is no evidence of time dependent biases between
 825 M2-SCREAM and ACE-FTS observations.

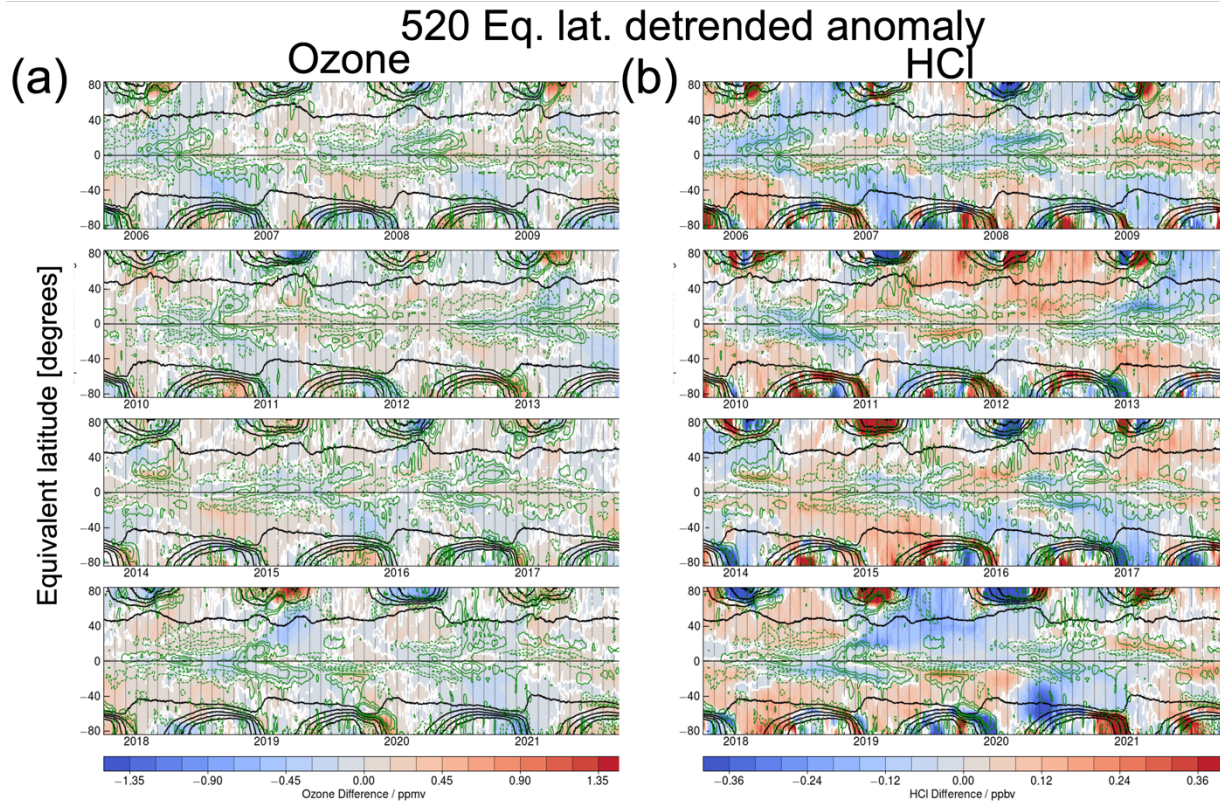
826 **6.5 Dynamically controlled interannual variability**

827 We now turn to the representation of dynamically controlled interannual variability of the five
 828 assimilated constituents. Time series of detrended anomalies of N₂O (**Fig. 13**), water vapor, HNO₃
 829 (**Fig. 14**), ozone, and HCl (**Fig. 15**) interpolated to the 520-K potential temperature surface
 830 (between about 40 and 70 hPa, the latter value being near the lowest level where N₂O is
 831 assimilated) shown as functions of equivalent latitude. The black lines in all three figures are
 832 selected PV contours, with all except the lowest value shown indicating the location of the polar
 833 vortex edge during fall-winter-spring. Also shown are effective diffusivity anomalies, k_{eff} (green)
 834 (Nakamura, 1996; Haynes and Shuckburgh, 2000a,b; Allen and Nakamura, 2001). The latter
 835 indicate regions of enhanced (solid) and suppressed (dashed) isentropic mixing. The anomalies are
 836 calculated by removing the monthly means calculated over the reanalysis period. For the trace gas
 837 fields, rather than subtracting the climatology, a linear fit to the daily time series over all the years
 838 is removed. Trace gas distributions on potential temperature surfaces are controlled by the effects
 839 of slow vertical diabatic transport and faster isentropic mixing by waves (Plumb, 2007; Shepherd,
 840 2007). These two processes typically act to sharpen and weaken the meridional tracer gradients,
 841 respectively. Because potential temperature, equivalent latitude and passive tracers are conserved
 842 in adiabatic and frictionless flows, any temporal variability of a constituent in the potential
 843 temperature / equivalent latitude space arises from non-conservative processes and/or chemistry.
 844 For further discussion of tracer analysis in potential temperature / equivalent latitude coordinates
 845 see Manney et al. (2005; 2009), Santee et al. (2011), and references therein.

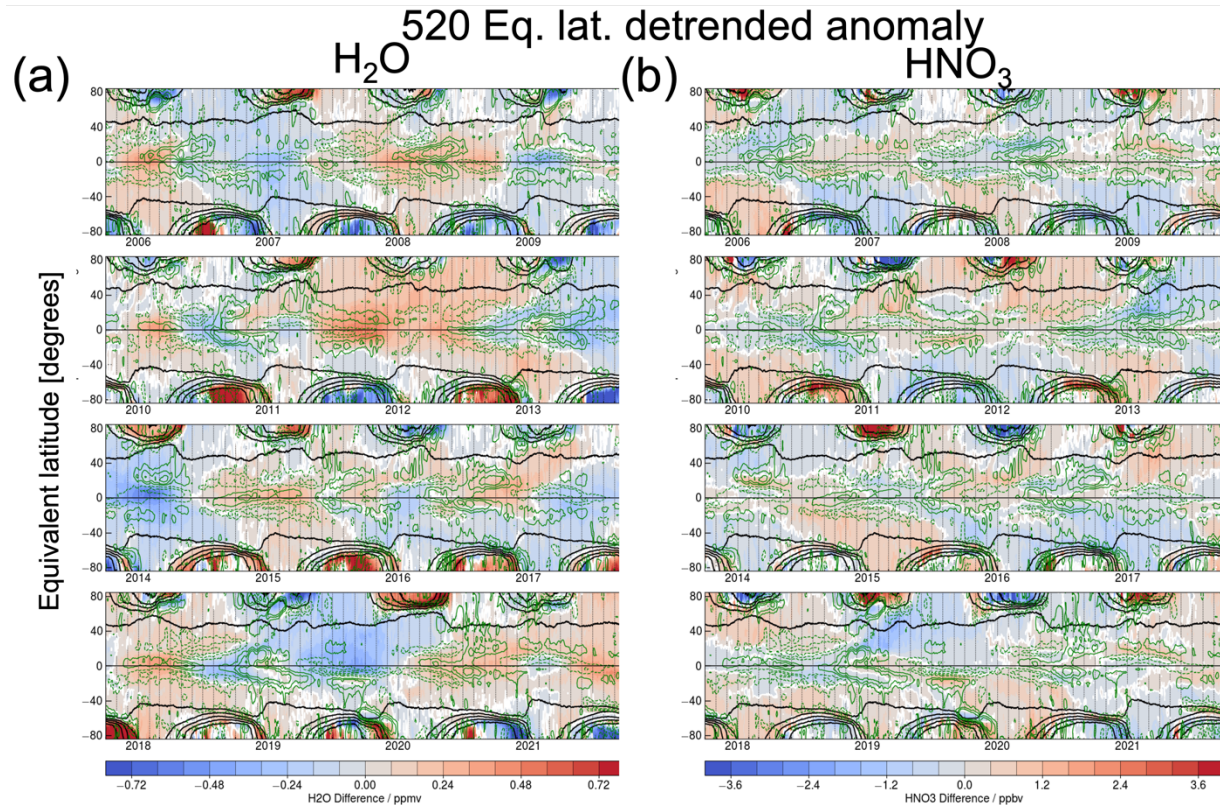


846

847 **Figure 13:** Equivalent latitude time series on the 520-K isentropic surface of M2-SCREAM N_2O
 848 detrended differences from the Aura mission climatology (time series is detrended by removing a
 849 linear fit over the mission to the values for each day of year). Black overlaid contours are sPV
 850 from 1.0 to $2.6 \times 10^{-4} s^{-1}$ by $0.4 \times 10^{-4} s^{-1}$, with the 1.4 contour representing the outer part of the
 851 vortex edge region. Green overlaid contours are anomalies from climatology in effective
 852 diffusivity expressed as log-normalized equivalent length (dashed negative contours indicate less
 853 mixing than in the climatology, solid contours more mixing than in the climatology).
 854
 855



856 **Figure 14:** As in Fig. 13 but for ozone (a) and HCl (b)
 857
 858



859
860 **Figure 15:** As in Fig. 13 but for water vapor (a) and HNO_3 (b)

861
862 As a chemically inactive gas in much of the stratosphere, N_2O is an excellent transport tracer. We
863 highlight some of the main features of the dynamical variability deducible from M2-SCREAM
864 N_2O on interannual scales (**Fig. 13**). The polar vortices that form in autumn and break up in spring
865 in each hemisphere are demarcated by a region of strong PV gradients and isolate the air within
866 them. In the absence of mixing, the slow descent of air within an undisturbed polar vortex leads to
867 depressed N_2O concentrations. In contrast, dynamical disturbances such as sudden stratospheric
868 warmings (SSWs) increase the vortex edge permeability (measured by k_{eff}), leading to higher
869 than average N_2O . Signatures of NH SSWs in 2006 (Manney et al., 2008, 2009a; Coy et al., 2009),
870 2009 (Manney et al., 2009b; Harada et al., 2010), 2013 (Coy and Pawson, 2015), 2018 and 2019
871 (Butler et al., 2020), and 2021, and a SH SSW in 2019 (Hendon et al., 2019; Wargan et al., 2020b;
872 Safieddine et al., 2020) are clearly discernible in **Fig. 13** in the PV contours and enhanced N_2O
873 mixing ratios around the vortex edge in these years. These events are associated with positive k_{eff}
874 anomalies. A signature of the early final warming in March 2016 (Manney and Lawrence, 2016)
875 is also seen as strongly positive N_2O and k_{eff} anomalies. In contrast, the very cold and strong NH
876 polar vortex in 2020 featured record low N_2O in the MLS period (Manney et al., 2020; Wohltmann
877 et al., 2020; 2021). Most of these events are well documented in the studies cited above and
878 references therein. In the tropics, a clear marker of the quasi-biennial oscillation (QBO) is seen in
879 the pattern of positive and negative N_2O anomalies alternating with a period of 26–28 months. The
880 520-K potential temperature surface is located near the bottom of the extratropical surf zone
881 (McIntyre and Palmer 1983), a region of strong wintertime wave activity and resulting mixing
882 flanked by the edge of the polar vortex and the subtropical mixing barrier on the poleward and
883 equatorward sides, respectively. We note that positive subtropical k_{eff} anomalies in some years

884 indicate a weakened transport barrier and are concurrent with enhanced N₂O transport into the
885 extratropics. The consistency of N₂O and k_{eff} variability seen in **Fig. 13** demonstrates the utility
886 of this M2-SCREAM data set for transport studies despite the biases and drifts discussed in
887 previous sections.

888

889 Unlike N₂O, variability of ozone, HCl, water vapor, and HNO₃ shown in **Figs 14** and **15** depends
890 not only on transport but also chemistry and, in the case of water vapor and HNO₃, also on the
891 thermodynamics of phase transitions. Low HCl and ozone anomalies in the exceptionally cold NH
892 winters of 2011, 2016, and 2020 indicate strong chlorine activation and ozone depletion consistent
893 with previous studies (Manney et al., 2011; Manney and Lawrence 2016; Manney et al., 2020;
894 Wohltmann et al., 2020). In the SH, strong dehydration (through condensation) correlates well
895 with strong ozone depletion because both are associated with below-average temperatures. The
896 situation in the NH HNO₃ is more complex because of extreme interannual variability and
897 temperatures that are commonly close to the thresholds for forming of HNO₃- and ice-containing
898 PSCs, and we do not analyze it here. We also do not discuss HNO₃ in the polar regions further
899 because of its low quality in M2-SCREAM (**Section 3**).

900

901 Outside of the polar regions the distribution of all five assimilated species at 520 K is determined
902 mainly by transport. The spatial patterns of the high and low anomalies at extrapolar latitudes are
903 remarkably similar among N₂O, ozone, HNO₃, and HCl. Note that since N₂O has sources at the
904 surface and the other three in the upper atmosphere, the signs of the anomalies are reversed
905 between N₂O and the other tracers. High correlations between long-lived constituents are expected
906 from theory (Plumb et al., 2007) and provide confidence in dynamical consistency of the M2-
907 SCREAM output. Some degree of correlation is also seen between the N₂O and water vapor
908 anomalies, but interannual variability of the latter outside the polar regions is primarily controlled
909 by the temperature variations at the tropical cold point tropopause (e.g., Randel and Park, 2019).
910 One notable exception to the dynamically induced correlation among the tracers is the strong
911 negative HCl anomaly in the SH in 2020, which lacks counterparts in HNO₃ and N₂O, suggesting
912 a chemical origin of the HCl anomaly. Santee et al. (2022) present strong evidence of chlorine
913 activation on smoke particles from the ANY event in early 2020 and show results similar to ours
914 using MLS version 5 data (their Figure 1, see also Rieger et al., 2021). Overall, the features seen
915 in **Figs 13-15** closely track those in analogous plots constructed from MLS data at this and other
916 isentropic levels (not shown).

917

918 **7 Recommended usage**

919 As noted in **Section 2**, data assimilation is by construction driven by observations. There are at
920 least three types of situations in which the reanalysis output is not sufficiently informed by
921 observations. First, there were several MLS data outages long enough to compromise the
922 assimilation results. These are listed in **Table 2**. We recommend caution when using the reanalysis
923 over those periods. Second, due to short chemical time scales of upper-stratospheric ozone the
924 information content from MLS data cannot be assumed to fully propagate forward during six-
925 hourly model integrations (see **Section 5**). The M2-SCREAM ozone fields at pressures lower than
926 10 hPa (the upper stratosphere) should be treated with caution. Third, M2-SCREAM does not
927 assimilate HNO₃ at locations where condensed nitric acid is present in the model. Due to model
928 deficiencies, significant low bias exists in those regions. This affects HNO₃ in the polar LS during

929 winter and spring in both hemispheres. Thus, we do not recommend using the M2-SCREAM
 930 HNO₃ in those regions and seasons. The model's condensed HNO₃ is provided in the M2-
 931 SCREAM output files. While it is not recommended for scientific use it does provide information
 932 indicating the areas where gas-phase HNO₃ is not assimilated.

933
 934

Table 2 MLS Outages. MLS outages 5 days and longer

From	To	Remarks
30 March 2006	4 April 2006	
13 July 2007	8 August 2007	HCl only
27 March 2011	19 April 2011	
19 February 2012	24 February 2012	
15 March 2012	21 March 2012	
4 June 2018	11 June 2018	
21 June 2018	26 June 2018	
10 July 2018	19 July 2018	
27 January 2019	31 January 2019	

935

936 **8 Summary**

937 This study describes and evaluates M2-SCREAM, a new reanalysis of stratospheric ozone, water
 938 vapor, HCl, HNO₃, and N₂O from assimilation of MLS constituent profiles and OMI total ozone
 939 with the GEOS CoDAS system developed at NASA's GMAO. The reanalysis covers almost the
 940 entire MLS mission from September 2004 through February 2022 (at time of writing) and is made
 941 freely available to the scientific community. We argue that the reanalysis, as produced using data
 942 assimilation, is fundamentally an observation-driven product. That is, the information content of
 943 the available species is derived exclusively from the data where observations are assimilated. This
 944 is supported by the excellent agreement between the M2-SCREAM constituent fields and the
 945 assimilated MLS data, as well as by an analysis of the O-F and O-A residuals presented in **Section**
 946 **5**. We provide several examples that show that the reanalysis faithfully captures small-scale
 947 structures in the constituent fields in the LS as compared with aircraft data from the PGS campaign
 948 and balloon-borne frost point hygrometers at Boulder, CO and Hilo, HI, USA, and Lauder, NZ.
 949 We also show that the composition of one of the plumes from PyroCb events associated with
 950 Australian New Year's bushfires is in good qualitative agreement with other studies, though the
 951 maximum moisture of the plume is underestimated in M2-SCREAM because many of the MLS
 952 observations of high water vapor concentrations were rejected by the CoDAS quality control. The
 953 reanalysis agrees well with ACE-FTS and SAGE III/ISS observations. The M2-SCREAM-satellite

954 differences are near-normally distributed with standard deviations smaller than those of the ACE-
 955 FTS data. Relative biases between the reanalysis and ACE-FTS reflect systematic differences
 956 between MLS and ACE-FTS. Comparisons with independent satellite data as well as a process-
 957 based analysis of the consistency of the assimilated constituent fields with the MERRA-2
 958 dynamics and with large-scale processes documented in the literature demonstrate the utility of
 959 M2-SCREAM for scientific studies of chemical and transport variability on time scales ranging
 960 from hours to decades.

961
 962 M2-SCREAM agrees well with the Belgian reanalysis BRAM2 that also assimilates MLS data.
 963 There are, however, several differences between the two reanalyses that, as we hope, make them
 964 complement each other from the standpoint of the user. BRAM2 assimilates several more species
 965 than M2-SCREAM does and its HNO₃ product is of higher quality in the polar regions. Some
 966 advantages of M2-SCREAM are a longer period covered by this reanalysis and higher horizontal
 967 resolution of the assimilated fields. In addition, along with the assimilated fields we provide
 968 estimates of the reanalysis uncertainties and data quality flags designed to guide the scientific use
 969 of this new reanalysis. We note that the latest release of BRAM2 includes standard deviations of
 970 the ensemble means of the assimilated species (Q. Errera, personal communication, 2022).

971
 972 Several issues identified during the preparation, production and evaluation of M2-SCREAM will
 973 guide future work on chemical reanalyses at NASA's GMAO. Future work will include the
 974 development of a PSC scheme that will be fully compatible with assimilation of HNO₃, strategies
 975 for assimilating short-lived constituents (including upper-stratospheric and mesospheric ozone),
 976 and elimination of drifts in multidecadal data sets. A significant step of achieving the last goal will
 977 be assimilation of version 5 of MLS retrievals in the next composition reanalysis.

978 **Appendix A. Calculation of analysis uncertainties**

979 It is assumed that the analysis state x^a is normally distributed and unbiased with an uncertainty
 980 covariance matrix A . Similarly, the background state x^b is assumed unbiased with an uncertainty
 981 covariance matrix B . Under these assumptions, Desroziers et al. (2005) derived the following
 982 expressions for A and B (their equations (2) and (4)).

$$983$$

$$984 \quad E(H[x^a - x^b][y - Hx^b]^T) = HBH^T$$

$$985 \quad E(H[x^a - x^b][y - Hx^a]^T) = HAH^T.$$

986
 987 Here E and T denotes average and transpose, respectively, and H is the (linear) observation
 988 operator. We use these formulas to estimate the background and analysis variances (the diagonal
 989 elements of A and B), $Var^b = \frac{N+1}{N}(\sigma^b)^2$ and $Var^a = \frac{N+1}{N}(\sigma^a)^2$ from the reanalysis' internal
 990 statistics (see equations (2) and (4) in Desroziers et al. (2005)). Here, N denotes the number of
 991 observations and σ^a and σ^b are the diagonal elements of HAH^T and HBH^T , respectively. The
 992 calculations are done using O-F, O-A and A-F residuals aggregated within 10°×10°
 993 longitude/latitude bins on the MLS pressure levels for each month of the reanalysis separately.
 994 Very rarely (a few percent of cases) this procedure produces negative variance estimates. In those
 995 cases, we set Var^b to $(\alpha E(x^b))^2$, where α is the proportionally coefficient for background
 996 uncertainties (**Table 1**, $\alpha=0.1$ for N₂O), and we redefine $Var^a = MAX + \frac{N}{N+C}(MIN - MAX)$

997 with, $MAX = Var^b$, $MIN=0.25MAX$, and $C=300$. Additionally, if the analysis uncertainty
 998 variance estimate at any point is greater than the background uncertainty estimate, then we set the
 999 former to the latter. These choices represent our attempt to provide reasonable estimates in the rare
 1000 cases where the Desroziers' procedure fails. The analysis and background variances are
 1001 interpolated to the geolocation-dependent average model levels, mapped onto the horizontal grid
 1002 of the reanalysis, and converted to standard deviations. Because the reanalysis output is obtained
 1003 from analysis increments through IAU (**Section 3**) it is a linear combination of the background
 1004 and analysis states. While the uncertainties of the two are, in principle, correlated, the conservative
 1005 choice that we make here is to neglect the correlations and calculate the uncertainty of the
 1006 assimilated output as

$$1007 \quad \tau^a = \sqrt{\frac{1}{2}[(\sigma^b)^2 + (\sigma^a)^2]}.$$

1008 This quantity is provided in monthly NetCDF files alongside the reanalysis output. Also provided
 1009 are additional uncertainties associated with the bug fix as described in **Appendix B**. We emphasize
 1010 that τ^a is an estimate of the standard deviation of the reanalysis constituents' uncertainty
 1011 conditioned on the assimilated data and derived under assumption of optimality. It, therefore,
 1012 measures the CoDAS's "confidence" in the assimilation results given the prior (background)
 1013 uncertainty distribution and the usual assumptions of zero bias and Gaussianity. It tends to be small
 1014 compared to the constituents' mixing ratios. **Movies M1–M3** show M2-SCREAM water vapor
 1015 profiles along with error bars obtained by combining τ^a with the additional error estimate from
 1016 **Appendix B**.

1017 **Appendix B. Vertical shift correction**

1018 A coding error, identified after the reanalysis was completed for the period 2004 – April 2020,
 1019 resulted in an upward shift of the assimilated water vapor, HCl, HNO₃ and N₂O fields by half the
 1020 model layer, or approximately 0.5 km. Formally, this error can be described as an erroneous
 1021 application of a vertical shift operator, $(Sx^b)_i = x_{i+1/2}$ to the background constituent profile
 1022 $x^b = (x_1, x_2, \dots, x_k)^T$ prior to analysis. The analysis state is given by $x^a = x^b + K(y - Sx^b)$,
 1023 where y denotes observations, and $K = BS^T(SBS^T + R)^{-1}$ is the gain matrix. Here, B and R
 1024 denote the background and observation uncertainty covariance matrices, respectively. Assuming
 1025 that the analyses are sufficiently frequent, and the dynamics at any given level are sufficiently like
 1026 those $\frac{1}{2}$ grid point away from that level, that these analyses eventually drive the subsequent
 1027 forecasts so much toward the observations that $x^b = S^T x^t + \varepsilon^b$, where the mean $E[(\varepsilon^b)(\varepsilon^b)^T] =$
 1028 B and x^t is the true state, it can be shown that the application of the correction Sx^a to x^a results
 1029 in the optimal analysis state, i.e. the state one would obtain if the coding error were absent and the
 1030 background uncertainty were given by $E[(S\varepsilon^b)(S\varepsilon^b)^T] = SBS^T$. We applied the correction above
 1031 to the reanalysis output and tested it against a three-month long assimilation with a system where
 1032 the initial error was eliminated ("correct analysis"). The relative bias between the corrected and
 1033 the correct analyses is negligible. The difference standard deviations between the two runs result
 1034 from interpolation errors and small departures from the assumptions given above and represent an
 1035 additional uncertainty in the assimilated M2-SCREAM water vapor, HCl, HNO₃, and N₂O fields.
 1036 We determined that these uncertainties are of similar magnitude to the assimilation uncertainties
 1037 discussed in **Appendix A**. Therefore the recommended way to estimate the combined assimilation
 1038 and additional uncertainties is to multiply the former by $\sqrt{2}$.

1039 **Appendix C. output provided to the users**

1040 The main reanalysis product is provided in the form of NetCDF files valid at 0, 3, 6, 9, 12, 15, 18,
 1041 21 UTC and contains instantaneous assimilated fields at a 0.625° longitude \times 0.5° latitude horizontal
 1042 resolution on 72 GEOS model layers. The layer center pressures and layer pressure thickness are
 1043 also provided. Water vapor, HCl, HNO₃ and N₂O mixing ratios are given in mol/mol and ozone is
 1044 provided in ppmv. In addition to the five assimilated constituents the output files also contain
 1045 temperature, winds, cloud fraction, and PV from the GCM replay (in very close agreement with
 1046 MERRA-2) and the following non-assimilated constituents: ClO, CO, and condensed nitric acid.
 1047 These are not evaluated in this study and are provided for reference only. Neither are the
 1048 tropospheric concentrations evaluated and not advised to use.

1049
 1050 The assimilation uncertainties are given in monthly NetCDF files. The uncertainties are mapped
 1051 onto the full latitude-longitude grid as that of the reanalysis output. Nominal three-dimensional
 1052 pressure grid is also provided. Fill values indicate regions where no profile data are assimilated.
 1053 In addition to the assimilation uncertainties (**Appendix A**), the uncertainty files for months prior
 1054 to May 2021 also contain estimated additional uncertainties arising from the coding error and
 1055 correction (**Appendix B**). These are calculated from the reanalysis and an additional assimilation
 1056 experiment valid for March 2020. These fields are identical in all the uncertainty files. All
 1057 uncertainties are provided as one-sigma.

1058 **Acknowledgments**

1059 KW, BW, GLM, and SEC acknowledge support for this research by NASA's Modeling, Analysis
 1060 and Prediction (MAP) grant "A new look at stratospheric chemistry with multispecies chemical
 1061 data assimilation". KEK and PAW acknowledge support by the NASA SAGE III/ISS Science
 1062 Team grant 80NSSC21K1197. Work at the Jet Propulsion Laboratory, California Institute of
 1063 Technology, was done under contract with NASA. Resources supporting this work were provided
 1064 by the NASA High-End Computing (HEC) Program through the NASA Center for Climate
 1065 Simulation at Goddard Space Flight Center (GSFC). MERRA-2 is an official product of the Global
 1066 Modeling and Assimilation Office at NASA GSFC, also supported by MAP. We thank the MLS
 1067 team, especially Brian Knosp and Ryan Fuller, for data management and analysis support at JPL.
 1068 We thank Dr. Dale Hurst and Dr. Sören Johansson for their help with FPH and GLORIA data, and
 1069 Dr. Kaley Walker for detailed information on the use of ACE-FTS observations.

1071 **Open Research**

1072 M2-SCREAM (GMAO 2022a; 2022b) is available through the Goddard Earth Sciences Data and
 1073 Information Services Center (<https://disc.gsfc.nasa.gov>) and can be accessed via these links:
 1074 <https://doi.org/10.5067/7PR3XRD6Q3NQ> (assimilated fields) and
 1075 <https://doi.org/10.5067/7XRIJO9OP8PE> (analysis uncertainties). ACE-FTS is the primary
 1076 instrument on the SCISAT satellite, a Canadian-led mission mainly supported by the Canadian
 1077 Space Agency. ACE-FTS data were downloaded from <http://www.ace.uwaterloo.ca/data.php>.
 1078 SAGE-III/ISS data were downloaded from the NASA Atmospheric Science and Data Center
 1079 (ASDC; <https://eosweb.larc.nasa.gov/project/SAGE%20III-ISS>). FPH observations were obtained
 1080 from <ftp://ftp.cmdl.noaa.gov/ozwv/WaterVapor/>. GLORIA data are available at
 1081 <https://publikationen.bibliothek.kit.edu/1000086506>.

1082 **References**

- 1083 Allen, D. R., and N. Nakamura (2001), A seasonal climatology of effective diffusivity in the stratosphere, *J.*
1084 *Geophys. Res.*, 106, 7917–7935
- 1085 Allen, D.R., Fromm, M.D., Kablick III, G.P., and Nedoluha, G.E. (2020), Smoke With Induced Rotation and
1086 Lofting (SWIRL) in the stratosphere, *J. Atmos. Sci.*, 77, doi:10.1175/JAS-D-20-0131.1
- 1087 Bergthórsson, P., Döös, B. R. (1955), Numerical weather map analysis. *Tellus* 7, 329–340
- 1088 Bernath, P. F., McElroy, C. T., Abrams, M. C., Boone, C. D., Butler, M., Camy-Peyret, et al. (2005), Atmospheric
1089 Chemistry Experiment (ACE): Mission overview, *Geophys. Res. Lett.*, 32, L15S01,
1090 <https://doi.org/10.1029/2005GL022386>
- 1091 Bernath, P.F. (2017), The Atmospheric Chemistry Experiment (ACE), *Journal of Quantitative Spectroscopy and*
1092 *Radiative Transfer*, Volume 186 Pages 3-16, ISSN 0022-4073, <https://doi.org/10.1016/j.jqsrt.2016.04.006>
- 1093 Bloom, S., Takacs, L., DaSilva, A., & Ledvina, D. (1996), Data assimilation using incremental analysis updates.
1094 *Mon. Wea. Rev.*, 124, 1256–1271
- 1095 Boone, C.D., Bernath, P.F., Cok, D., Jones, S.C., and Steffen, J. (2020), Version 4 retrievals for the atmospheric
1096 chemistry experiment Fourier transform spectrometer (ACE-FTS) and imagers, *Journal of Quantitative*
1097 *Spectroscopy and Radiative Transfer*, Volume 247, 106939, ISSN 0022-4073,
1098 <https://doi.org/10.1016/j.jqsrt.2020.106939>
- 1099 Brasseur, G. P., and S. Solomon (2005), *Aeronomy of the Middle Atmosphere*, 3rd ed., Springer, New York
- 1100 Burkholder, J. B. , Sander, S. P. , Abbatt, J. Barker, J. R., Huie, R. E. Kolb, C. E., Kurylo, M. J., Orkin, V. L.,
1101 Wilmouth, D. M. and Wine, P. H. (2015), *Chemical Kinetics and Photochemical Data for Use in Atmospheric*
1102 *Studies*, Evaluation No. 18. JPL Publication 15-10, Jet Propulsion Laboratory, Pasadena, 2015
1103 <http://jpldataeval.jpl.nasa.gov>
- 1104 Butchart, N. and Remsberg, E.E. (1986), The area of the stratospheric polar vortex as a diagnostic for tracer
1105 transport on an isentropic surface, *J. Atmos. Sci.*, 43, 1319–1339
- 1106 Butler, AH, Lawrence, ZD, Lee, SH, Lillo, SP, Long, CS (2020), Differences between the 2018 and 2019
1107 stratospheric polar vortex split events. *Q J R Meteorol Soc.*; 146: 3503– 3521. <https://doi.org/10.1002/qj.3858>
- 1108 Cohn, S. E. (1997), An introduction to estimation theory. *J. Meteor. Soc. Japan*, 75, 257–288
- 1109 Considine, D. B., Douglass, A. R., Connell, P. S., Kinnison, D. E. and Rotman, D. A. (2000), A polar stratospheric
1110 cloud parameterization for the global modeling initiative three-dimensional model and its response to
1111 stratospheric aircraft, *J. Geophys. Res.*, 105(D3), 3955–3974
- 1112 Coy, L., Eckermann, S., and Hoppel, K. (2009), Planetary wave breaking and tropospheric forcing as seen in the
1113 stratospheric sudden warming of 2006, *J. Atmos. Sci.*, 66, 495–507
- 1114 Coy, L., and Pawson, S. (2015), The Major Stratospheric Sudden Warming of January 2013: Analyses and Forecasts
1115 in the GEOS-5 Data Assimilation System, *Monthly Weather Review*, 143(2), 491-510
- 1116 Davis, S. M., Hegglin, M. I., Fujiwara, M., Dragani, R., Harada, Y., Kobayashi, C. et al. (2017), Assessment of
1117 upper tropospheric and stratospheric water vapor and ozone in reanalyses as part of S-RIP., *Atmos. Chem.*
1118 *Phys.*, 17, 12743-12778, <https://doi.org/10.5194/acp-17-12743-2017>
- 1119 Desroziers, G., Berre, L., Chapnik, B. and Poli, P. (2005), Diagnosis of observation, background and analysis-error
1120 statistics in observation space. *Q.J.R. Meteorol. Soc.*, 131: 3385-3396. <https://doi.org/10.1256/qj.05.108>
- 1121 Dunkerton, T. J., & Delisi, D. P. (1986), Evolution of potential vorticity in the winter stratosphere of January-
1122 February 1979. *Journal of Geophysical Research*, 91(D1), 1199–1208.
1123 <https://doi.org/10.1029/JD091iD01p01199>
- 1124 Errera, Q., Chabrillat, S., Christophe, Y., Deboscher, J., Hubert, D., Lahoz, W., Santee, M. L., Shiotani, M.,
1125 Skachko, S., von Clarmann, T., and Walker, K. (2019), Technical note: Reanalysis of Aura MLS chemical
1126 observations, *Atmos. Chem. Phys.*, 19, 13647–13679, <https://doi.org/10.5194/acp-19-13647-2019>
- 1127 Friedl-Vallon, F., Gulde, T., Hase, F., Kleinert, A., Kulesa, T., Maucher, G., Neubert, T., Olschewski, F., Piesch,
1128 C., Preusse, P., Rongen, H., Sartorius, C., Schneider, H., Schönfeld, A., Tan, V., Bayer, N., Blank, J., Dapp, R.,
1129 Ebersoldt, A., Fischer, H., Graf, F., Guggenmoser, T., Höpfner, M., Kaufmann, M., Kretschmer, E., Latzko, T.,
1130 Nordmeyer, H., Oelhaf, H., Orphal, J., Riese, M., Schardt, G., Schillings, J., Sha, M. K., Suminska-Ebersoldt,
1131 O., and Ungermann, J. (2014), Instrument concept of the imaging Fourier transform spectrometer GLORIA,
1132 *Atmos. Meas. Tech.*, 7, 3565–3577, <https://doi.org/10.5194/amt-7-3565-2014>
- 1133 Flemming, J., Benedetti, A., Inness, A., Engelen, R. J., Jones, L., Huijnen, V., Remy, S., Parrington, M., Suttie, M.,
1134 Bozzo, A., Peuch, V.-H., Akritidis, D., and Katragkou, E. (2017), The CAMS interim Reanalysis of Carbon

- 1135 Monoxide, Ozone and Aerosol for 2003–2015, *Atmos. Chem. Phys.*, 17, 1945–
 1136 1983, <https://doi.org/10.5194/acp-17-1945-2017>
- 1137 Gelaro, R., McCarty, W., Suárez, M.J., Todling, R., Molod, A., Takacs, L. et al., (2017), The Modern-Era
 1138 Retrospective Analysis for Research and Applications, Version 2 (MERRA-2). *J. Climate*, 30, 5419–5454,
 1139 <https://doi.org/10.1175/JCLI-D-16-0758.1>
- 1140 Gilpin, S., Matsuo, T., and Cohn, S.E. (2022), Continuum covariance propagation for understanding variance loss in
 1141 Advective systems. *SIAM/ASA J. on Uncertainty Quantification*, 10:3, 886–914,
 1142 <https://doi.org/10.1137/21M1442449>
- 1143 Global Modeling and Assimilation Office (GMAO)(2015), MERRA-2 inst3_3d_asm_Nv: 3d,3-
 1144 Hourly,Instantaneous,Model-Level,Assimilation,Assimilated Meteorological Fields V5.12.4, Greenbelt, MD,
 1145 USA, Goddard Earth Sciences Data and Information Services Center (GES DISC), Accessed: **January 2021**,
 1146 10.5067/WWQSXQ8IVFW8
- 1147 Global Modeling and Assimilation Office (GMAO) (2022), M2-SCREAM: 3d,3-Hourly,Instantaneous,Model-
 1148 Level,Assimilation,Assimilated Constituent Fields,Replayed MERRA-2 Meteorological Fields, Greenbelt, MD,
 1149 USA, Goddard Earth Sciences Data and Information Services Center (GES DISC), Accessed: July
 1150 2022, doi:10.5067/7PR3XRD6Q3NQ
- 1151 Global Modeling and Assimilation Office (GMAO) (2022), M2-SCREAM: Monthly,Model-Level,Assimilated
 1152 Constituent Fields uncertainties, Greenbelt, MD, USA, Goddard Earth Sciences Data and Information Services
 1153 Center (GES DISC), Accessed: July, 2022. Doi:10.5067/7XRIJO9OP8PE
- 1154 Harada, Y., Goto, A., Hasegawa, H., Fujikawa, N., Naoe, H., & Hirooka, T. (2010), A Major Stratospheric Sudden
 1155 Warming Event in January 2009, *Journal of the Atmospheric Sciences*, 67(6), 2052–2069
- 1156 Haynes, P. and Shuckburgh, E. (2000a), Effective diffusivity as a diagnostic of atmospheric transport 1.
 1157 Stratosphere, *J. Geophys. Res.*, 105, 22777–22794
- 1158 Haynes, P., and Shuckburgh, E. (2000b), Effective diffusivity as a diagnostic of atmospheric transport: 2.
 1159 Troposphere and lower stratosphere, *J. Geophys. Res.*, 105, 22,795–22,810
- 1160 Hegglin, M. I., Boone, C. D., Manney, G. L., and Walker, K. A. (2009), A global view of the extratropical
 1161 tropopause transition layer from Atmospheric Chemistry Experiment Fourier Transform Spectrometer O3,
 1162 H₂O, and CO, *J. Geophys. Res.*, 114, D00B11, doi:10.1029/2008JD009984
- 1163 Hegglin, M. I., et al. (2013), SPARC Data Initiative: Comparison of water vapor climatologies from international
 1164 satellite limb sounders, *J. Geophys. Res. Atmos.*, 118, 11,824– 11,846, doi:10.1002/jgrd.50752
- 1165 Hendon, H.H.,Thompson, D.W., Lim, E.-P., Butler, A.H., Newman, P.A., Coy, L et al. (2019), Rare forecasted
 1166 climate event under way in the Southern Hemisphere, *Nature*, 573(7775), 495–495. doi:10.1038/d41586-019-
 1167 02858-0
- 1168 Hersbach, H, Bell, B, Berrisford, P, et al. (2020) The ERA5 global reanalysis. *Q J R Meteorol*
 1169 *Soc.*, 146: 1999– 2049. <https://doi.org/10.1002/qj.3803>
- 1170 Hollingsworth, A., Engelen, R. J., Textor, C., Benedetti, A., Boucher, O., Chevallier, F., Dethof, A., Elbern, H.,
 1171 Eskes, H., Flemming, J., Granier, C., Kaiser, J. W., Morcrette, J.-J., Rayner, R., Peuch, V.-H., Rouil, L.,
 1172 Schultz, M. G., Simmons, A. J., and The GEMS Consortium (2008), Toward a Monitoring and Forecasting
 1173 System For Atmospheric Composition: The GEMS Project, *B. Am. Meteorol. Soc.*, 89, 1147–1164,
 1174 <https://doi.org/10.1175/2008BAMS2355.1>
- 1175 Hurst, D. F., Lambert, A., Read, W. G., Davis, S. M., Rosenlof, K. H., Hall, E. G., Jordan, A. F., and Oltmans, S. J.
 1176 (2014), Validation of Aura Microwave Limb Sounder stratospheric water vapor measurements by the NOAA
 1177 frost point hygrometer, *J. Geophys. Res. Atmos.*, 119, 1612– 1625, doi:10.1002/2013JD020757
- 1178 Inness, A., Baier, F., Benedetti, A., Bouarar, I., Chabrillat, S., Clark, H., Clerbaux, C., Coheur, P., Engelen, R. J.,
 1179 Errera, Q., Flemming, J., George, M., Granier, C., Hadji-Lazaro, J., Huijnen, V., Hurtmans, D., Jones, L.,
 1180 Kaiser, J. W., Kapsomenakis, J., Lefever, K., Leitão, J., Razinger, M., Richter, A., Schultz, M. G., Simmons, A.
 1181 J., Suttie, M., Stein, O., Thépaut, J.-N., Thouret, V., Vrekoussis, M., Zerefos, C., and the MACC team (2013),
 1182 The MACC reanalysis: an 8 yr data set of atmospheric composition, *Atmos. Chem. Phys.*, 13, 4073–4109,
 1183 <https://doi.org/10.5194/acp-13-4073-2013>
- 1184 Inness, A., Ades, M., Agustí-Panareda, A., Barré, J., Benedictow, A., Blechschmidt, A.-M., Dominguez, J. J.,
 1185 Engelen, R., Eskes, H., Flemming, J., Huijnen, V., Jones, L., Kipling, Z., Massart, S., Parrington, M., Peuch,
 1186 V.-H., Razinger, M., Remy, S., Schulz, M., and Suttie, M. (2019), The CAMS reanalysis of atmospheric
 1187 composition, *Atmos. Chem. Phys.*, 19, 3515–3556, <https://doi.org/10.5194/acp-19-3515-2019>
- 1188 Jazwinski, A. H. (1970), Stochastic processes and filtering theory. Academic Press, Inc. New York, New York.

- 1189 Johansson, S., Woiwode, W., Höpfner, M., Friedl-Vallon, F., Kleinert, A., Kretschmer, E., Latzko, T., Orphal, J.,
 1190 Preusse, P., Ungermann, J., Santee, M. L., Jurkat-Witschas, T., Marsing, A., Voigt, C., Giez, A., Krämer, M.,
 1191 Rolf, C., Zahn, A., Engel, A., Sinnhuber, B.-M., and Oelhaf, H. (2018), Airborne limb-imaging measurements
 1192 of temperature, HNO₃, O₃, ClONO₂, H₂O and CFC-12 during the Arctic winter 2015/2016: characterization,
 1193 in situ validation and comparison to Aura/MLS, *Atmos. Meas. Tech.*, 11, 4737–4756,
 1194 <https://doi.org/10.5194/amt-11-4737-2018>
- 1195 Kablick, G.P., Allen, D.R., Fromm, M.D., and Nedoluha, G.E. (2020), Australian PyroCb smoke generates
 1196 synoptic-scale stratospheric anticyclones, *Geophys. Res. Lett.*, 47, e2020GL088101, doi:10.1029/2020GL088101
- 1197 Khaykin, S., Legras, B., Bucci, S. et al. (2020), The 2019/20 Australian wildfires generated a persistent smoke-
 1198 charged vortex rising up to 35 km altitude. *Commun. Earth Environ.*, 1, 22, doi:10.1038/s43247-020-00022-5
- 1199 Khosrawi, F., Kirner, O., Sinnhuber, B.-M., Johansson, S., Höpfner, M., Santee, M. L., Froidevaux, L., Ungermann,
 1200 J., Ruhnke, R., Woiwode, W., Oelhaf, H., and Braesicke, P. (2017), Denitrification, dehydration and ozone loss
 1201 during the 2015/2016 Arctic winter, *Atmos. Chem. Phys.*, 17, 12893–12910, [https://doi.org/10.5194/acp-17-](https://doi.org/10.5194/acp-17-12893-2017)
 1202 12893-2017
- 1203 Lahoz, W. A. and Schneider, P. (2014), Data assimilation: making sense of Earth Observation, *Front. Environ. Sci.*,
 1204 2, <https://doi.org/10.3389/fenvs.2014.00016>
- 1205 Lawrence, Z.D., Perlwitz, J., Butler, A.H., Manney, G.L., Newman, P.A., Lee, S.H., and S.H., Nash, E.R. (2020),
 1206 The remarkably strong Arctic stratospheric polar vortex of winter 2020: Links to record-breaking Arctic
 1207 Oscillation and ozone loss, *J. Geophys. Res.*, 125, e2020JD033271, doi:10.1029/2020JD033271
- 1208 Levelt, P. F., van den Oord, G. H. J., Dobber, M. R., Mälkki, A., Visser, H., Vries, J. D., Stammes, P., Lundell, J. O.
 1209 V., and Saari, H. (2006), The Ozone Monitoring Instrument, *IEEE Trans. Geosci. Remote Sens.*, 44, 1093–
 1210 1101, <https://doi.org/10.1109/TGRS.2006.872333>
- 1211 Levelt, P. F., Joiner, J., Tamminen, J., Veefkind, J. P., Bhartia, P. K., Stein Zweers, D. C., Duncan, B., et al. (2018),
 1212 The Ozone Monitoring Instrument: overview of 14 years in space, *Atmos. Chem. Phys.*, 18, 5699–5745,
 1213 <https://doi.org/10.5194/acp-18-5699-2018>
- 1214 Livesey, N. J., Read, W. G., Wagner, P. A., Froidevaux, L., Lambert, A., Manney, G. L. et al. (2020) Version 4.2x
 1215 Level 2 and 3 data quality and description document, JPL D-33509 Rev. E. Retrieved from
 1216 https://mls.jpl.nasa.gov/data/v4-2_data_quality_document.pdf
- 1217 Livesey, N. J., Read, W. G., Froidevaux, L., Lambert, A., Santee, M. L., Schwartz, M. J., Millán, L. F., Jarnot, R. F.,
 1218 Wagner, P. A., Hurst, D. F., Walker, K. A., Sheese, P. E., and Nedoluha, G. E. (2021), Investigation and
 1219 amelioration of long-term instrumental drifts in water vapor and nitrous oxide measurements from the Aura
 1220 Microwave Limb Sounder (MLS) and their implications for studies of variability and trends, *Atmos. Chem.*
 1221 *Phys.*, 21, 15409–15430, <https://doi.org/10.5194/acp-21-15409-2021>
- 1222 Livesey, N. J., Read, W. G., Wagner, P. A., Froidevaux, L., Santee, M. L., Schwartz, M. J. et al. (2022), Version
 1223 5.0x Level 2 and 3 data quality and description document, JPL D-105336 Rev. B. Retrieved from
 1224 https://mls.jpl.nasa.gov/data/v5-0_data_quality_document.pdf
- 1225 Manney, G.L., Santee, M.L., Livesey, N.J., Froidevaux, L., Pumphrey, H.C., Read, and W.G., Waters, J.W. (2005),
 1226 EOS Microwave Limb Sounder Observations of the Antarctic Polar Vortex Breakup in 2004, *Geophys. Res.*
 1227 *Lett.*, 32, L12811, doi:10.1029/2005GL022823
- 1228 Manney, G. L., et al. (2008), The evolution of the stratopause during the 2006 major warming: Satellite data and
 1229 assimilated meteorological analyses, *J. Geophys. Res.*, 113, D11115, doi:10.1029/2007JD009097
- 1230 Manney, G.L., et al. (2009a), Satellite Observations and Modelling of Transport in the Upper Troposphere through
 1231 the Lower Mesosphere During the 2006 Major Stratospheric Sudden Warming, *Atmos. Chem. Phys.*, 9, 4775–
 1232 4795
- 1233 Manney, G. L., Schwartz, M. J., Krüger, K., Santee, M. L., Pawson, S., Lee, J. N., Daffer, W. H., Fuller, R. A.,
 1234 and Livesey, N. J. (2009b), Aura Microwave Limb Sounder observations of dynamics and transport during the
 1235 record-breaking 2009 Arctic stratospheric major warming, *Geophys. Res. Lett.*, 36, L12815,
 1236 doi:10.1029/2009GL038586
- 1237 Manney, G.L., Santee, M.L., Rex, M., Livesey, N.J., Pitts, M.L.C., Veefkind, P. et al. (2011), Unprecedented
 1238 Arctic ozone loss in 2011, *Nature*, 478, 469–475, doi:10.1038/nature10556
- 1239 Manney, G. L. and Lawrence, Z. D. (2016), The major stratospheric final warming in 2016: dispersal of vortex air
 1240 and termination of Arctic chemical ozone loss, *Atmos. Chem. Phys.*, 16, 15371–15396,
 1241 <https://doi.org/10.5194/acp-16-15371-2016>
- 1242 Manney, G. L., Livesey, N. J., Santee, M. L., Froidevaux, L., Lambert, A., & Lawrence, Z. D., et al. (2020), Record-
 1243 low Arctic stratospheric ozone in 2020: MLS observations of chemical processes and comparisons with

- 1244 previous extreme winters. *Geophysical Research Letters*, 47,
 1245 e2020GL089063. <https://doi.org/10.1029/2020GL089063>
- 1246 McIntyre, M.E. and Palmer, T.N. (1983), Breaking planetary waves in the stratosphere. *Nature*, 305, 593–600
- 1247 Ménard, R., Skachko, S., and Pannekoucke, O. (2021), Numerical discretization causing error variance loss and the
 1248 need for inflation, *Q. J. Roy. Meteor. Soc.*, 147, 3498–3520, <https://doi.org/10.1002/qj.4139>
- 1249 Miyazaki, K., Bowman, K., Sekiya, T., Eskes, H., Boersma, F., Worden, H., Livesey, N., Payne, V. H., Sudo, K.,
 1250 Kanaya, Y., Takigawa, M., and Ogochi, K. (2020), Updated tropospheric chemistry reanalysis and emission
 1251 estimates, TCR-2, for 2005–2018, *Earth Syst. Sci. Data*, 12, 2223–2259, <https://doi.org/10.5194/essd-12-2223-2020>
- 1252 Nakamura, N. (1996), Two-Dimensional Mixing, Edge Formation, and Permeability Diagnosed in an Area
 1253 Coordinate, *Journal of Atmospheric Sciences*, 53(11), 1524–1537
- 1254 Nichols, N. K. (2010), Mathematical concepts of data assimilation, in *Data Assimilation: Making Sense of*
 1255 *Observations*, eds W. A. Lahoz, B. Khattatov, and R. Ménard (Berlin; Heidelberg: Springer), 13–39
- 1256 Nielsen, J. E., Pawson, S., Molod, A., Auer, B., da Silva, A. M., Douglass, A. R., et al. (2017), Chemical
 1257 mechanisms and their applications in the Goddard Earth Observing System (GEOS) earth system model. *J.*
 1258 *Adv. Mod. Earth Sys.*, 9, 3019–3044. <https://doi.org/10.1002/2017MS001011>
- 1259 Orbe, C., Oman, L. D., Strahan, S. E., Waugh, D. W., Pawson, S., Takacs, L. L., & Molod, A. M. (2017), Large-
 1260 scale atmospheric transport in GEOS replay simulations. *J. Adv. Mod. Earth Sys.*, 9. <https://doi.org/10.1002/2017MS001053>
- 1261 Park, M., Randel, W. J., Damadeo, R. P., Flittner, D. E., Davis, S. M., Rosenlof, K. H., et al. (2021), Near-global
 1262 variability of stratospheric water vapor observed by SAGE III/ISS. *J. of Geoph. Res.: Atmospheres*, 126,
 1263 e2020JD034274. <https://doi.org/10.1029/2020JD034274>
- 1264 Plumb, R. A. (2007), Tracer interrelationships in the stratosphere, *Rev. Geophys.*, 45, RG4005,
 1265 doi:10.1029/2005RG000179
- 1266 Randel, W. and Park, M. (2019), Diagnosing observed stratospheric water vapor relationships to the cold point
 1267 tropical tropopause. *J. of Geoph. Res.: Atmospheres*, 124, 7018–7033. <https://doi.org/10.1029/2019JD030648>
- 1268 Reich, S. (2019), Data assimilation: the Schrödinger perspective. *Acta Numerica*, 28, 635–711
- 1269 Rieger, L. A., Randel, W. J., Bourassa, A. E., & Solomon, S. (2021), Stratospheric temperature and ozone anomalies
 1270 associated with the 2020 Australian New Year Fires. *Geoph. Res. Lett.*, 48, e2021GL095898.
 1271 <https://doi.org/10.1029/2021GL095898>
- 1272 Safieddine, S., Bouillon, M., Paracho, A.-C., Jumelet, J., Tencé, R., Pazmino, A., Goutail, F., Wespes, C., Bekki,
 1273 S., Boynard, A., Hadji-Lazaro, J., Coheur, P.-F., Hurtmans, D., and Clerbaux, C. (2020), Antarctic ozone
 1274 enhancement during the 2019 sudden stratospheric warming event, *Geophys. Res. Lett.*, 47, e2020GL087810,
 1275 doi:10.1029/2020GL087810
- 1276 Santee, M.L., Manney, G.L., Livesey, N.J., Froidevaux, L., Schwartz, M.J., and Read, W.G. (2011), Trace gas
 1277 evolution in the lowermost stratosphere from Aura Microwave Limb Sounder measurements, *J. Geophys. Res.*,
 1278 116, D18306, doi:10.1029/2011JD015590
- 1279 Santee, M. L., Lambert, A., Manney, G. L., Livesey, N. J., Froidevaux, L., Neu, J. L., et al. (2022), Prolonged and
 1280 pervasive perturbations in the composition of the Southern Hemisphere midlatitude lower stratosphere from the
 1281 Australian New Year's fires. *Geoph. Res. Lett.*, 49, e2021GL096270. <https://doi.org/10.1029/2021GL096270>
- 1282 Schwartz, M. J., Manney, G. L., Hegglin, M. I., Livesey, N. J., Santee, M. L., and Daffer, W. H. (2015),
 1283 Climatology and variability of trace gases in extratropical double-tropopause regions from MLS, HIRDLS, and
 1284 ACE-FTS measurements, *J. Geophys. Res. Atmos.*, 120, doi:10.1002/2014JD021964
- 1285 Schwartz, M.J., Santee, M.L., Pumphrey, H.C., Manney, G.L., Lambert, A., Livesey, N.J., et al. (2020), Australian
 1286 New Year's pyroCb impact on stratospheric composition, *Geophys. Res. Lett.*, 47, e2020GL090831,
 1287 doi:10.1029/2020GL090831
- 1288 Sheese, P.E., Boone, C.D., and Walker, K.A. (2015), Detecting physically unrealistic outliers in ACE-FTS
 1289 atmospheric measurements, *Atmos. Meas. Tech.*, 8, 741–750, 2015. doi: 10.5194/amt-8-741-2015
- 1290 Sheese, P. E., Walker, K. A., Boone, C. D., Bernath, P. F., Froidevaux, L., Funke, B., Raspollini, P., and von
 1291 Clarmann, T. (2017), ACE-FTS ozone, water vapour, nitrous oxide, nitric acid, and carbon monoxide profile
 1292 comparisons with MIPAS and MLS, *Journal of Quantitative Spectroscopy and Radiative Transfer*, 186, 63–80,
 1293 doi:10.1016/j.jqsrt.2016.06.026
- 1294 Sheese, P.; Walker, K. (2020), "Data Quality Flags for ACE-FTS Level 2 Version 4.1/4.2 Data Set,
 1295 <https://doi.org/10.5683/SP2/BC4ATC>, *Scholars Portal Dataverse*, V15
- 1296 Shepherd, T. G. (2007), Transport in the middle atmosphere, *J. Meteorol. Soc. Japan*, 85B, 165–191

- 1299 Skachko, S., Ménard, R., Errera, Q., Christophe, Y., and Chabrillat, S. (2016), EnKF and 4D-Var data assimilation
 1300 with chemical transport model BASCOE (version 05.06), *Geosci. Model Dev.*, 9, 2893–2908,
 1301 <https://doi.org/10.5194/gmd-9-2893-2016>
- 1302 SPARC Reanalysis Intercomparison Project (S-RIP) (2021), Final Report. Masatomo Fujiwara, Gloria L. Manney,
 1303 Lesley J. Gray, and Jonathon S. Wright (Eds.), *SPARC Report No. 10*, WCRP-6/2021, doi:
 1304 10.17874/800dee57d13, available at www.sparc-climate.org/publications/sparc-reports
- 1305 Todling, R., and El Akkroui, A. (2018), The GMAO Hybrid Ensemble-Variational Atmospheric Data Assimilation
 1306 System: Version 2.0. *NASA Technical Report Series on Global Modeling and Data Assimilation*, NASA/TM-
 1307 2018-104606, 50. <https://gmao.gsfc.nasa.gov/pubs/docs/Todling1019.pdf>
- 1308 van der A, R. J., Allaart, M. A. F., and Eskes, H. J. (2015), Extended and refined multi sensor reanalysis of total
 1309 ozone for the period 1970–2012, *Atmos. Meas. Tech.*, 8, 3021–3035, <https://doi.org/10.5194/amt-8-3021-2015>
- 1310 Wang, H. J. R., Damadeo, R., Flittner, D., Kramarova, N., Taha, G., Davis, S., et al. (2020), Validation of SAGE
 1311 III/ISS solar occultation ozone products with correlative satellite and ground based measurements. *J. of Geoph.*
 1312 *Res. Atmos.*, 125, e2020JD032430. <https://doi.org/10.1029/2020JD032430>
- 1313 Wargan, K., Pawson, S., Olsen, M. A., Witte, J. C., Douglass, A. R., Ziemke, J. R., Strahan, S. E. & Nielsen, J. E.
 1314 (2015), The global structure of upper troposphere-lower stratosphere ozone in GEOS-5: A multiyear
 1315 assimilation of EOS Aura data. *J. Geophys. Res. Atmos.*, 120: 2013– 2036.
 1316 <https://doi.org/10.1002/2014JD022493>
- 1317 Wargan, K., Labow, G., Frith, S., Pawson, S., Livesey, N., & Partyka, G. (2017), Evaluation of the Ozone Fields in
 1318 NASA’s MERRA-2 Reanalysis. *J. Climate*, 30, 2961–2988, <https://doi.org/10.1175/JCLI-D-16-0699.1>
- 1319 Wargan, K., Kramarova, N., Weir, B., Pawson, S., & Davis, S. M. (2020a), Toward a reanalysis of stratospheric
 1320 ozone for trend studies: Assimilation of the Aura microwave limb sounder and ozone mapping and profiler suite
 1321 limb profiler data. *Journal of Geophysical Research: Atmospheres*, **125**,
 1322 e2019JD031892. <https://doi.org/10.1029/2019JD031892>
- 1323 Wargan, K., Weir, B., Manney, G. L., Cohn, S. E., & Livesey, N. J. (2020b), The anomalous 2019 Antarctic ozone
 1324 hole in the GEOS Constituent Data Assimilation System with MLS observations. *Journal of Geophysical*
 1325 *Research: Atmospheres*, 125, e2020JD033335. <https://doi.org/10.1029/2020JD033335>
- 1326 Waters, J. W., Froidevaux, L., Harwood, R.S., Jarnot, R.F., Pickett, H.M., Read, W.G. et al. (2006), The Earth
 1327 Observing System Microwave Limb Sounder (EOS MLS) on the Aura satellite. *IEEE Trans. Geosci. Remote*
 1328 *Sens.*, 44, 1075–1092. <https://doi.org/10.1109/TGRS.2006.873771>
- 1329 Weir, B., Miller, R. N., and Spitz, Y. H. (2013), Implicit Estimation of Ecological Model Parameters. *Bulletin of*
 1330 *Mathematical Biology*, 75 (2): 223-257. <https://doi.org/10.1007/s11538-012-9801-6>
- 1331 Weir, B., Crisp, D., O’Dell, C. W. et al. (2021), Regional impacts of COVID-19 on carbon dioxide detected
 1332 worldwide from space. *Science Advances*, 7 (45): doi:10.1126/sciadv.abf9415
- 1333 Wohltmann, I., von der Gathen, P., Lehmann, R., Maturilli, M., Deckelmann, H., Manney, G. L., et al. (2020), Near-
 1334 complete local reduction of Arctic stratospheric ozone by severe chemical loss in spring 2020. *Geoph. Res.*
 1335 *Lett.*, 47, e2020GL089547. <https://doi.org/10.1029/2020GL089547>
- 1336 Wohltmann, I., von der Gathen, P., Lehmann, R., Deckelmann, H., Manney, G. L., Davies, J., et al. (2021),
 1337 Chemical evolution of the exceptional Arctic stratospheric winter 2019/2020 compared to previous Arctic and
 1338 Antarctic winters. *J. of Geoph. Res. Atmos.*, 126, e2020JD034356. <https://doi.org/10.1029/2020JD034356>
- 1339 Wu, W.S., Purser, R.J., Parrish, D.F. (2002), Three-dimensional variational analysis with spatially inhomogeneous
 1340 covariances. *Mon. Weather Rev.* 130, 2905–2916
- 1341 Ziemke, J. R., et al. (2014) Assessment and applications of NASA ozone data products derived from Aura
 1342 OMI/MLS satellite measurements in context of the GMI chemical transport model. *J. Geophys. Res. Atmos.*,
 1343 119, doi:10.1002/2013JD020914

M2-SCREAM: A Stratospheric Composition Reanalysis of Aura MLS data with MERRA-2 transport

Krzysztof Wargan^{1,2}, Brad Weir^{2,3,†}, Gloria L. Manney^{4,5}, Stephen E. Cohn², K. Emma Knowland^{2,3,†}, Pamela A. Wales^{2,3,†}, and Nathaniel J. Livesey⁶

¹ Science Systems and Applications Inc., Lanham, Maryland, USA

² Global Modeling and Assimilation Office, NASA Goddard Space Flight Center, Greenbelt, Maryland, USA

³ Universities Space Research Association, Columbia, Maryland, USA

⁴ NorthWest Research Associates, Socorro, New Mexico, USA

⁵ Department of Physics, New Mexico Institute of Mining and Technology, Socorro, New Mexico, USA

⁶ Jet Propulsion Laboratory, California Institute of Technology, Pasadena, California, USA

[†] Now Morgan State University, Baltimore, Maryland, USA

Corresponding author: Krzysztof Wargan (krzysztof.wargan-1@nasa.gov)

Contents of this file

Figures S1 to S18

Additional Supporting Information (Files uploaded separately)

Captions for Movies S1 to S3

Introduction

This file contains supplementary figures and movie captions for “M2-SCREAM: A Stratospheric Composition Reanalysis of Aura MLS data with MERRA-2 transport”. Figure S1 shows observation minus forecast statistics for water vapor, HCl, HNO₃, and N₂O, analogous to Figure 3a and b in the main text. Figure S2 plots global zonal mean comparisons between M2-SCREAM and BRAM2. Figures S3–S16 show comparisons of M2-SCREAM HNO₃, H₂O, and ozone with GLORIA data from individual flights during the joint Polar Stratosphere in a Changing Climate, Gravity Wave Life Cycle Experiment, and Seasonality of Air mass transport and origin in the Lowermost Stratosphere using the HALO Aircraft campaigns. These are analogous to Figure 6 in the main text. Figures S17 and S18 show statistical comparisons of M2-SCREAM with ACE-FTS as in Figure 10 but limited to 30°N–60°N and for December–January 2005–2020. Animations S1–S3 show all available frost point hygrometer water vapor profile observations between 2005 and 2021 and collocated M2-SCREAM profiles. These are discussed in Section 6.1 of the main text. Figure 7 shows statistical comparisons calculated using the data displayed in the animations.

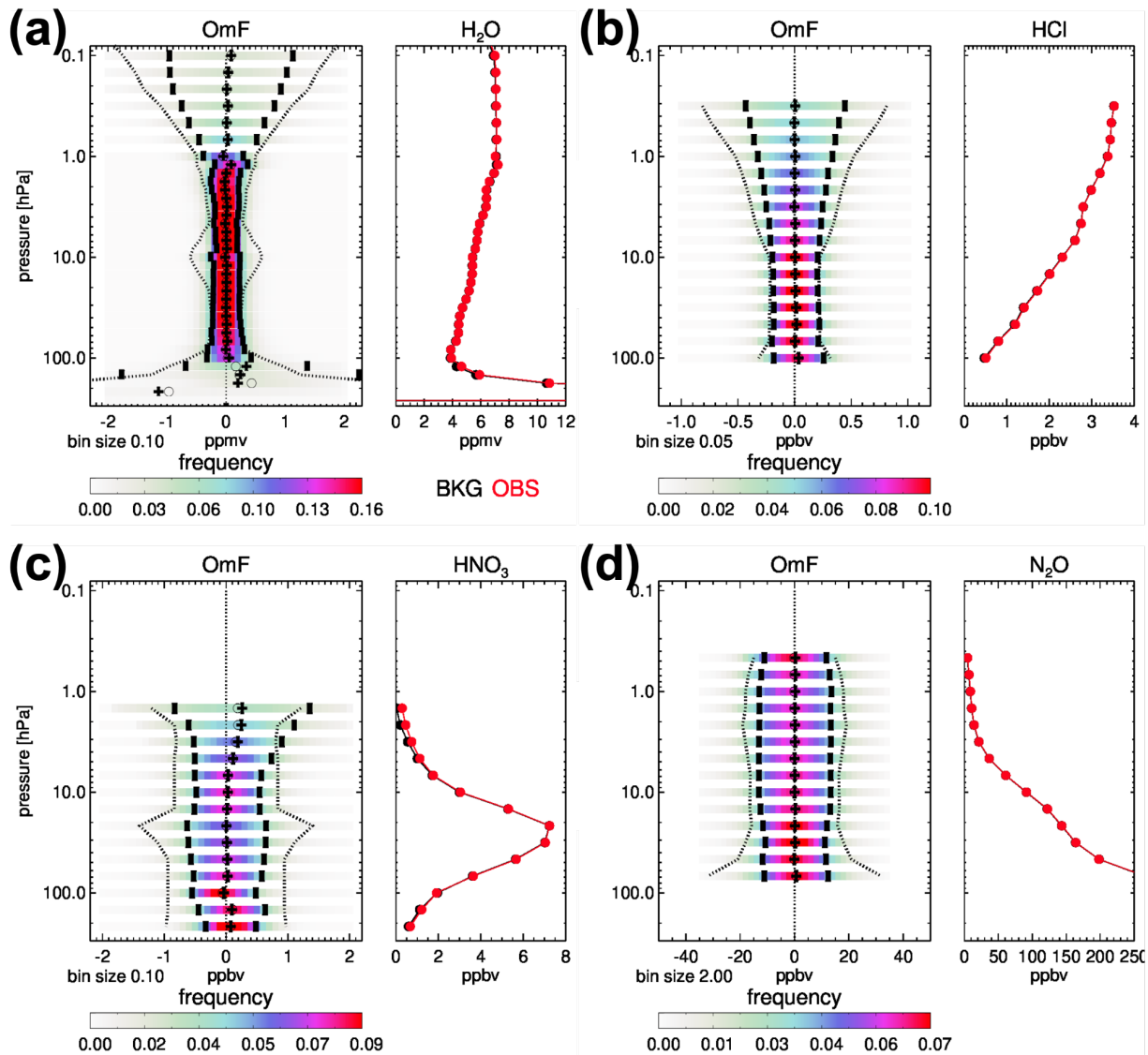


Figure S1: Internal global SCREAM statistics for H_2O (a), HCl (b), HNO_3 (c), and N_2O (d). The right-hand side panels show the mean background and MLS profiles. Observation minus forecast (O-F) statistics are plotted in the left-hand side panels. Shown are the O-F mean (plus signs), median (open circles), standard deviations around the mean (short vertical bars), probability density functions (colors) at prescribed pressure levels. The dotted lines are plus/minus MLS uncertainty estimates. Valid for January 2005.

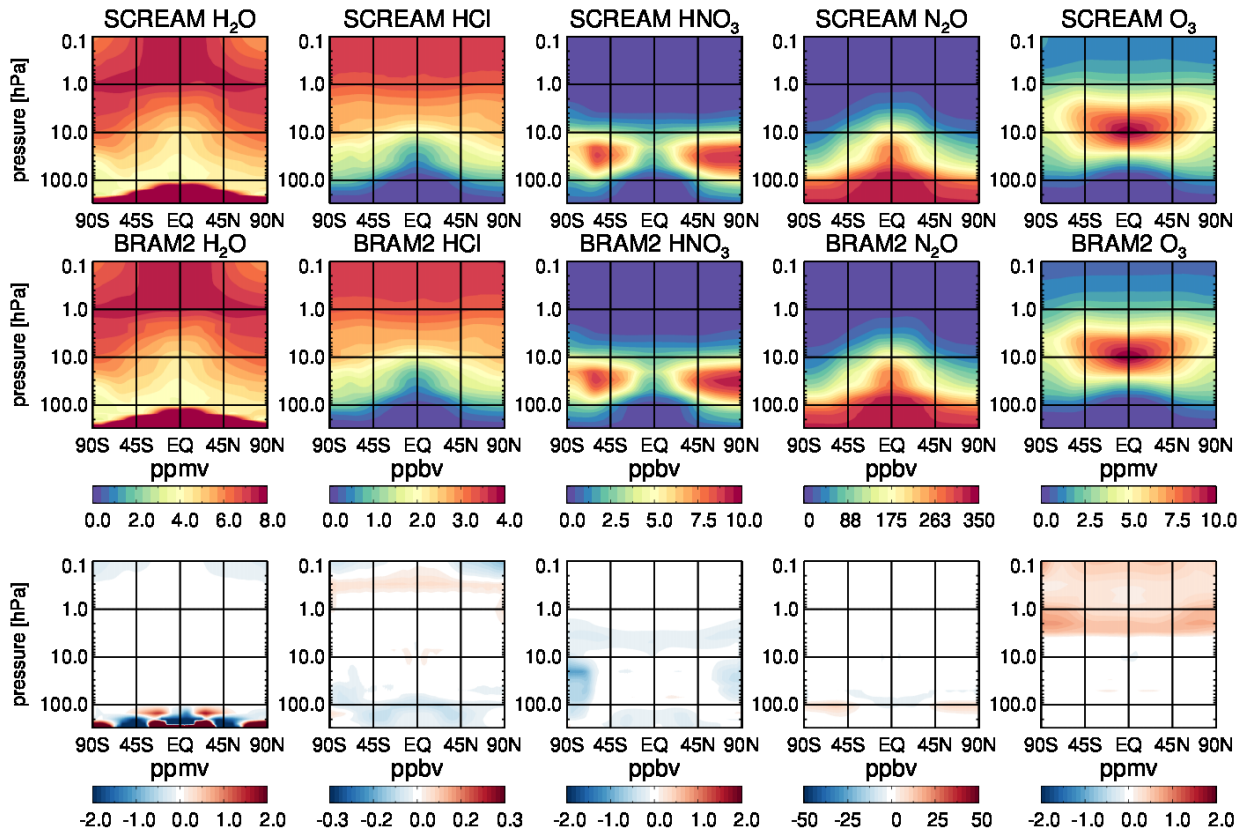


Figure S2: Zonal mean mixing ratios of the assimilated constituents from the BRAM2 reanalysis (a) and SCREAM (b). The SCREAM minus BRAM2 differences are shown in (c).

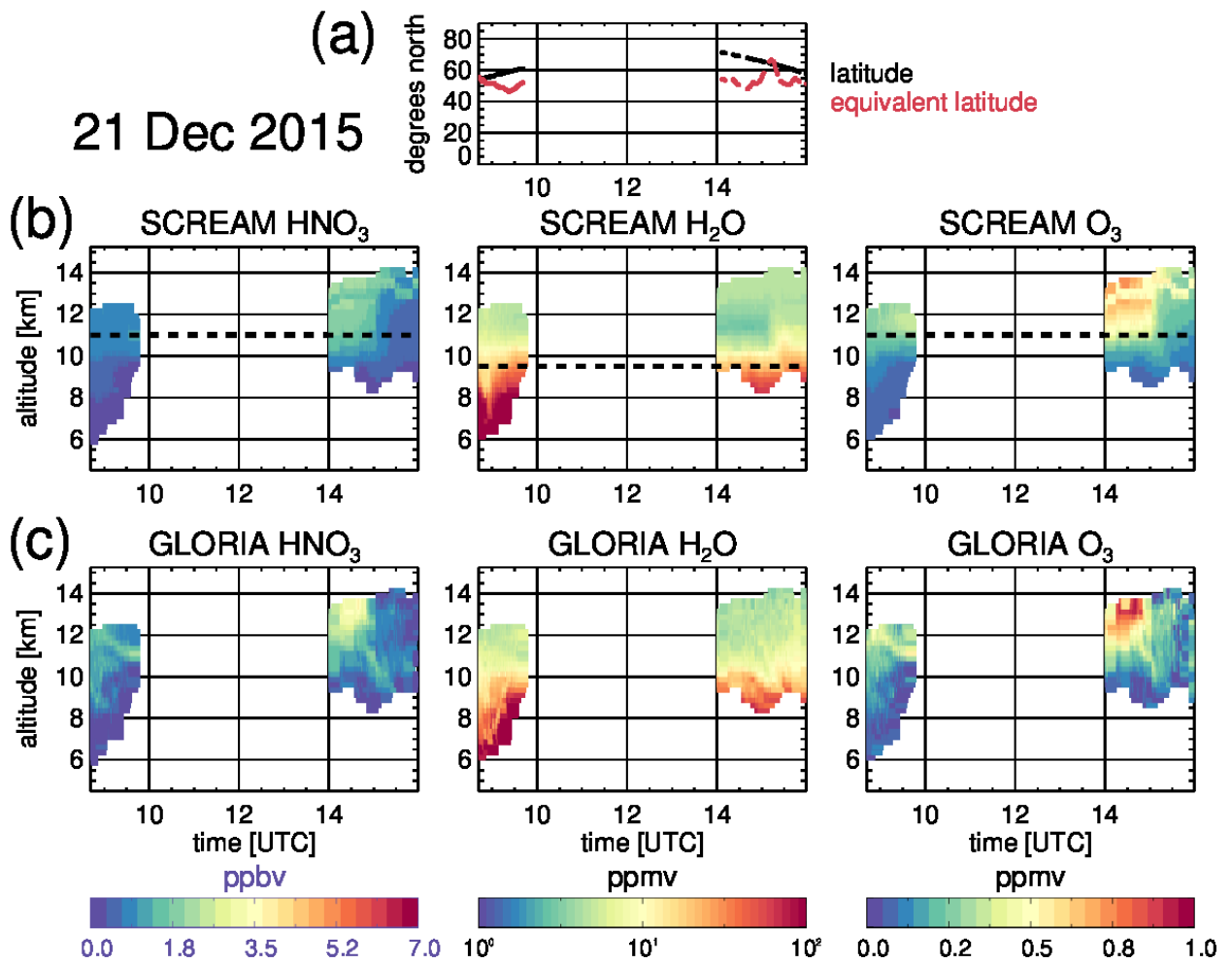


Figure S3: (a) Latitudes and equivalent latitudes of the GLORIA measurements at 10 km. (b) M2-SCREAM HNO₃, water vapor, and ozone collocated with GLORIA measurements during a single flight on 21 December 2015. The dashed lines mark the lowest altitudes of MLS observations assimilated in M2-SCREAM. (c) GLORIA observations.

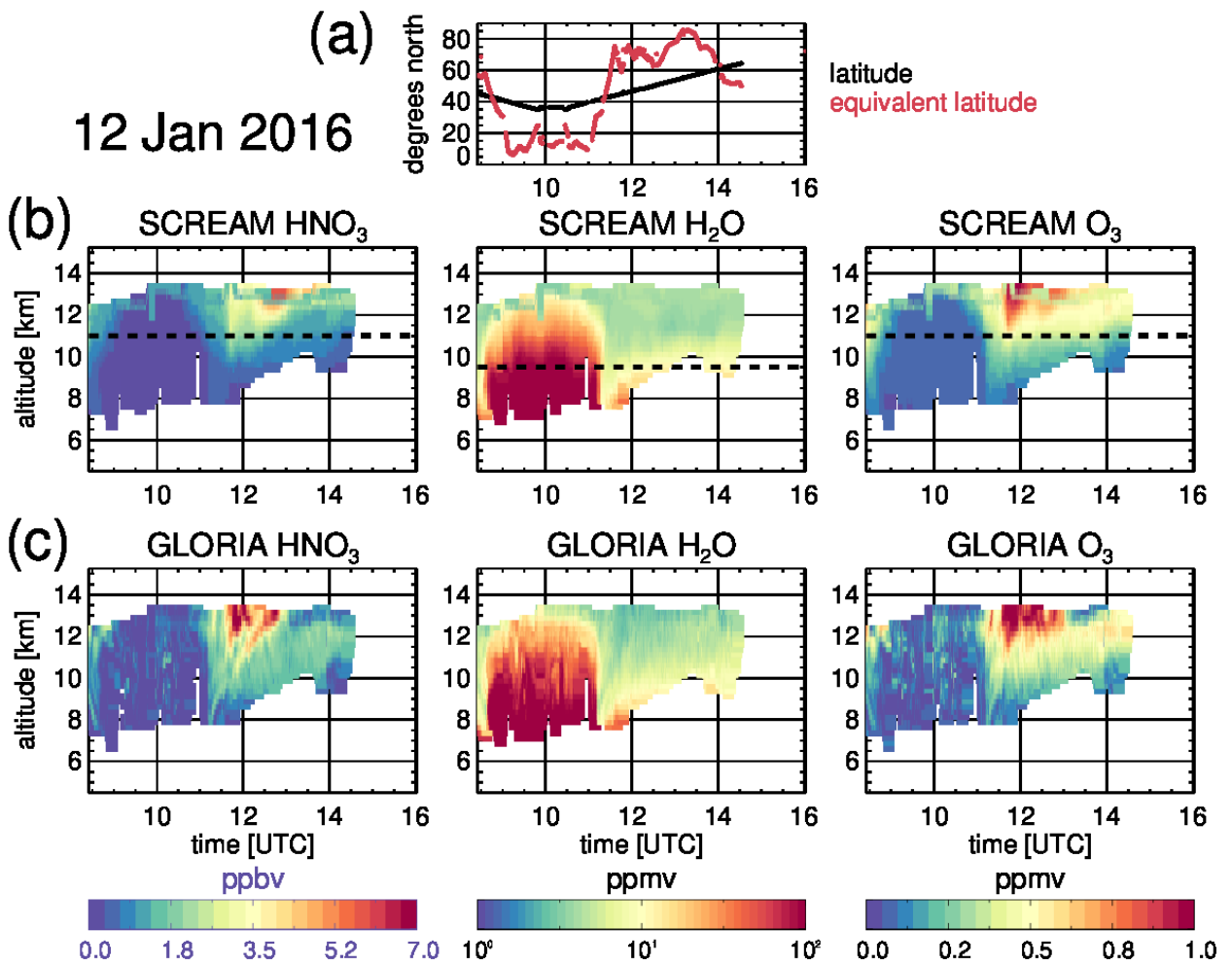


Figure S4: As in Fig. S3 but for 12 January 2016.

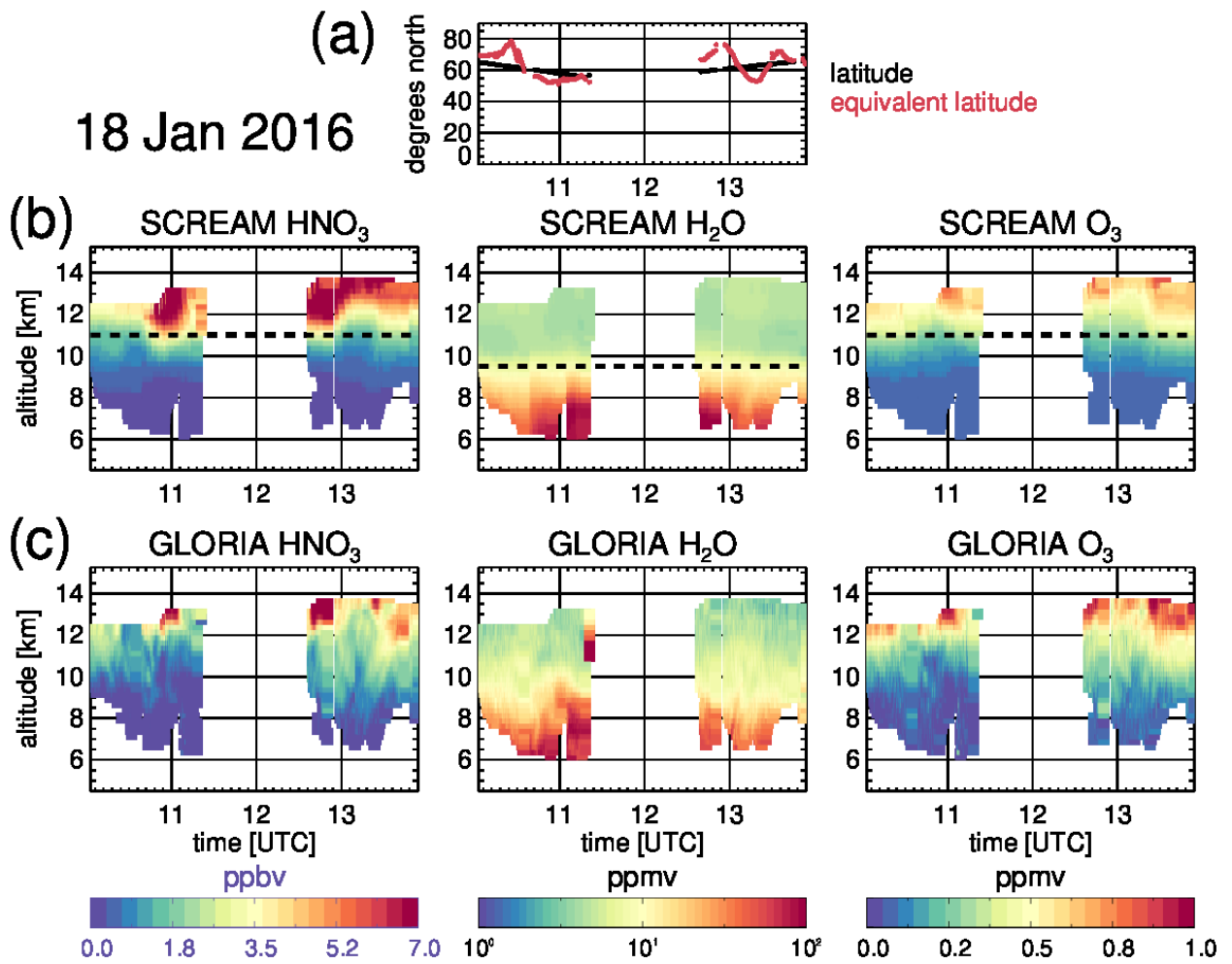


Figure S5: As in Fig. S3 but for 18 January 2016.

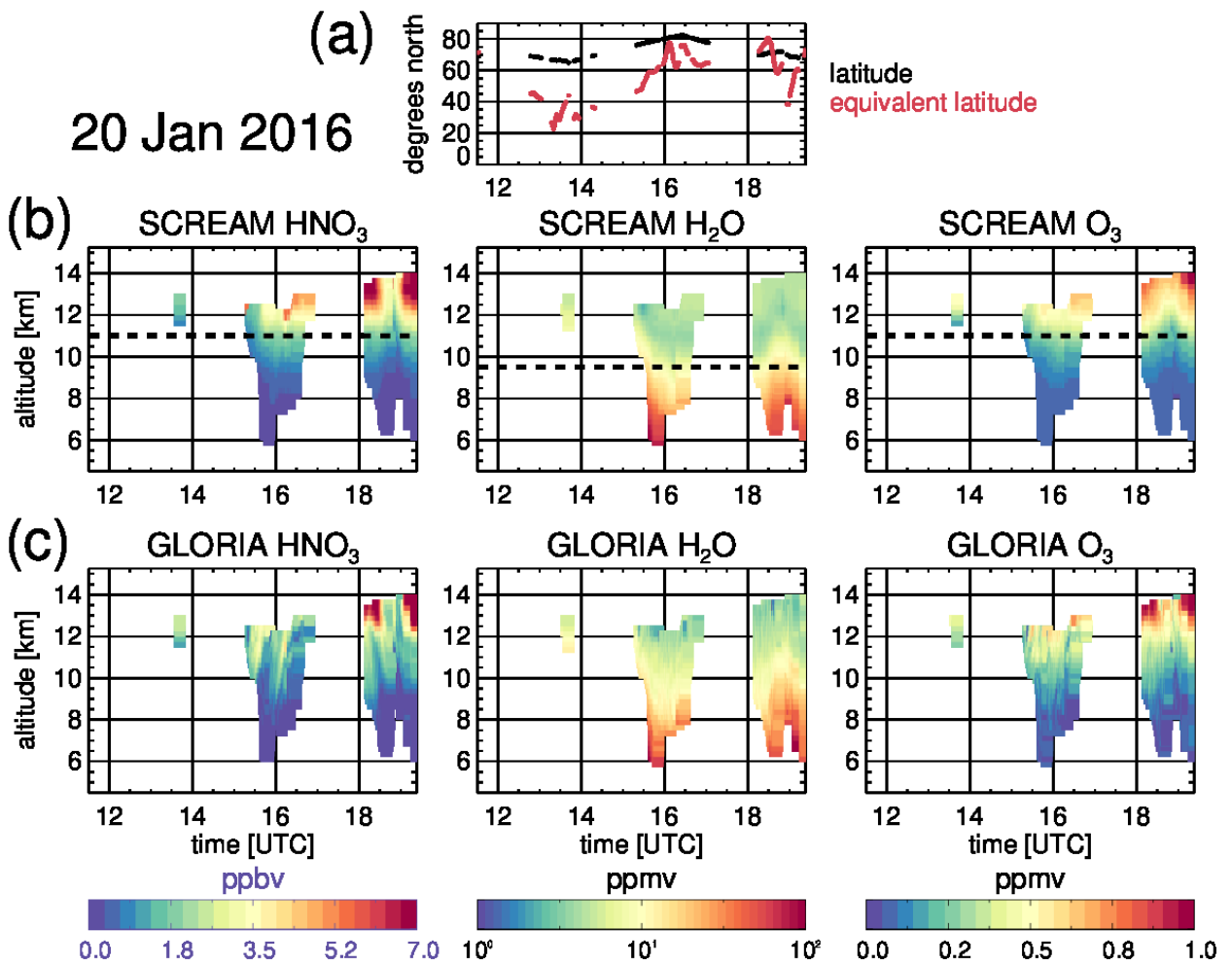


Figure S6: As in Fig. S3 but for 20 January 2016.

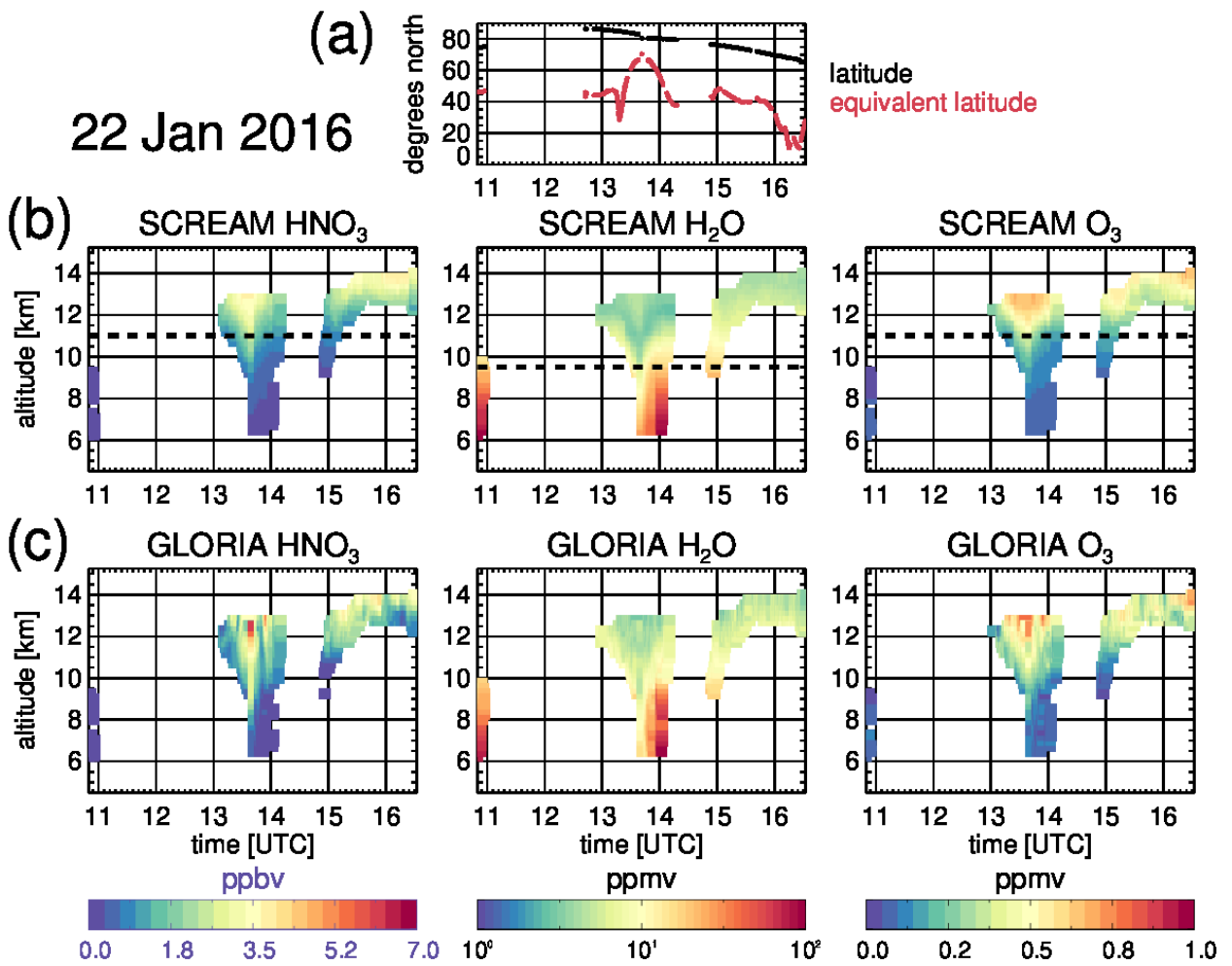


Figure S7: As in Fig. S3 but for 22 January 2016.

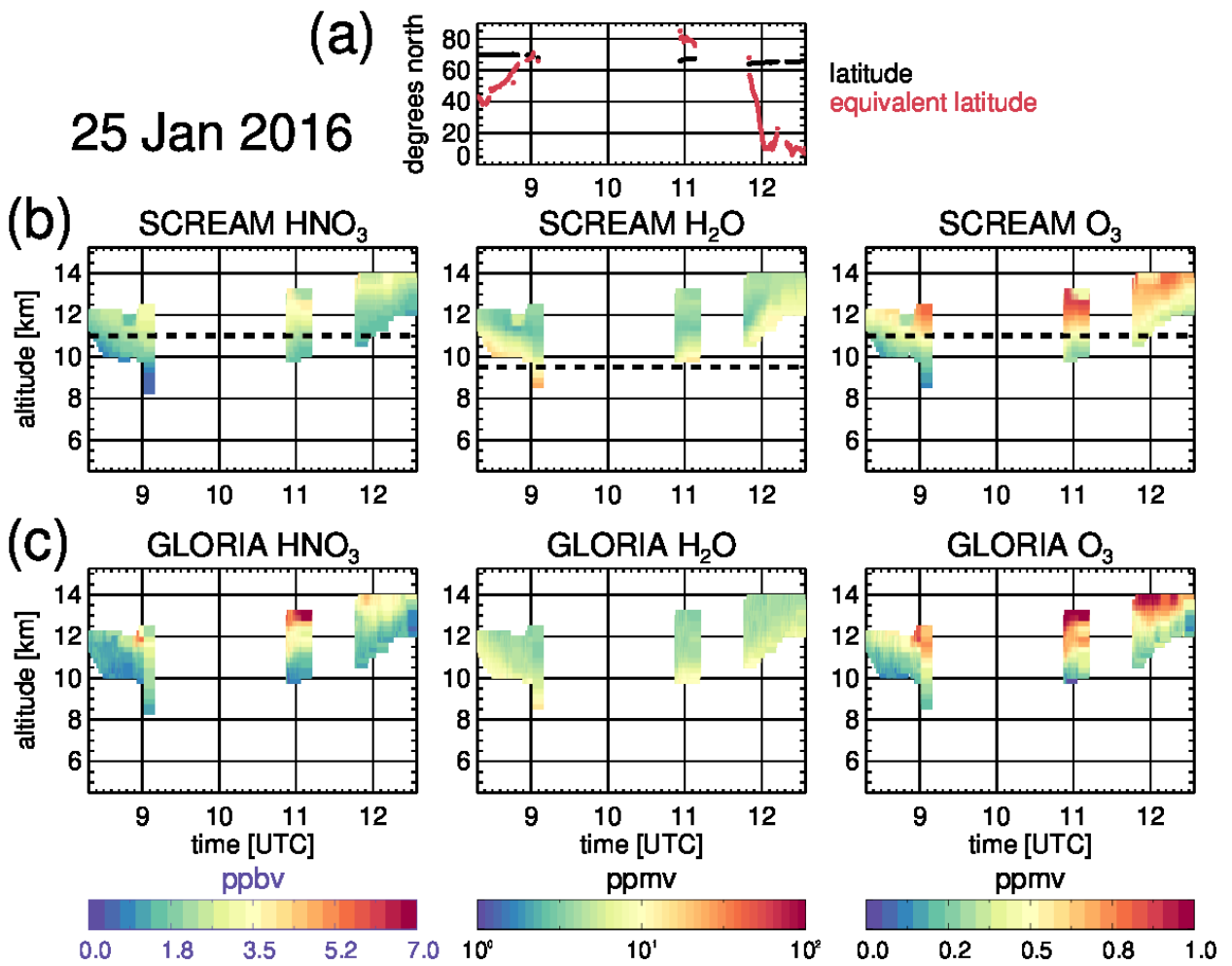


Figure S8: As in Fig. S3 but for 25 January 2016.

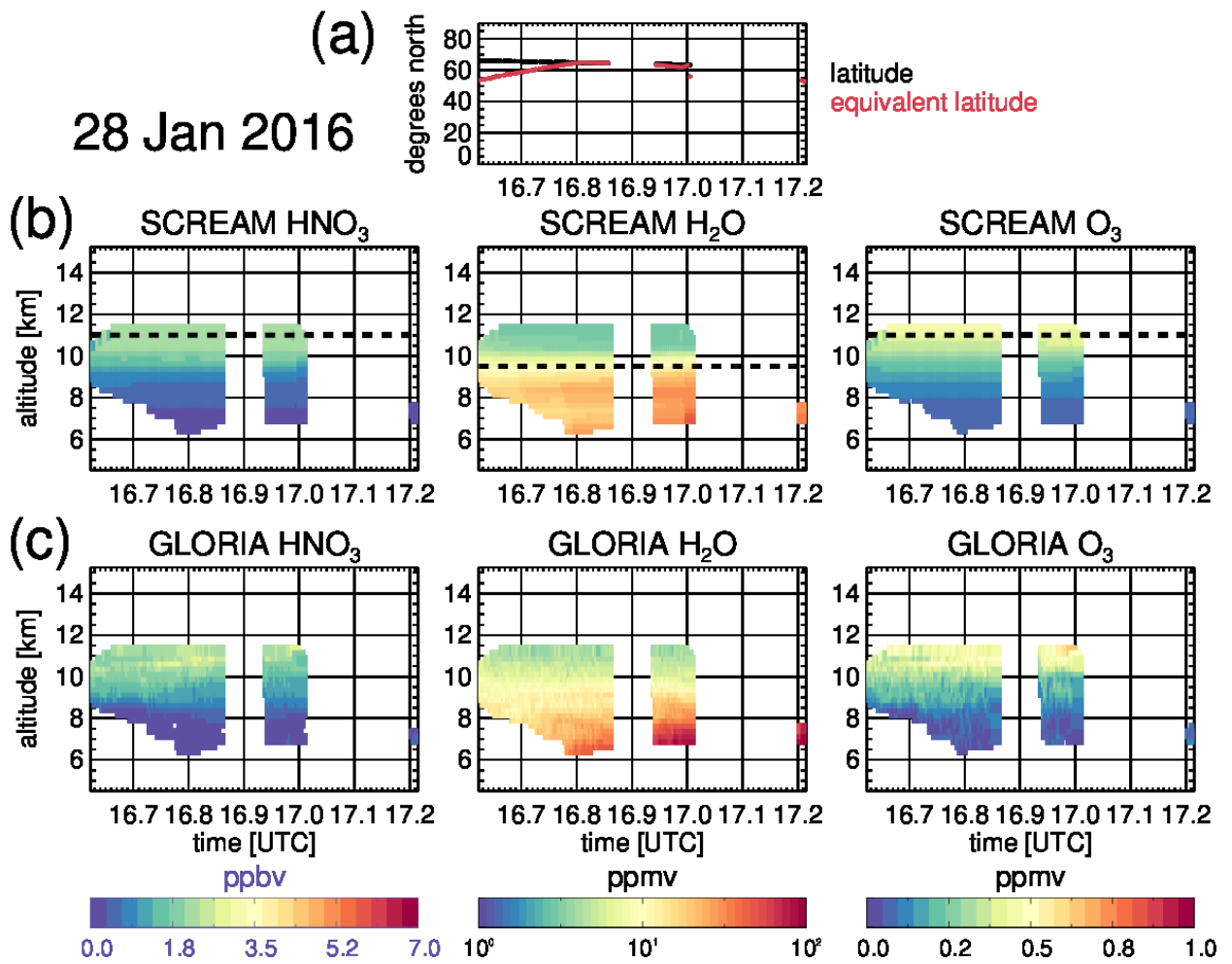


Figure S9: As in Fig. S3 but for 28 January 2016.

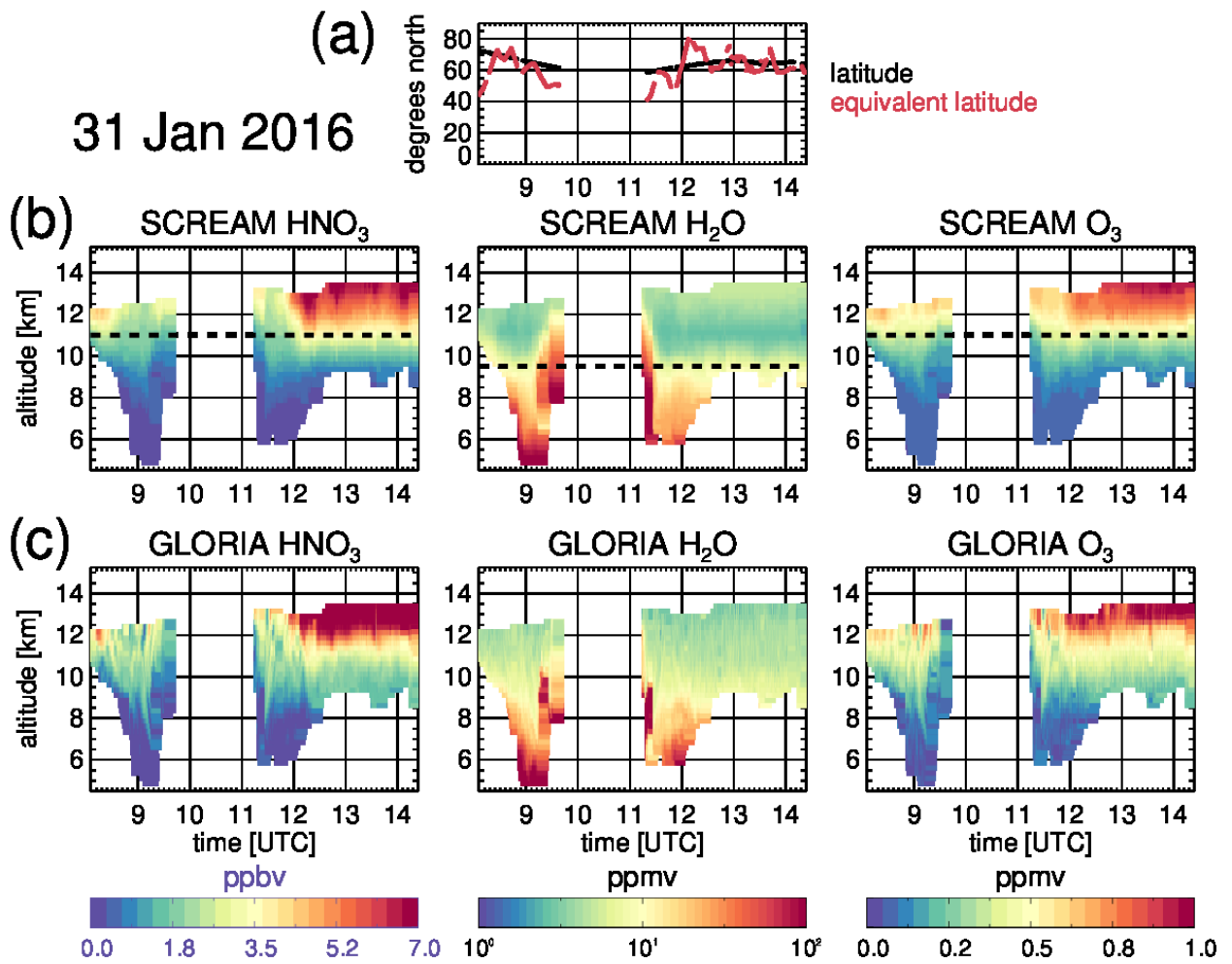


Figure S10: As in Fig. S3 but for 31 January 2016.

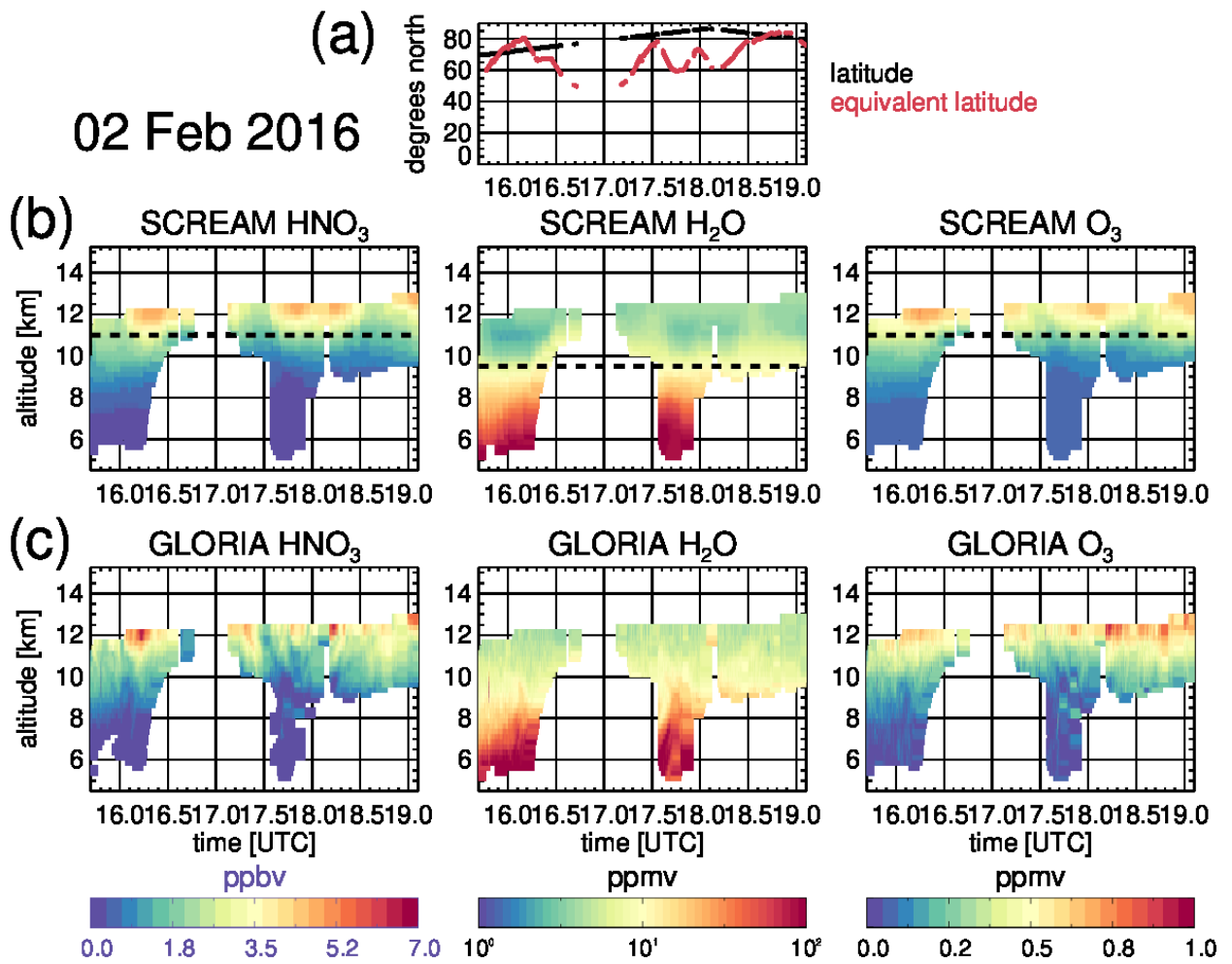


Figure S11: As in Fig. S3 but for 2 February 2016.

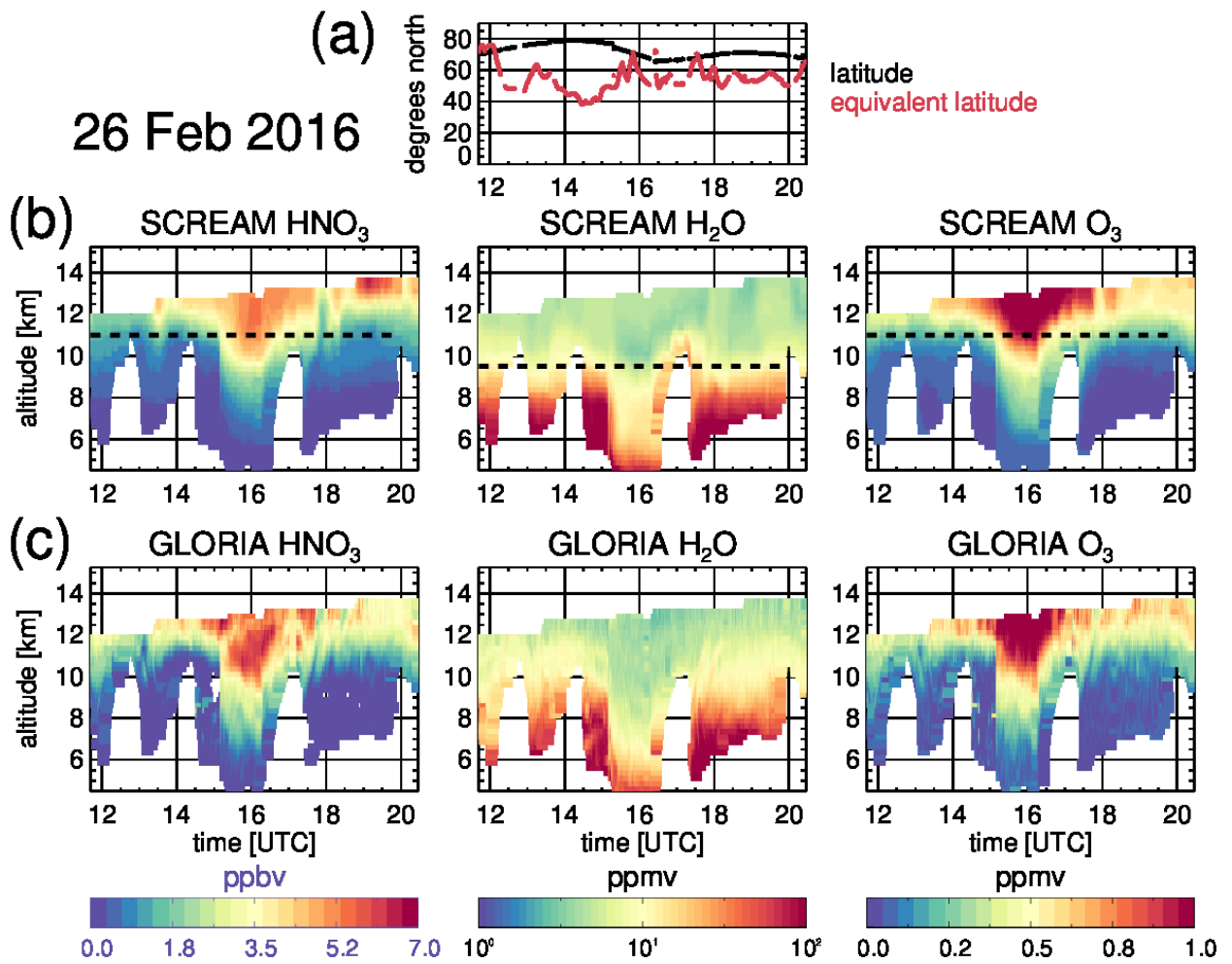


Figure S12: As in Fig. S3 but for 26 February 2016.

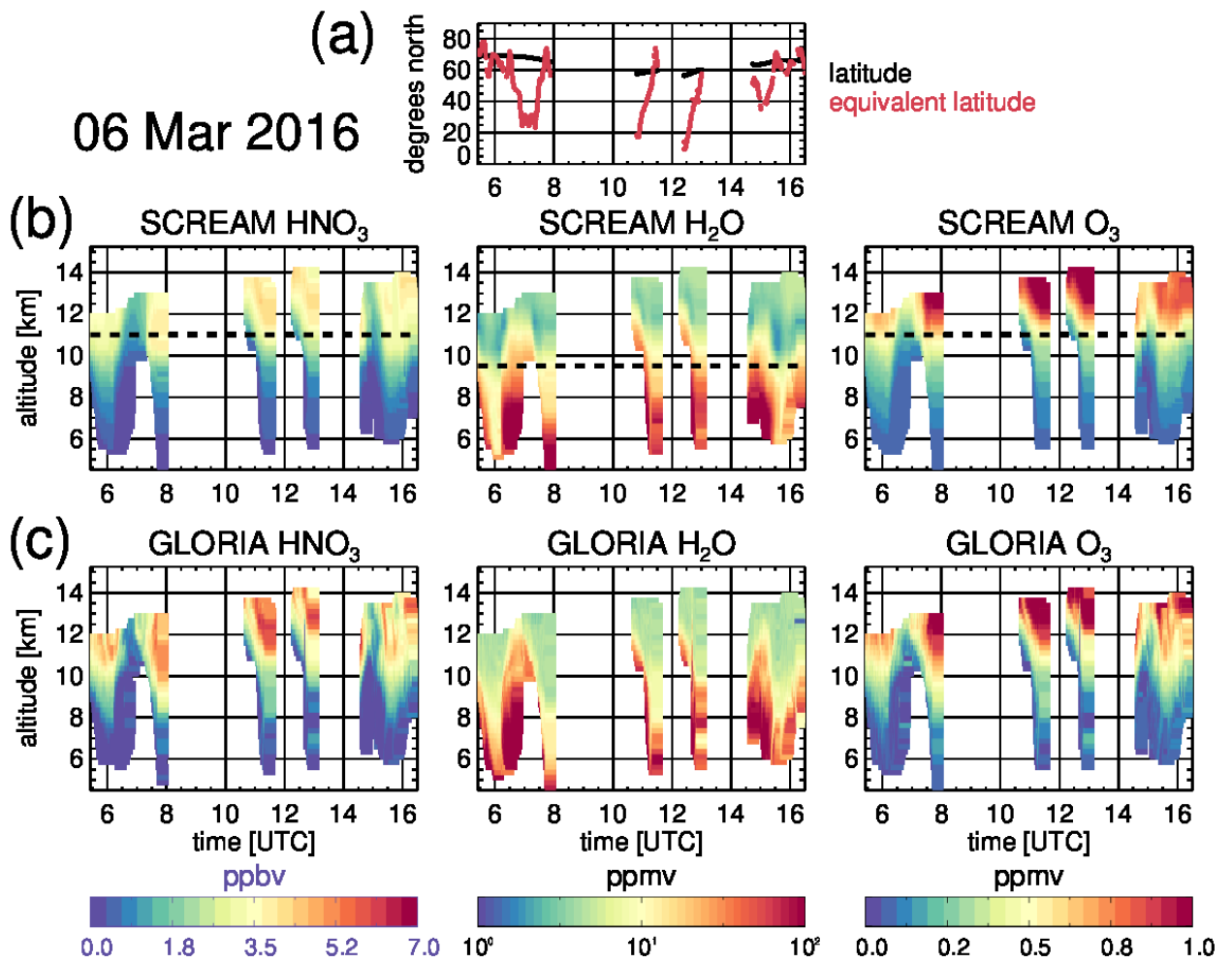


Figure S13: As in Fig. S3 but for 6 March 2016.

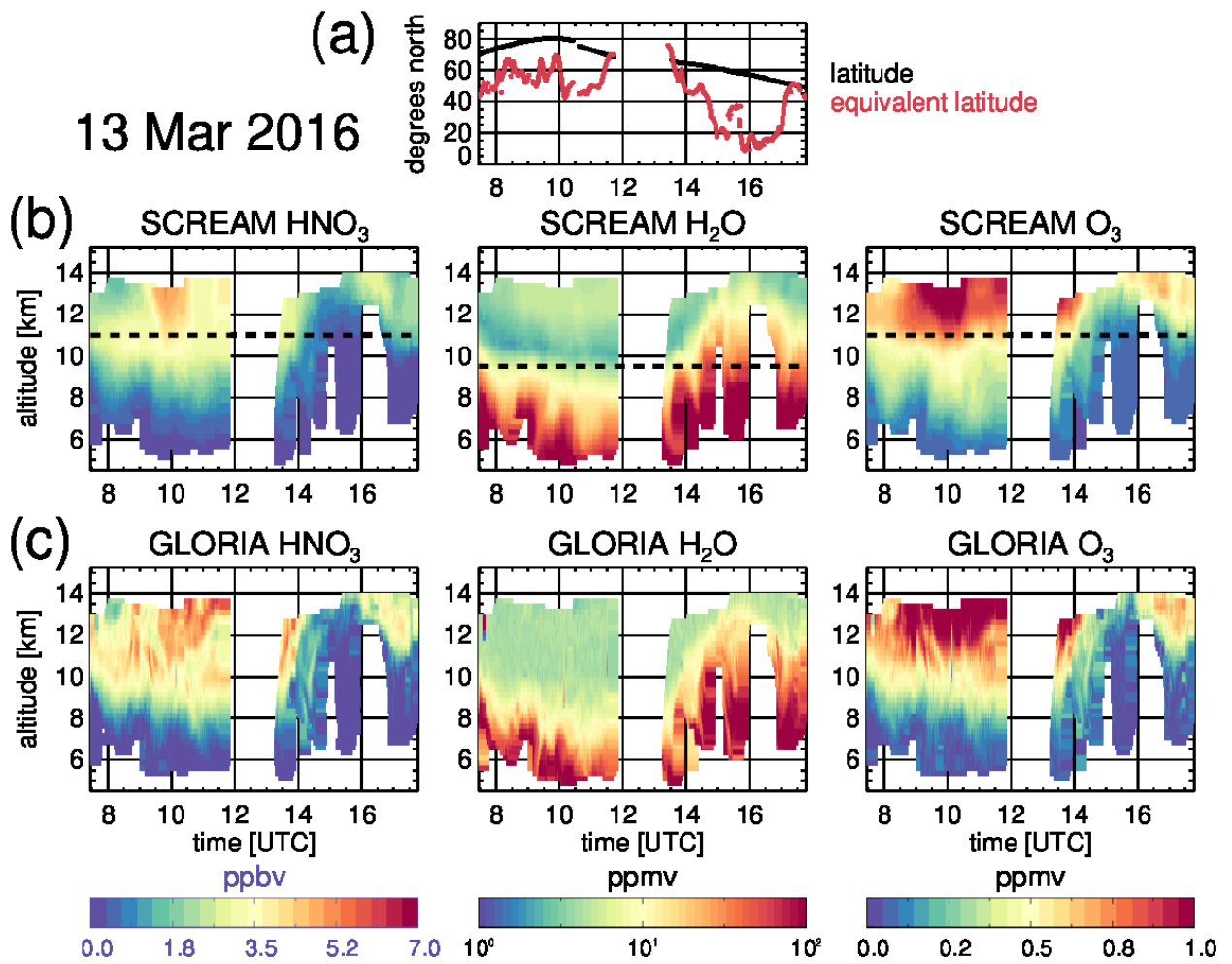


Figure S14: As in Fig. S3 but for 13 March 2016.

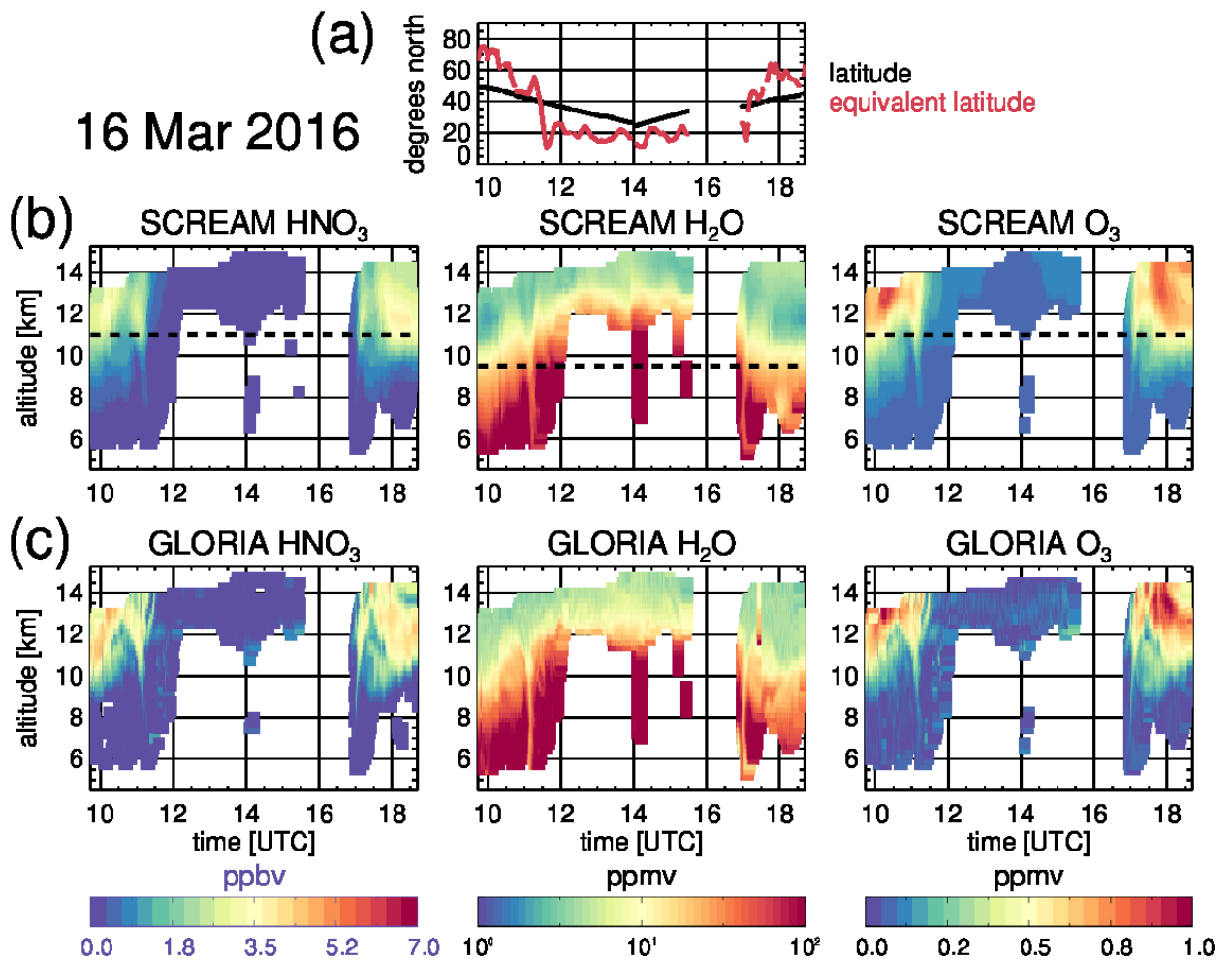


Figure S15: As in Fig. S3 but for 16 March 2016.

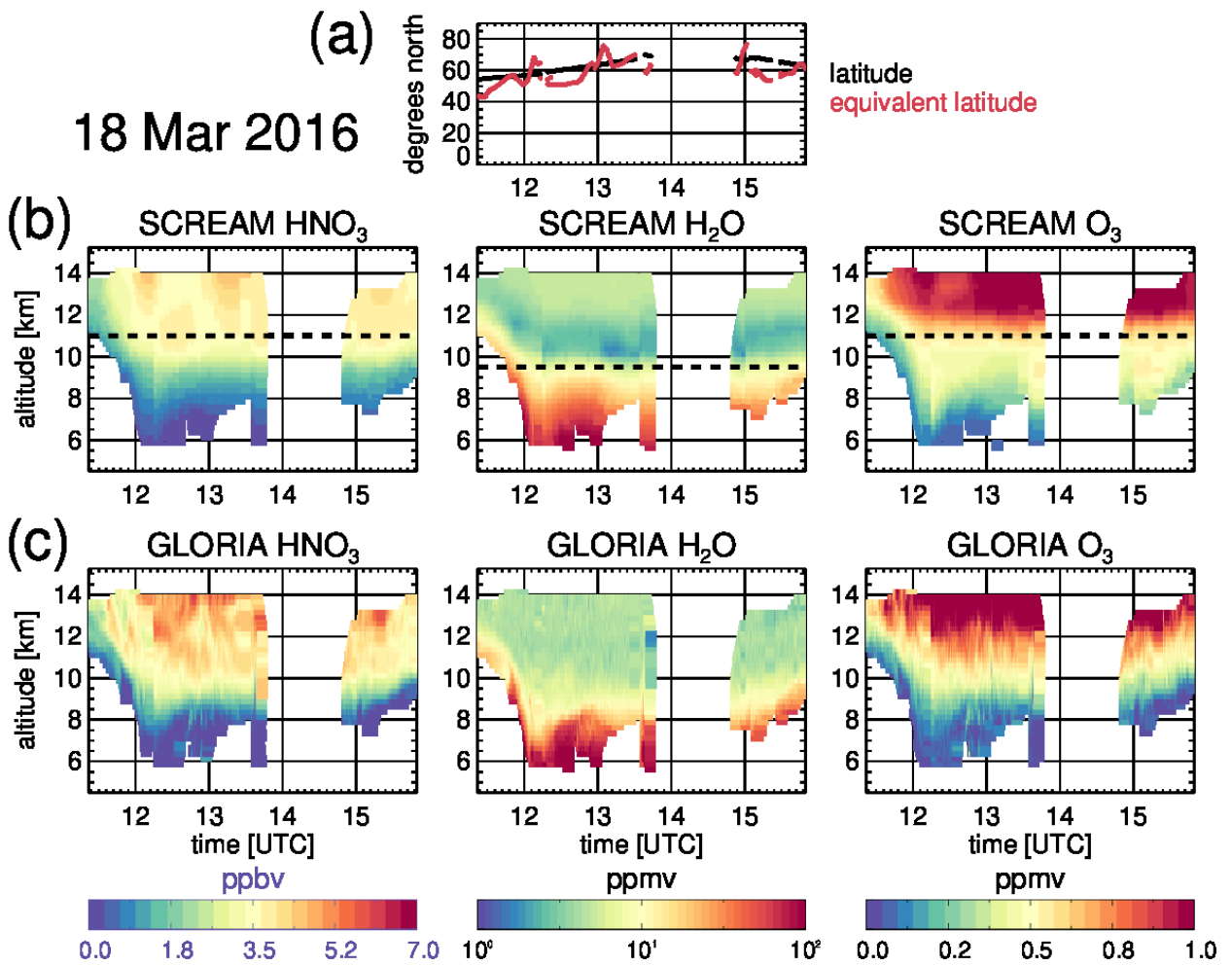


Figure S16: As in Fig. S3 but for 18 March 2016.

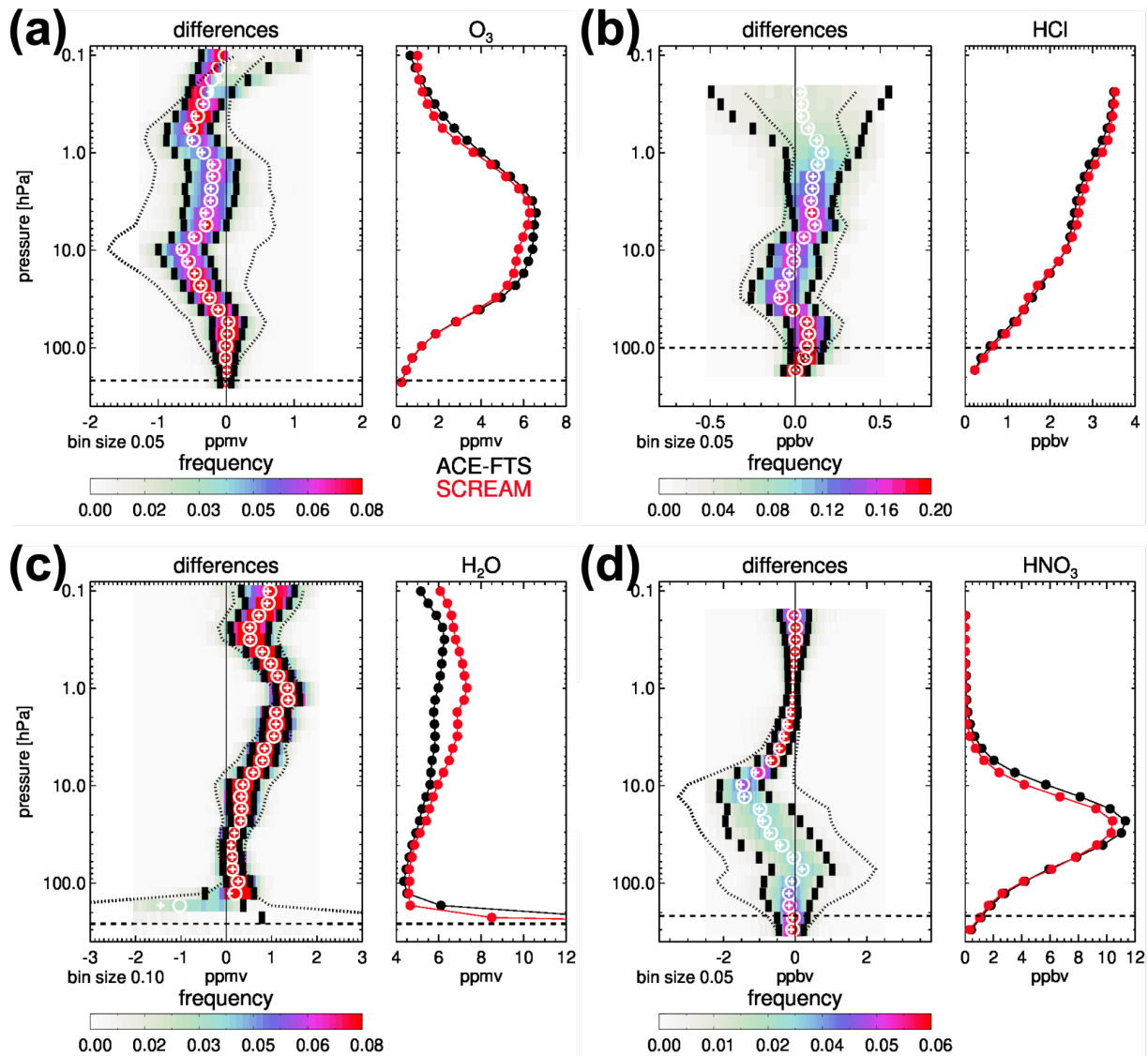


Figure S17: Statistical comparisons of the SCREAM ozone (a) and HCl (b), H₂O (c), and HNO₃ (d) with ACE-FTS observations for December–January, 30°N–60°N. The right- and left-hand side panels show mean profiles and difference statistics, respectively. Shown are the difference mean (plus signs), median (open circles), standard deviations around the mean (short vertical bars), probability density functions (colors) at prescribed pressure levels. The dotted lines are the mean difference plus/minus standard deviation of the ACE-FTS observations. All available December–January 2005–2020 ACE-FTS data are used.

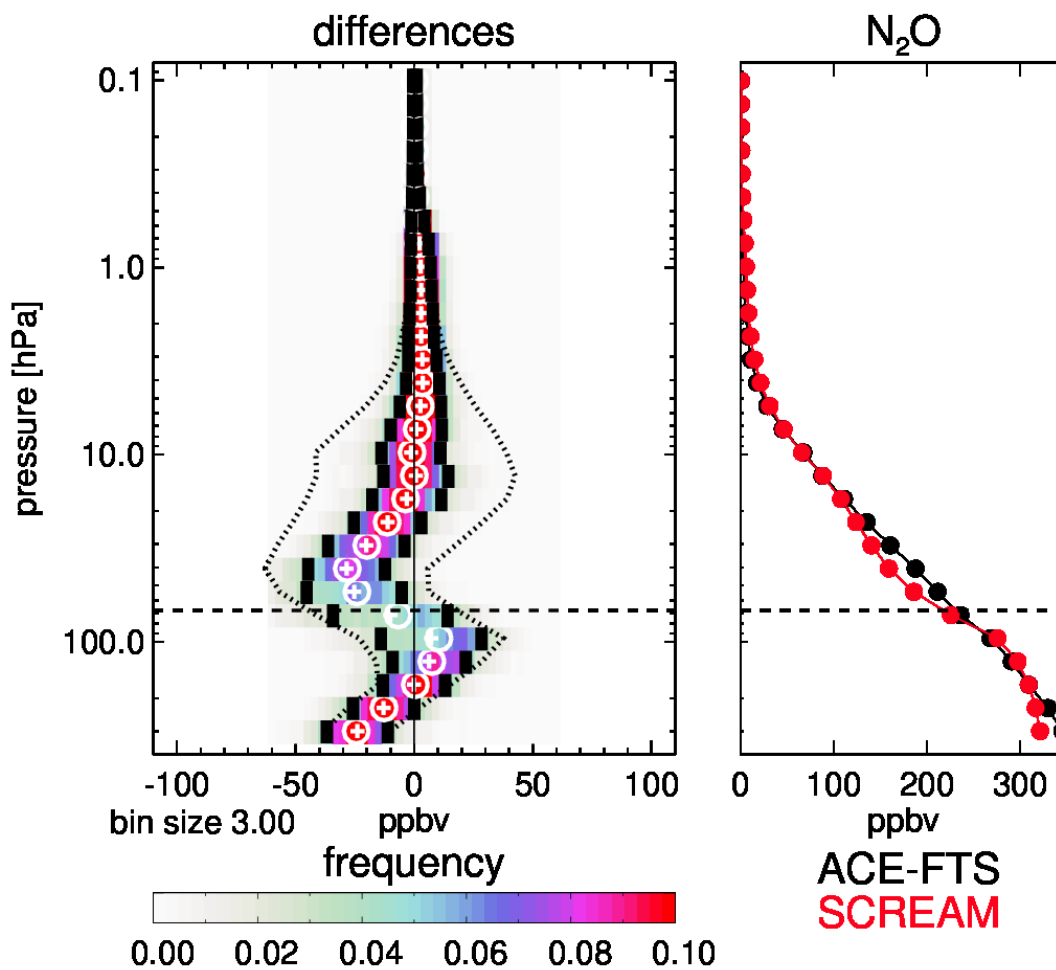


Figure S18: As in Fig. S17 but for N₂O.

Movie S1. File name: M1-Lauder-FPH-SCREAM.mp4. Animation showing all available frost point hygrometer water vapor profiles at Lauder, New Zealand (169.68°E, 45.04°S) between 2005 and 2021 (black) and collocated M2-SCREAM profiles (blue).

Movie S2. File name: M2-Hilo-FPH-SCREAM.mp4. As in Movie S1 but for Hilo, Hawaii (155.05°W, 19.72°N).

Movie S3. File name: M3-Boulder-FPH-SCREAM.mp4. As in Movie S1 but for Boulder, CO, USA (105.2°W, 39.95°N).